University of Denver
Digital Commons @ DU

Electronic Theses and Dissertations | Graduate Studies

3-2024

The Interplay of Spin, Charge, and Heat: From Metal/Insulator Heterostructures to Perovskite Bilayers

Sam M. Bleser

Follow this and additional works at: https://digitalcommons.du.edu/etd

 Part of the Condensed Matter Physics Commons, and the Other Materials Science and Engineering Commons


All Rights Reserved.

The Interplay of Spin, Charge, and Heat: From Metal/Insulator Heterostructures to Perovskite Bilayers

Abstract

In this dissertation begin with an investigation of non-local spin transport in an amorphous germanium (a-Ge) sample via the inverse spin Hall effect (ISHE). In that study we show that commonly used techniques such as differential conductance and delta mode of a paired Keithley 6221/2182a for non-local resistance measurements can lead to false indicators of spin transport. Next, we turn out attention to a thickness dependent study in thermally-evaporated chromium (Cr) thin films on a bulk polycrystalline yttrium-iron-garnet (YIG) substrate. This project analyzed the spin transport in the Cr films versus thickness via the longitudinal spin Seebeck effect (LSSE). This research revealed a complex thickness dependence of the spin-to-charge conversion and LSSE voltages for the evaporated Cr that may be a consequence of strain in Cr and finite size effects. We continue to examine LSSE in thermallyevaporated Cr, but now under a temperature dependent study. The results reveal an enhancement in the evaporated Cr below 200 K, where the Cr thin film transitions from a mixed SDW antiferromagnetic state described by the combination of a antiferromagnetic commensurate SDW (CSDW) and paramagnetic incommensurate SDW (ISDW) to a full antiferromagnetic state where both CSDW and ISDW are antiferromagnetic. This is absent in sputtered Cr thin films deposited on similar YIG substrates. Finally, we explore the spin-flopped coupled lanthanum strontium ferrite (LSFO) lanthanum strontium manganite (LSMO) bilayer grown on a lanthanum strontium aluminate (LSAT) substrate. This research focuses on the possible control of magnetic moments using current pulses.

Document Type

Dissertation

Degree Name

Ph.D.

First Advisor

Barry L. Zink

Second Advisor

Xin Fan

Third Advisor

Pavel Salev

Keywords

Spin hall effect, Spincaloritronics, Spintronics

Subject Categories

Condensed Matter Physics | Materials Science and Engineering | Other Materials Science and Engineering | Physical Sciences and Mathematics | Physics

Publication Statement

Copyright is held by the author. User is responsible for all copyright compliance.

THE INTERPLAY OF SPIN, CHARGE, AND HEAT: FROM METAL/INSULATOR HETEROSTRUCTURES TO PEROVSKITE BILAYERS

A Dissertation

Presented to

the Faculty of the College of Natural Sciences and Mathematics

University of Denver

In Partial Fulfillment

of the Requirements for the Degree

Doctor of Philosophy

---

by

Sam M. Bleser

March 2024

Advisor: Dr. Barry Zink

©Copyright by Sam M. Bleser 2024

All Rights Reserved

Author: Sam M. Bleser
Title: THE INTERPLAY OF SPIN, CHARGE, AND HEAT: FROM METAL/INSULATOR HETEROSTRUCTURES TO PEROVSKITE BILAYERS
Advisor: Dr. Barry Zink
Degree Date: March 2024

ABSTRACT

In this dissertation begin with an investigation of non-local spin transport in an amorphous germanium (a-Ge) sample via the inverse spin Hall effect (ISHE). In that study we show that commonly used techniques such as differential conductance and delta mode of a paired Keithley 6221/2182a for non-local resistance measurements can lead to false indicators of spin transport. Next, we turn out attention to a thickness dependent study in thermally-evaporated chromium (Cr) thin films on a bulk polycrystalline yttrium-iron-garnet (YIG) substrate. This project analyzed the spin transport in the Cr films versus thickness via the longitudinal spin Seebeck effect (LSSE). This research revealed a complex thickness dependence of the spin-to-charge conversion and LSSE voltages for the evaporated Cr that may be a consequence of strain in Cr and finite size effects. We continue to examine LSSE in thermally-evaporated Cr, but now under a temperature dependent study. The results reveal an enhancement in the evaporated Cr below 200 K, where the Cr thin film transitions from a mixed SDW antiferromagnetic state described by the combination of a antiferromagnetic commensurate SDW (CSDW) and paramagnetic incommensurate SDW (ISDW) to a full antiferromagnetic state where both CSDW and ISDW are antiferromagnetic. This is absent in sputtered Cr thin films deposited on similar YIG substrates. Finally, we explore the spin-flopped coupled lanthanum strontium ferrite (LSFO) lanthanum strontium manganite (LSMO) bilayer grown on a lanthanum strontium aluminate (LSAT) substrate. This research focuses on the possible control of magnetic moments using current pulses.

ACKNOWLEDGEMENTS

Before embarking on this thesis, I extend heartfelt appreciation to those who have made this journey possible. The past decade of my life, dedicated to becoming a proficient scientist, has been marked by a myriad of challenges and triumphs. Throughout this transformative period, there have been numerous exceptional individuals whose guidance I have relied upon.

My heartfelt gratitude goes to my undergraduate friends -Tristan Aft, Dave Austin, Jeremy Jones, Becca Brnich, Christian Hawkings, and Joseph Synder - provided unwavering support, making those years unforgettable.

Special thanks to my inspiring physics professors at the College of Charleston: Dr. Gardner Marshall, Dr. Micheal Larsen, and Dr. Jeffery Wragg, who ignited and nurtured my passion for physics.

At the University of Denver friends: Matthew Natale, Leopoldo Hernandez, Kyle Peterson, Nick Boyd, Ryan Greening, and Andrew Torres, who contributed not only to my scientific knowledge but also to personal growth.

My mentor, Dr. Barry Zink, instilled confidence and excellence, shaping me into a skilled experimentalist. Dr. Xin Fan's support and teachings also contributed significantly.

Acknowledgment is also extended to my collaborators at the University of California, Davis—Dr. Yayoi Takamura, Dayne Sasaki, and Ishmam Nihal—for their contributions to the growth and characterization of our perovskite samples.

Lastly, immense gratitude to my family - Sin, Devin, Kyle, Andy, Kiera, Kiana, and Shayleigh - for their unwavering support, advice, and love. To my mom and dad, I express my deepest appreciation and love.

TABLE OF CONTENTS

LIST OF FIGURES

CHAPTER 1: MOTIVATION

In the pursuit of technological advancement, the field of condensed matter physics has witnessed a paradigm shift with the emergence of spintronics and spin caloritronics. These cutting-edge fields promise to revolutionize the way we process and utilize information, offering unparalleled opportunities for innovation and progress.

At its core, spintronics differs from traditional electronics by harnessing the intrinsic spin of electrons, a fundamental quantum property. Unlike classical electronics that solely relies on the charge of electrons, spintronics leverages both their charge and spin, providing an additional degree of freedom. This intrinsic spin property not only enhances the storage and transmission of information but also facilitates the development of novel devices with improved performance and efficiency. The potential impact of spintronics extends across a myriad of applications, from ultra-fast and energy-efficient data storage to the creation of spin-based logic devices, paving the way for unprecedented computational capabilities.

In parallel, spin caloritronics explores the interplay between the flow of spin and heat, opening up avenues for efficient energy conversion and management. As we grapple with the challenges of a rapidly evolving global energy landscape, the pursuit of sustainable solutions becomes paramount. Spin caloritronics offers a unique approach to address these challenges by providing new insights into the manipulation and control of heat in electronic systems. This not only holds promise for more energy-efficient electronic devices but also lays the groundwork for the development of spin-based thermoelectric materials, capable of converting waste heat into valuable electrical energy.

Therefore, it is critical to understand the underlying physics from both a material standpoint as well as a device perspective for spintronics and spincaloritronic research in order to advance technology for the next generation.

CHAPTER 2: INTRODUCTION

In this chapter, we provide a concise overview of the thesis structure. After careful consideration and meticulous planning of the paper's organization, it is anticipated that this outline represents the optimal arrangement. The thesis consists of three main sections: an introduction covering essential background information, a comprehensive presentation of the experimental work conducted during my graduate studies, and an appendix housing additional information that did not find a place within the main text.

The introduction (chapters 2 through 4) initiates with a delineation of the general theoretical framework necessary for comprehending the experimental aspects. A brief review of transport mechanisms in metals is undertaken, starting with charge transport, followed by thermal transport, and concluding with spin transport. The introduction highlights critical phenomena explored in the experimental work, such as the spin Hall effect, spin Seebeck effect, and spin Hall magnetoresistance. Subsequently, we delve into crucial details regarding device designs employed for sensitive measurements, categorizing them as non-local and local devices, both contributing essential insights to transport measurements. The section concludes with a detailed overview of device fabrication, incorporating e-beam lithography and photolithography, along with material deposition.

Chapters 5 through 9 comprise the experimental work conducted. The exploration begins with a focus on amorphous germanium (a-Ge), emphasizing the significance of understanding non-local spin transport measurements in highly insulated materials. Subsequent chapters (6 through 8) delve into investigations on chromium (Cr), unveiling intriguing findings related to longitudinal spin Seebeck effect (LSSE)

measurements, particularly noting the influence of film disorder and stress on spin-to-charge conversion. Chapter 7 extends this exploration beyond room temperature, revealing an enhancement of spin-to-charge conversion in thermally-evaporated Cr at temperatures below 200K, not observed in sputter Cr thin films. Chapter 8 delves into the magnetoresistance behaviors between thermally-evaporated Cr and sputtered Cr thin films.

Chapter 9 concludes the experimental section, presenting intriguing findings with spin-flop coupled lanthanum strontium ferrite (LSFO) and lanthanum strontium manganite (LSMO) bilayers. The thesis concludes with a summarizing conclusion, encapsulating the entirety of the work undertaken during my graduate studies, followed by an appendix housing miscellaneous information. The appendix covers topics such as atomic force microscopy (AFM) for determining thin film thickness and roughness, scanning electron microscopy (SEM) images of devices, and essential LabVIEW code developed for device measurements and data analysis.

CHAPTER 3: TRANSPORT EFFECTS

This chapter is dedicated to a comprehensive overview of charge, heat, and spin transport in a metal. This will set up the critical transport properties and phenomena that are instrumental in understanding the experimental work conducted, starting from chapter 4. This chapter will begin with a review of charge transport carried by electrons in a metal while diving into phenomena such as the Hall effect and magnetoresistance, the thermal transport by both electrons and phonons with a discussion of the Nernst effect and Seebeck effect, and finally a discussion of spin transport carried by magnons in a ferromagnetic insulator and conduction electrons in a metal with an overview of the spin Hall effect, spin Hall magnetoresistance, spin Seebeck effect, and spin orbit torque.

3.1. ELECTRICAL TRANSPORT

Electrical properties are a consequence of the transport mechanisms of conduction electrons in a metal that result from scattering and interactions with other conduction electrons or with the lattice. Here we will conceptually and mathematically describe the electron transport in a metal with a discussion of the Hall effect and magnetoresistance when an external magnetic field is applied.

One of the earliest models to describe the electron motion in a crystal lattice for a metal comes from Drude[60]. In its simplest form kinetic theory treats the molecules of a gas as identical solid spheres, which move in straight lines until they collide with one another as illustrated in Figure 3.1.

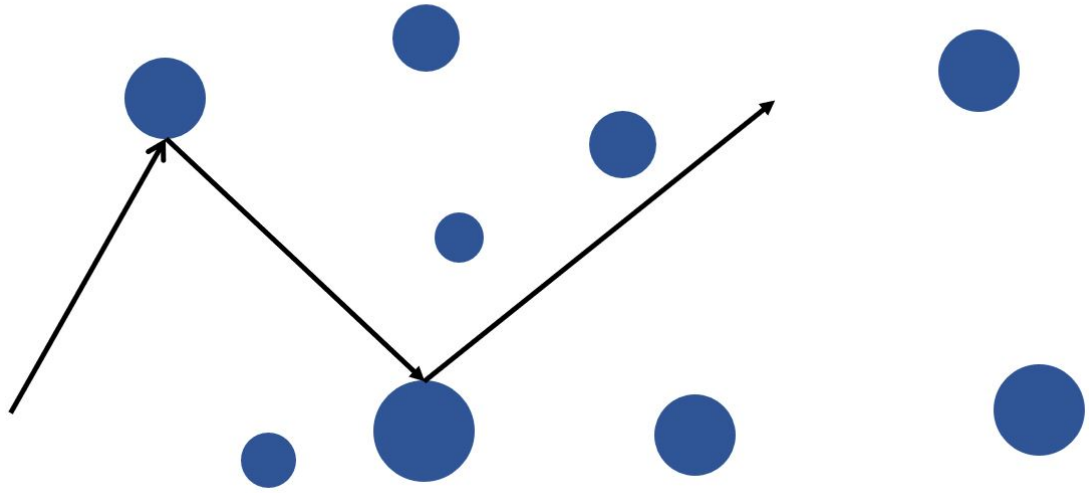

Figure 3.1: An illustration of the kinetic theory for electrons in a metal. The electrons are represented by dark spheres and the vectors illustrate a path in which one particular conduction electron took while moving in the metal. As we can see, the conduction electron moves in straight lines until colliding with another electron. Figure adapted from [176].

The time taken up by a single collision is assumed to be negligible, and, except for the forces coming momentarily into play during each collision, no other forces are assumed to act between the particles.

According to Ohm's law, the current I flowing in a wire is proportional to the potential drop V along the wire: $V = IR$, where R the resistance of the wire, depends on its dimensions, but is independent of the size of the current or potential drop. The resistivity, ρ, is defined to be the proportionality constant between the electric field $\vec{E}$ at a point in the metal and the current density $\vec{j}$ that it introduces

$$\vec{E} = \rho\vec{j}. \tag{3.1}$$

The current density $\vec{j}$ is a vector parallel to the flow of charge, whose magnitude is the amount of charge per unit time crossing a unit area perpendicular to the flow.

If n electrons per unit volume all move with velocity $\vec{v}$, then the current density they give rise to will be parallel to $\vec{v}$. Furthermore, in a time dt the electrons will advance by a distance vdt in the direction of $\vec{v}$, so that $n\,(vdt)\,A$ electrons will cross an area A perpendicular to the direction of flow. Since each electron carries a charge $-e$, the charge crossing A in the time dt will be $-nevAdt$, and hence the current density is

$$\vec{j} = -ne\vec{v}. \tag{3.2}$$

At any point in a metal, electrons are always moving in a variety of directions with a variety of thermal energies, thus the net current density is given by 3.2, where $\vec{v}$ is the average electronic velocity. The Drude model is a simple explanation for electron transport of a metal that treats the behavior classically. However, electrons are quantum in nature and follow the Fermi-Dirac[176,285] statistics. Using the Sommerfeld model[131,176,233], we can more accurately explain electron transport in a metal.

3.1.1. HALL EFFECT AND MAGNETORESISTANCE

Upon the application of a magnetic field, a voltage develops along the lateral sides of a metal, the Hall effect, and the resistance is modified, the magnetoresistance of a metal. E. H. Hall argued in 1879 that if the electric current in a metal is attracted to an external magnetic field, the electric current should be drawn to the lateral sides of the metal, and the resistance experienced should increase[92]. The Hall effect is illustrated in Figure 3.2.

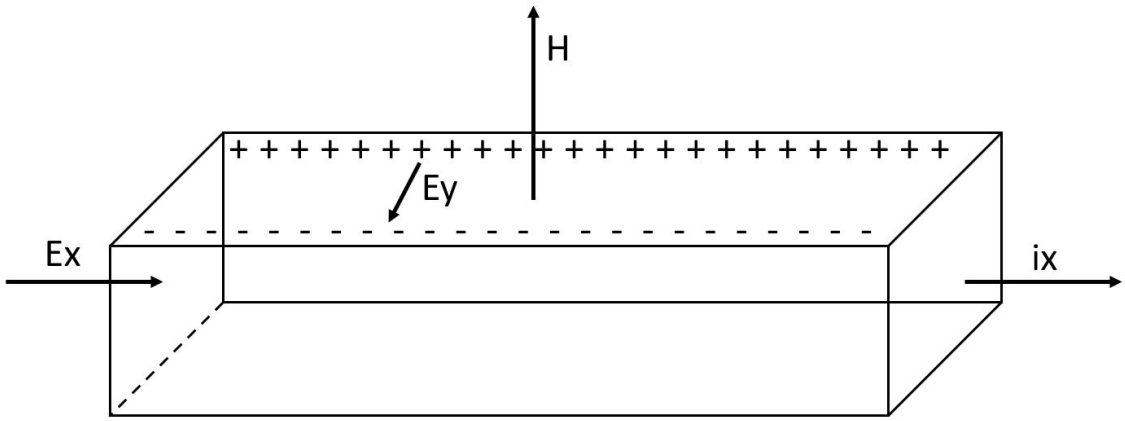

Figure 3.2: An illustration of the ordinary Hall effect. A current flowing in the x-direction i_x with associated electric field E_x within a metal. When subjected to an out-of-plane magnetic field H normal to the metal, in this case the z-direction, the electrons in the metal are subjected to an Lorentz force, and thus accumulate on one lateral side of the metal. Charge is separated on either edge of the metal as represented by the $-$ and $+$ symbols. This causes a transverse electric field H_y to develop, commonly known has a Hall voltage. Figure adapted from [176].

An electric field E_x is applied to a wire extending in the x-direction due to a current density j_x. In addition, a magnetic field $\vec{H}$ is applied out-of-plane of the metal, usually the z-direction. As a result the Lorentz force acting on the electrons in the metal

$$-\frac{e}{c}\vec{v} \times \vec{H}, \tag{3.3}$$

moving electrons in the metal are deflected towards the lateral edges. Eventually the electrons accumulate on the lateral edges and electric field along the lateral direction, namely the y-direction, develops. In equilibrium this transverse field, know as the Hall field, E_y will balance the Lorentz force, and current will flow only in the x-direction. The Hall effect is typically summed up in a quantity know as the Hall coefficient:

$$R_H = -\frac{1}{nec}, \tag{3.4}$$

where n is the charge carrier concentration, e is the magnitude of the electron charge, and c is the velocity of light. This is interesting because this is stating that the Hall coefficient depends on no parameters of the metal except the density of charge carriers.

The electrical resistivity of a metal under an externally applied magnetic field will be modified due to magnetoresistance. For the ordinary magnetoresistane, the change in resistance is positive for both longitudinal and transverse directions in a metal. Magnetoresistance is defined as:

$$\frac{\Delta\rho}{\rho_\circ} = \frac{\rho\left(B\right) - \rho_\circ}{\rho_\circ}, \tag{3.5}$$

where $\Delta\rho$ is the change in resistivity, $\rho_\circ$ is the resistivity without the application of a magnetic field, and $\rho\left(B\right)$ is the resistivity as a function of magnetic field strength, B. The application of an external magnetic field bends the trajectory of electrons into helices whose axes are parallel to the magnetic field direction. When electrons are wound into tight helices, they execute more collisions, and the conduction process changes considerably.

Beyond the ordinary Hall effect and ordinary magnetoresistance, there exists other phenomena that depend not on the applied external magnetic field, but the magnetization of a magnetic material such as anisotropic magnetoresistance (AMR) [17,157] and anomalous Hall effect (AHE) [171]. In these magnetic materials, such as ferromagnets, it is the angle between the magnetization and applied current that will modify the resistance of the material without the need of an externally applied magnetic field. Of course, these effects can contribute to existing Hall or magnetoresistive effects when a magnetic material is subjected to an externally applied magnetic field.

3.2. THERMAL TRANSPORT

In a metal, the participants in thermal transport are often the conduction electrons and phonons, a quasi-particle that is the quantization of a lattice vibration.

In most situations, the conduction electrons in a metal are the main carriers of heat rather than phonons[77,131,176] or even magnons[175,273]. In nature, thermal energy can be transferred through three different mechanisms: conduction, convection, and radiation. In the solid phase and at the molecular scale, convection and radiation are less relevant. We can describe the conduction of heat in a metal with Fourier's law:

$$\vec{j}^{q} = -\kappa \nabla T, \tag{3.6}$$

where $\vec{j}^{q}$ is the thermal current density, κ is the thermal conductivity, and ∇T is the thermal gradient. If we model a metal as a dilute gas under kinetic theory, the thermal conductivity can be defined as:

$$\kappa = \frac{1}{3} C_v v \lambda, \tag{3.7}$$

where C_v is the heat capacity at constant volume, v is the mean velocity of the particles in the gas, and λ is the mean free path. This means that thermal conductivity is the product of the amount of thermal energy that can be carried by a particle at the speed and distance it moves before scattering.

When an electric current density is introduced to a metal, the metal warms under the effects of Joule heating. Introducing more electrons into a metal leads to an increase of scatterings due to the higher density of electrons flowing through the metal. These scattering event lead to a higher rate of energy transfer through collisions in the form of heat causing the metal to warm. These heating effects in a metal lead to interesting phenomena such as the Seebeck effect and Nernst effects, where the interplay of thermal and electrical energies occur.

3.2.1. THERMOELECTRICITY

The combination of electron and heat transport births a new field called thermoelectricity. A common phenomena of study in this field is the Seebeck effect, as illustrated in Figure 3.3, which refers to the generation of an electric voltage due to a temperature difference across two dissimilar metals. Conduction electrons from the hot temperature end of the material, migrate towards the cold temperature end, through scattering mechanisms with phonons and other conduction electrons, these migrating electrons lose energy and eventually accumulate on the cold end. This creates a separation of charges and thus a voltage develops parallel to the temperature gradient.

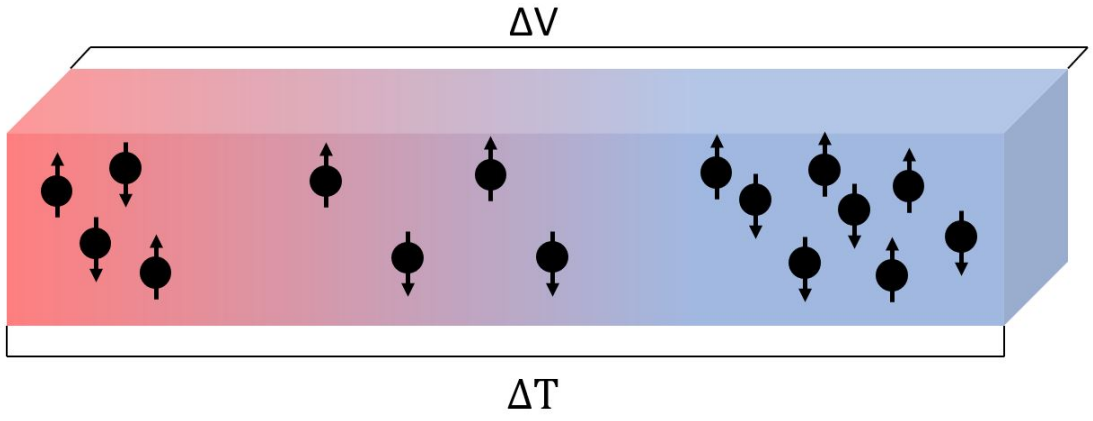

Figure 3.3: An illustration of the conventional Seebeck effect. An input temperature difference ΔT drives the diffusion of conduction electrons via phonon-electron scattering (represented as black spheres with spin orientation given by vector arrows) in a metal to on side creating an accumulation of negative charge. As a result of the separation of charges on either side of the metal, a voltage difference develops. Figure adapted from [95].

Originally observed by Seebeck in 1821 [182,216,243], a voltage difference is generated across the terminals of an open circuit made up of a pair of dissimilar metals or alloys whose junctions are held at different temperatures. This can be expressed by the following equation:

$$\Delta V = \alpha \Delta T, \tag{3.8}$$

where ΔV is the voltage difference generated, α is the Seebeck coefficient, and ΔT is the temperature difference between the two dissimilar metals. The generated voltage depends on the metals employed and also on the temperature difference, but does not depend on the distribution of temperature along the metals between the junctions [199]. This is the classical description of the Seebeck effect; however, there are analogues to this phenomena that rely on spin currents as opposed to electric currents that will be explored in a later section.

3.2.2. NERNST EFFECTS

One early phenomena that exemplifies the mixing of charge, heat, and magnetism is the ordinary Nernst effect. In a metal with an applied in-plane thermal gradient and an out-of-plane externally applied magnetic field results in a transverse electric field as illustrated in Figure 3.4.

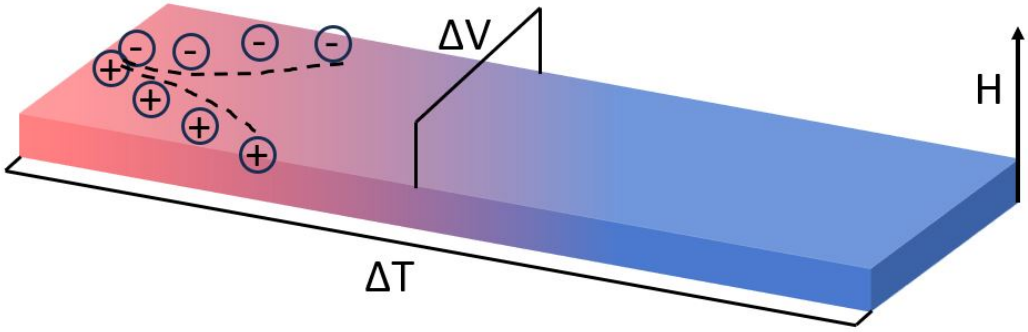

Figure 3.4: An illustration of the ordinary Nernst effect. Here charges (positive represented by + symbols and negative by − symbols) are driven by an in-plane temperature difference ΔT. An external magnetic field H normal to the sample causes the charges to move toward the edges of the sample via a Lorentz force. An electric field develops between the lateral edges of the sample due to an accumulation of opposing charges on either side that is measure as a Nernst voltage, V_N. Figure adapted from [79].

The ordinary Nernst effect can be mathematically described by the following equation:

$$E_y = \frac{N}{H}\nabla T, \tag{3.9}$$

where E_y is the transverse electric field (or voltage), N is Nernst coefficient of the material, H is the externally applied magnetic field normal to the material, and ∇T is the in-plane thermal gradient.

Conduction electrons in a metal are driven from an area of high temperature to an area of low temperature due to an in-plane thermal gradient. An externally applied magnetic field causes the charges to move towards the lateral edges due to a Lorentz force and thus a charge accumulation forms on the lateral edges of the metal.

The separation of charge carriers on the lateral edges generates an electric field that is both normal to the in-plane thermal gradient and magnetic field, this is commonly referred to as the Nernst effect[21,22].

Beyond the ordinary Nernst effects, others have been experimentally observed such as the spin Nernst effect[43,164,222], where the separation of spin orientation of conduction electrons are taken into consideration, the anomalous Nernst effect[50,108,194], that depends on a magnetic material's magnetization rather than an applied magnetic field, and the planar Nernst effect[267,281], where the applied magnetic field and thermal gradient are both in the plane of the sample.

3.3. SPIN TRANSPORT

In previous sections we described the transportation of charges in a metal under the influence of both a thermal gradient and externally applied magnetic field to describe phenomena such as ordinary Hall effect, magnetoresistance, and Seebeck effect. In this section, we explore the spin analogues of these phenomena and consider not the flow of charge, but the flow of spin in a metal.

3.3.1. SPIN HALL EFFECT

Early theoretical work by Dyakonov and Perel[65,66] referred to the phenomena of Mott scattering[169] and of the anomalous Hall effect (AHE)[91] to theoretically predict the extrinsic spin Hall effect (SHE). In particular, they pointed out that spin-dependent asymmetric deflection is observed in electron beams due to Mott scattering[85,169,223] and that Mott's skew scattering is regarded among the origins of the AHE of electrons in ferromagnets[23,122,171,227] Under an applied electrical current, asymmetric spin-dependent deflection should occur in normal metals with sufficient spin-orbit coupling. Nonmagnetic metals in equilibrium have the same number of spin-up and spin-down electrons and no transverse charge imbalance will occur. Instead, the SHE generates an edge spin accumulation that has opposite polarization at opposite edges[106,224,255] as illustrated in Figure 3.5

Taking inspiration of theoretical work on the anomalous Hall effect [25,55,150,171,184], Hirsch [97] argued that the same scattering mechanisms, skew scattering and side-jump, that gave rise to the anomalous Hall effect will also give rise to the spin Hall effect in the absence of any net magnetization.

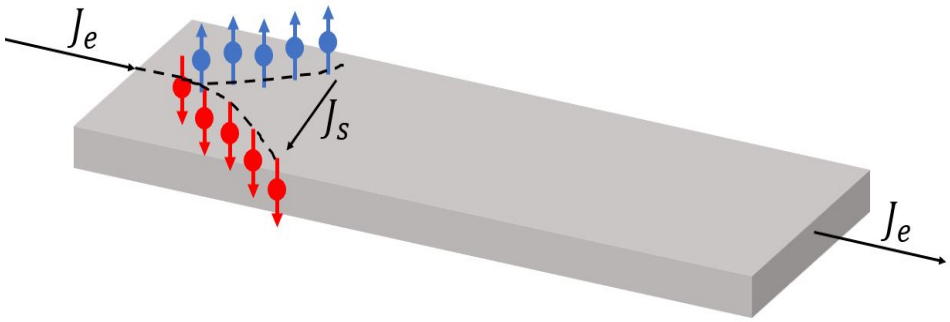

Figure 3.5: A charge current density, J_e, flows through the metal and through skew scattering processes the conduction electrons of the metal are asymmetrically scattered based on their spin orientation. This leads to a spin imbalance on the lateral edges of the metal as shown with the spin-up electrons (blue spheres) accumulating on one side and the spin-down electrons (red spheres) accumulation on the opposite end. Absent of a charge imbalance, the spin imbalance generates a spin current density, J_s.

From Figure 3.5 a charge current density flows through a nonmagnetic metal with a sufficiently large spin-orbit coupling. Electrons are asymmetrically scattered, depending on the microscopic details it will be due to either skew-scattering or side-jump for extrinsic SHE, based on their spin polarization that leads to a separation of spin along the lateral edges absent of a separation of charge. This spin imbalances generates a transverse spin current density via the spin Hall effect (SHE).From symmetry arguments, the reciprocal effect, the inverse spin Hall effect (ISHE), where a spin current density entering a nonmagnetic metal generates a transverse electric field.

Some time later, the spin Hall effect had been experimentally observed in several material systems including metals[128,205,209,218,263], semiconductors[123,274], ferromagnets[75,93,269], and antiferromagnets[15,36,87].

3.3.2. SPIN SEEBECK EFFECT

The spin Seebeck effect is regarded as the spin analogue of the classical thermoelectric effect, the Seebeck effect. First experimentally observed by Uchida *et al*[251] in 2008. In this pioneering work, a $Ni_{81}Fe_{19}$, a ferromagnetic metal commonly known as permalloy, was subjected to an in-plane thermal gradient parallel to an external magnetic field generated a voltage drop in an adjacent platinum thin film via the inverse spin Hall effect. This differs from the classical Seebeck effect because it is not due to the transport of charge under a thermal gradient, but a transport of spin under the influence of a thermal gradient.

The first seminal theoretical study by Johnson and Silsbee[117] established the framework for the flow of charge, heat, and nonequilibrium magnetization at an interface. They concluded that, for a system of two metals where one metal is a ferromagnet, there is a possibility of electrically and thermally induced magnetization currents and of magnetically induced thermal and electrical currents at the junction. In a similar fashion, electric and thermal potential gradients in a bulk ferromagnetic metal will drive a magnetization current[117].

The spin Seebeck effect is the generation of a spin voltage caused by a temperature gradient in a ferromagnet. Here, the spin voltage is a potential for electrons' spin to drive spin currents. More concretely, when a nonmagnetic metal is attached on top of a material with a finite spin voltage, a nonzero spin injection is obtained due to a combination of the spin-orbit coupling and inverse spin Hall effect[2]. There are two classifications of the spin Seebeck effect: transverse spin Seebeck effect (TSSE) and longitudinal spin Seebeck effect (LSSE). There is also the spin-dependent Seebeck effect that use conduction electrons to transport spin currents, otherwise magnons will carry the spin.

The LSSE consists of applying a temperature gradient, typically in an electrically insulating ferromagnet or ferrimagnet, along the z-direction, and a magnetic field along the x-direction. This is illustrated in Figure 3.6.

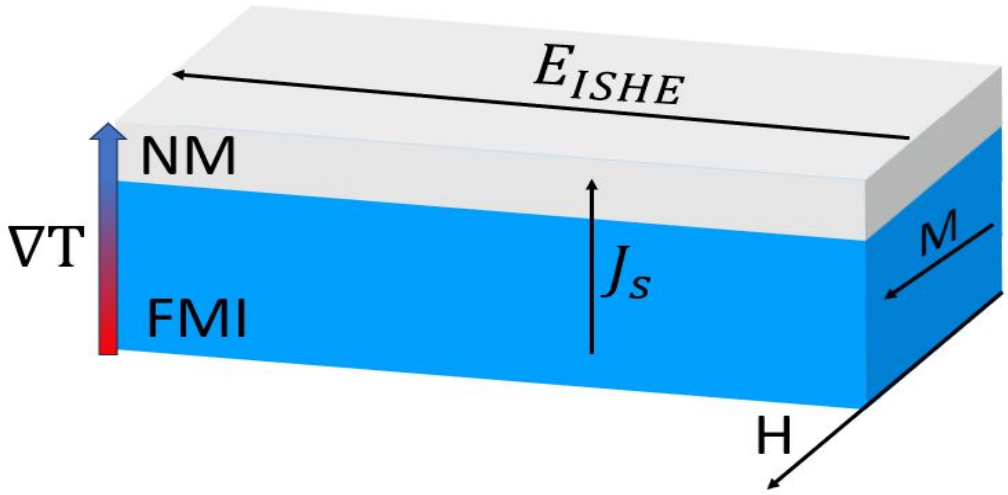

Figure 3.6: A thermal gradient, ∇T, applied in the z-direction in a ferromagnetic insulator (FMI)/ normal metal (NM) bilayer. An in-plane externally applied magnetic field, H, aligns the magnetization, M, of the FMI layer. A spin current, J_s, is generated and flows towards the NM layer, where it is transformed into a measurable electric field, E_{ISHE}, via the inverse spin Hall effect (ISHE).

The magnetic field gives the spin-polarization and net magnetic moment along the x-axis. The applied temperature gradient along the z-direction results in a magnon heat flux from either phonon-drag or magnon conductivity and thus a spin flux $\vec{j}_S$ along z. In typical LSSE experiments, one uses a good spin conversion material such as platinum (Pt)[101,162,165,201,250,261] as a charge-to-spin converter to detect transverse electric fields via the inverse spin Hall effect (ISHE)[5,209], mathematically described as:

$$\vec{E}_{ISHE} = (\theta_{SH}\rho_{NM})\,\vec{j}_S \times \sigma_S, \tag{3.10}$$

where $\vec{E}_{ISHE}$ is the electric field produced from the ISHE, θ_{SH} is the spin Hall angle of the spin conversion normal metal adjacent to the insulating ferromagnet or ferrimagnet, ρ_{NM} is the charge resistivity of the normal metal, $\vec{j}_S$ is the spin current density, and σ_S is the spin polarization. It is commonplace to use yttrium-iron-garnet (YIG) as the ferromagnetic insulator to generate the spin current. The spin that is carried by magnons in the electrically insulating YIG must be transferred to the conduction electrons in Pt. One plausible mechanism for spin transfer across the Pt/YIG interface is through the electron-magnon exchange interaction at the interface. This is also know as "s-d' scattering", where "s" refers to the electrons in Pt and "d" refers to local Fe moments in YIG[31,98]. The details of this interactions depends on the metallurgical and electronic details of the interface. It should also be mentioned that the longitudinal spin Seebeck effect can have contributions from proximity effects such as the anomalous Nernst effect (ANE)[32,83,101,121,124,125]. Through careful measurement these parasitic effects can be determined and or eliminated from the SSE signal.

In the transverse spin Seebeck effect (TSSE) geometry, a thermal gradient is applied to a spin-polarized material, like a ferromagnet, which drives a spin current parallel to the heat current. Due to the fact that a heat current passes through the ferromagnet, the spins are pushed out of equilibriuim. When placed in contact with a normal metal with sufficient spin conversion, a pure spin current, which is absent of any charge current, will diffuse from the ferromagnet into the normal metal. The gradient in spin-split chemical potential $d/dz\,(\mu_\uparrow(z) - \mu_\downarrow(z))$ leads to a net spin current into the normal metal. The spins must be pushed away from equilibrium through the applied temperature gradient and resulting heat current to enable a net flux of spins from the spin source, the ferromagnet, to the spin sink, the normal metal.

One might expect that if a flux of spins exists between the ferromagnet and the normal metal, and spins carry heat, then a finite thermal gradient in the z-direction, ∇T_z should be expected between the normal metal and the ferromagnet. There is experimental evidence that TSSE-like features might arise by LSSE or planar

Nernst effect (PNE) due to an accidental ∇T_z between normal metal and ferromagnet[12,13,103,104,162]. In thin films, a ∇T_z can arise from an inappropriate choice of substrate, where there is a thermal conductivity mismatch, or if wiring and thermal design are not engineered appropriately to avoid heat losses and uncontrolled heat fluxes. However, ∇T_z can be eliminated from measurements on bulk samples or free-standing films with careful mount that minimizes uncontrolled heat losses[31].

3.3.3. SPIN HALL MAGNETORESISTANCE

Unlike the ordinary magnetoresistance (MR) in non-magnetic metals, where the resistance is increased upon the application of an external in-plane magnetic field[52,244], or even anisotropic magnetoresistance (AMR), where a spontaneous magnetization normal to the film plane increases the electrical resistance in a metal[17,19,157], the spin Hall magnetoresistance (SHMR) is a new type of magnetoresistance in a bilayer made of a metal with strong spin-orbit coupling and a ferromagnetic insulator, where the electrical resistance was found to depend on the magnetization of the ferromagnetic insulator[4,90,103,127,156,172,256,265]. This new type of magnetoresistance has been explained by the simultaneous action of the spin Hall effect (SHE) and inverse spin Hall effect (ISHE)[40,41].

The spin Hall magnetoresistance for a bilayer system composed of a nonmagnetic metal with good spin-orbit coupling, such as platinum (Pt), adjacent to a ferrimagnetic insulator, such as yttrium-iron-garnet (YIG), is explained in terms of a non-equilibrium proximity effect caused by the simultaneous action of the SHE and ISHE that is modulated by the magnetization direction in YIG via the spin transfer at the normal metal/ferromagnet interface. When a charge current flows through the Pt, asymmetric scattering of the spins creates a spin accumulation on the edges leading to a transverse spin current that depends on the spin polarization, $\vec{j}_e \propto \vec{\sigma} \times \vec{j}_s$[14,119,128,174], where $\vec{j}_e$ is the charge current density, $\vec{\sigma}$ is the spin polarization, and $\vec{j}_s$ is the generated spin current density. Part of the generated spin current density is directed toward the interface between the normal metal Pt and

the ferrimagnetic insulator YIG. At the interface, the electrons in the Pt layer will interact with the localized magnetic moments in the YIG layer. Depending on the magnetization direction of the YIG, electrons spins will either be absorbed $\left(\vec{M} \perp \vec{\sigma}\right)$ or reflected $\left(\vec{M} \parallel \vec{\sigma}\right)$ [256], where $\vec{M}$ is the magnetization of YIG. Depending on the details of the interface and magnetization dynamics, spin angular momentum from the Pt electrons can be transferred to the magnetic moments of the YIG layer via spin transfer torques [192,224]. By changing the magnetization direction of the YIG, the polarization direction of the reflected spins in Pt, and thus the direction of the additional created charge current can be controlled. A charge current in the direction perpendicular to $\vec{j}_e$, that is perpendicular to the experimentally controlled charge current flowing in Pt, can also be created that leads to a transverse voltage via inverse spin Hall effect. These simultaneous actions lead to the modulation of the charge resistivity in the Pt layer that is dependent on the magnetization direction of the YIG layer underneath. For the Pt/YIG system, the SHMR mechanism has been described as [254]:

$$\rho_{pt} = \rho_{\circ} - \Delta\rho_{SHMR} m_y^2, \tag{3.11}$$

where ρ_{pt} is the resistivity of Pt, $\rho_{\circ}$ is the residual resistivity of Pt at low temperatures, $\Delta\rho_{SHMR}$ is the change in resistivity due to the SHMR, and m_y is the Cartesian component of the magnetization along the y-direction. From this, we see that the resistivity changes via SHMR is symmetric with respect to the magnetization reversal, which can be distinguished from contributions of possible inverse spin Hall voltage induced by the longitudinal spin Seebeck effect [73,257,262]

3.4. SPIN-ORBIT TORQUES

Spin-orbit torque (SOT) is a phenomenon where an electrical current flowing through a bilayer of a heavy metal and a magnetic material, such as a ferromagnet,

can affect the magnetization in the ferromagnet leading to oscillations or switching. This torque can originate either from the bulk of a material or at an interface and can lead to a transfer of angular momentum known as a spin-transfer torque (STT). Early work[24,78,225] proposed that STT can be explained as follows: when a charge current passes through a magnetic material, the electrons undergo spin polarization and then enter another layer of the magnetic material[74]. Angular moment transfer occurs between the spin carried by the electrons and the local magnetic moments in the magnetic material. It is this interaction that allows for the change of state of the magnetic moments that induce magnetic switching.

SOT has two components: in-plane damping-like (DL) torque and out-of-plane field-like (FL) torque. The DL torque has the form $\mathbf{m} \times \sigma \times \mathbf{m}$ and FL torque has the form $\mathbf{m} \times \sigma$[234], where $\mathbf{m}$ is the magnetization and σ is the spin polarization. In literature, the damping-like torque is usually referred to as the longitudinal (Slonczewski-like) component that acts like an effective magnetic damping on the magnetic moment and the field-like torque that is usually referred to as the perpendicular (or transverse) component acts on the magnetic moments like an effective magnetic field[155].

CHAPTER 4: LOCAL AND NON-LOCAL MEASUREMENT TECHNIQUES FOR SPINTRONICS

It is critical to understand the spin propagation within a spin conducting medium for the field of spintronics. In order to accomplish this, material and device geometries need to be considered. It is common to see device geometries catered to either a non-local detection of spin or a local detection of spin transport through a material. In this chapter we outline these measuring techniques for the detection of spin currents in a non-local and local geometry. We will focus on electrical detection of spin transport via the inverse spin Hall effect, although there are others[145]. Details of the device fabrication will be discussed in Chapter 4.

4.1. NON-LOCAL DEVICES

The early days of non-local detection of spin currents involved devices known as non-local spin valves (NLSV)[112], where two ferromagnetic strips inject and detect a pure spin current flowing through a nonmagnetic metal channel. We use a similar device scheme for our non-local spin transport detection geometry outlined in Figure 4.1. Instead of ferromagnetic sources and sinks of spin, we adopt metals with large spin-orbit coupling[141,212,220,236,282]. The spin current will flow through our sample of study in a similar manner to a NLSV and is detected on a different metallic wire some distance away.

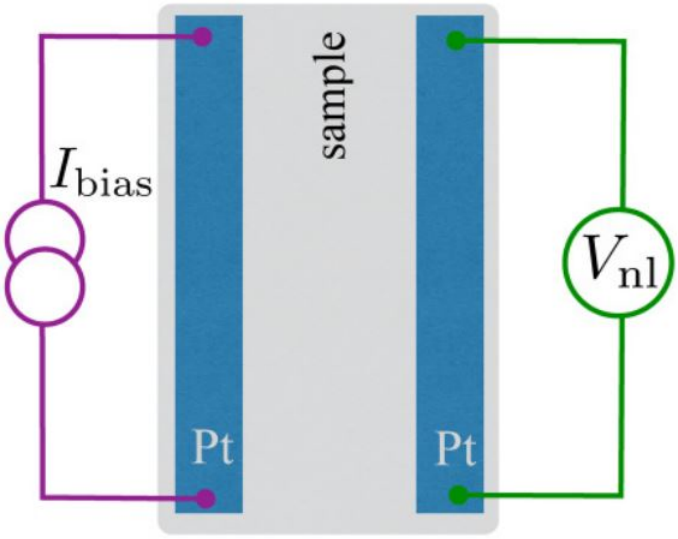

Figure 4.1: Cartoon schematic of a simplified non-local device. Two non-magnetic metals with large spin-orbit coupling, in this case platinum (Pt) wires, inject a spin current via the spin Hall effect (SHE), the spin current flows through a spin transport medium, and is detected elsewhere via the inverse spin Hall effect (ISHE). Illustration adapted from [202].

From Figure 4.1, a bias current flows through a metallic wire with a sufficiently large spin-orbit coupling, in this case Pt, where charge current is transformed into a spin current via the spin Hall effect (SHE). At the interface of the injection wire and the sample, spin angular momentum from the conduction electrons of a preferred spin state is transferred at the interface, causing a change in spin chemical potential, and ultimately a flow of spin angular momentum through the sample. If the distance between the injection and detection sites is not too large where relaxation mechanisms cause a decoherence in spin angular momentum flow, then at the interface of the sample and spin detection wire, the spin angular momentum is again transferred, and transformed into an electric field via the inverse spin Hall effect (ISHE) [238]. If the sample has a large resistivity, then a pure spin current, that is a spin current in the absence of charge, can flow through the sample and be detected as a negative

non-local resistance. Otherwise, complications can arise when charge is allow to accompany spin flow.

4.2. HALL BAR LOCAL DEVICE

It is also common to see studies using a more local geometry for the detection of spin flow in experiments involving spin Seebeck effects[73,214,262], spin pumping[107], and others[39]. Traditional spin Seebeck experiments, have samples mounted between two Peltier elements for thermal gradient control[26,111,229] and a two wire configuration to measure resulting voltages. This method of measuring spin Seebeck voltages are often limited by device designs that typically restrict access to temperatures below room, unless special design considerations are met[88,126,271]. Beyond the device restrictions, the generated thermal gradient are often assumed to be uniform across boundaries (i.e. the temperature difference measured between heater elements often divided by the thickness of the heat sink is often reported). This assumption neglects the various thermal conductivities of the films as well as the interfacial thermal conductivities that are critical, thus these experiments are difficult to replicate in other laboratories[229,230].

The local heating method used in some of our experiments to explore spin Seebeck effects at low temperatures (schematic seen in Figure 4.2) takes inspiration from other groups[73,214,262].

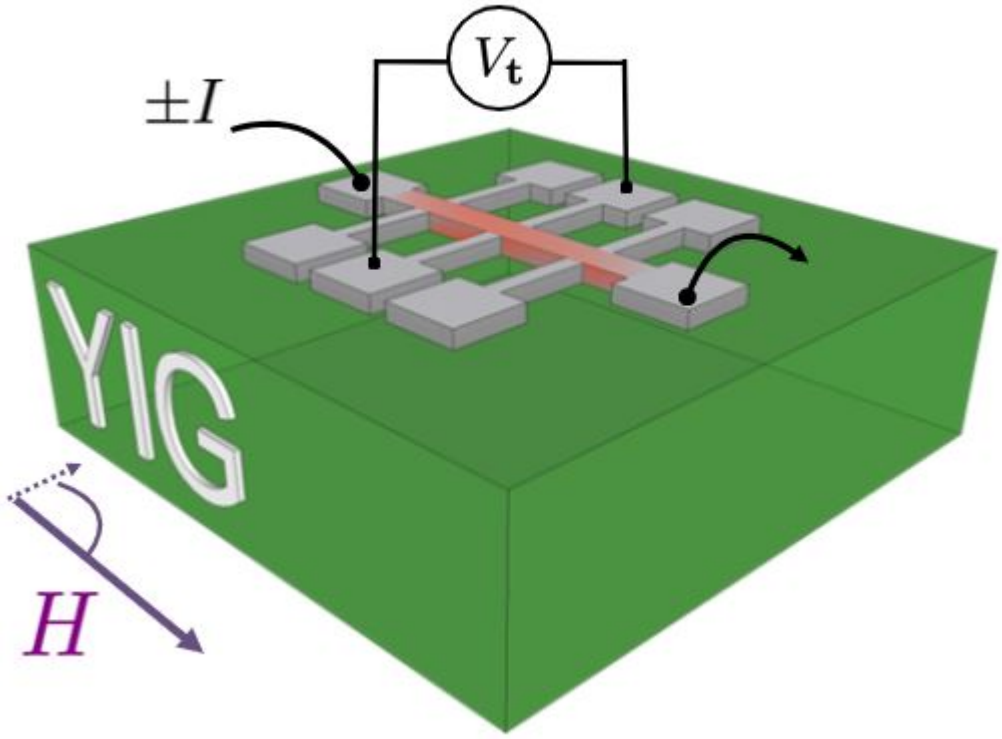

Figure 4.2: A cartoon illustration of the local heating method used in spin Seebeck experiments. Wires are ultrasonically bonded to pads of a Hall bar for the injection of a dc current, I, and the detection of a transverse voltage, V_t. The red region represents the development of a thermal gradient due to Joule heating.

In this method, a DC current produces a thermal gradient via Joule heating and voltage taps are used to detect the resulting transverse voltages. For our experiments using a ferromagnetic insulator, the thermal gradient creates a nonequilibrium population of magnons to carry the flow of spin angular momentum from the ferromagnetic insulator to the device. Spin angular momentum is transferred and turned into a transverse voltage via the ISHE. A current reversal method is employed, in which the DC current switches polarity with magnetic field sweeps, and due to the symmetries of the transverse signal the voltage measured can be broken into thermal and electrical components. The resistive contributions obey $V_{res}(+I) = -V_{res}(-I)$,

while the thermal component obeys $V_{SSE}(+I) = V_{SSE}(-I)$, thus, from the current reversal technique, we have:

$$\begin{aligned} V_t(+I) + V_t(-I) &= V_{res}(+I) + V_{res}(-I) + V_{SSE}(+I) + V_{SSE}(-I) \\ &= V_{res}(+I) - V_{res}(+I) + V_{SSE}(+I) + V_{SSE}(+I) \\ &= 2V_{SSE}(+I). \end{aligned}$$

It is important, however, to note that this method is not immune to other effects entangling along side the spin Seebeck voltage such as anomalous Nernst effect[32,124,188,246,272]. Because of this, careful analysis of the signal is required. The electrical component of the transverse voltage contains signals from spin Hall magnetoresistance[4,76,163] and anisotropic mangetoresistance[4,44,58]. Careful measurements must be made to separate these effects from each other.

4.3. 8-TERMINAL STAR PATTERN

Another device geometry to study spin transport in materials is a 8-terminal star device or asterisk device[28,37,38,80,198]. An illustration of the device geometry can be viewed in Figure 4.3.

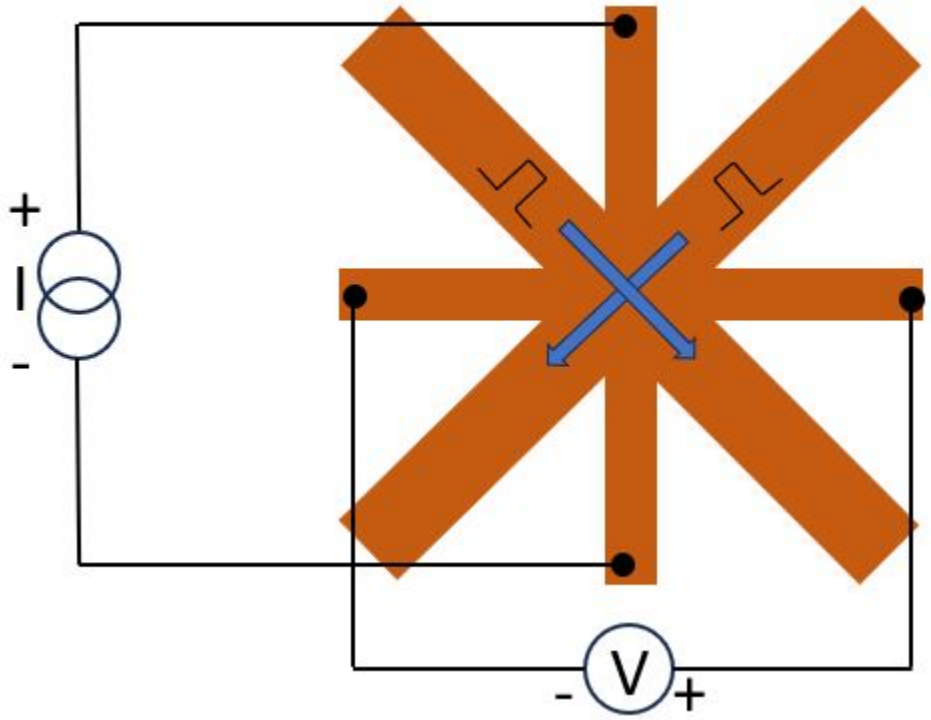

Figure 4.3: Device schematic of an 8-terminal star pattern to measure spin-orbit torque responses. Blue arrows indicate large DC pulsed currents to re-orient the magnetic structure of a magnetic material. I is a small current in the range of several μA and V is the voltage taps used to measure changes in resistance after the large DC pulse current. Figure adapted by[38].

In these types of devices a large DC pulse current density, typically in the range of several tens of MA/cm^2, are used to electrically control magnetic states of a material. These pulsed currents electrically control the magnetic material order parameter by inducing on of two types of spin-orbit torques (SOTs): either a fieldlike torque ($\partial_t \mathbf{m}|_{FL} \sim \mathbf{m} \times \mathbf{p}$[183,259]) or antidamping torques ($\partial_t \mathbf{m}|_{AD} \sim \mathbf{m} \times (\mathbf{m} \times \mathbf{p})$[143,224]), where $\mathbf{m}$ denotes the orientation of a magnetic moment and $\mathbf{p}$ represents the nonequilibrium spin polarization. These torques transfer spin angular momentum to the magnetic moment of a magnetic material and have the potential to switch their orientation. One measures longitudinal and transverse resistances and notes the changes

in resistance when switching the orientation of the magnetic order parameter after pulsing with a large current. Differences in resistances based on the direction of the pulse current is indicative of spin related phenomena occurring in the sample.

When the large current pulse, or can be viewed as a magnetic pulse, acts on the magnetic moments of a magnetic layer in a sample, the magnetic moments begin to oscillate, and these oscillations can create torques on adjacent materials near the interface. It is here where angular momentum is transferred from the oscillating magnetic moments to unperturbed moments in an adjacent layer via spin-transfer torques (STT). The angular momentum travels in the adjacent layer before completely dephasing and is converted into a voltage via inverse spin Hall effect.

CHAPTER 5: DEVICE FABRICATION

In this chapter we discuss the operating principles of a scanning electron microscope (SEM) and describe the electron-beam lithography process used to create our devices seen in later chapters as well as the photolithography process. These processes and chemical development are standard use in the experimental work discussed in later chapters.

5.1. SCANNING ELECTRON MICROSCOPE INTRODUCTION

In Figure 5.1, we illustrate, in a blown up cartoon schematic, the inside of a typical scanning electron microscope (SEM) system. The generation of a coherent beam of electrons starts with the filament. In most SEM systems the filament will be either made of tungsten or lanthanum hexaboride (LaB_6). A sizable charge current is sent through the filament in order to thermally eject electrons. The thermally ejected electrons converge and are accelerated with an electric potential on the order of several kVs via the Wehnelt cylinder. The electron beam is condensed again through a series of condenser lens and shaped by the electromagnetic coils. The final stage of the formation of a electron beam is at the double deflection raster coils where magnetic fields are used to deflect the beam and allow scanning in the X and Y directions of the sample.

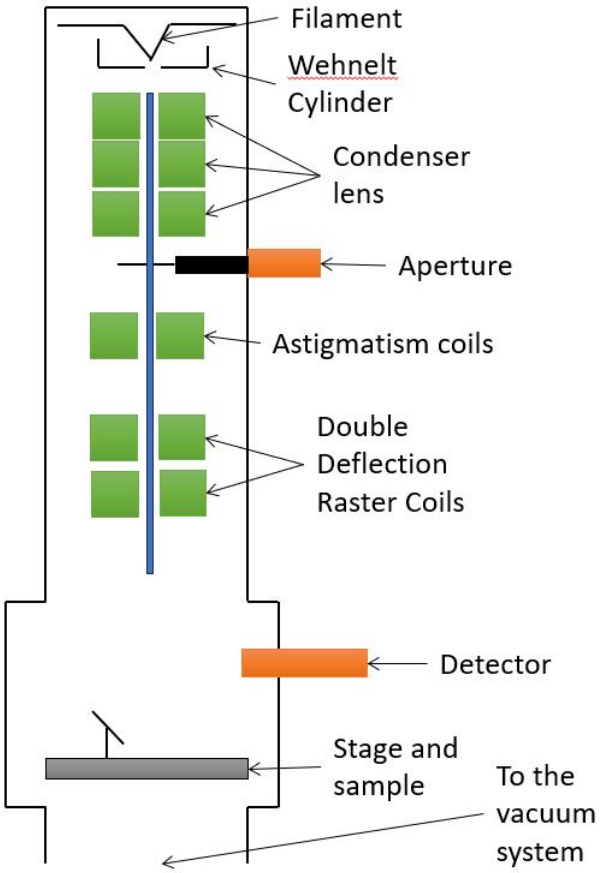

Figure 5.1: Schematic view of the internal working of a scanning electron microscope (SEM) system. This schematic outlines the internal components responsible for forming a condensed beam of electrons and detection. Illustration adapted from [62].

The electron beam can then interact with the sample for imaging (detecting backscattered or secondary electrons to form an image) or for device fabrication (where a resist coasting on the sample is charged by the electron beam in the shape of the device). The interaction the electron beam has with the sample is depicted in Figure 5.2.

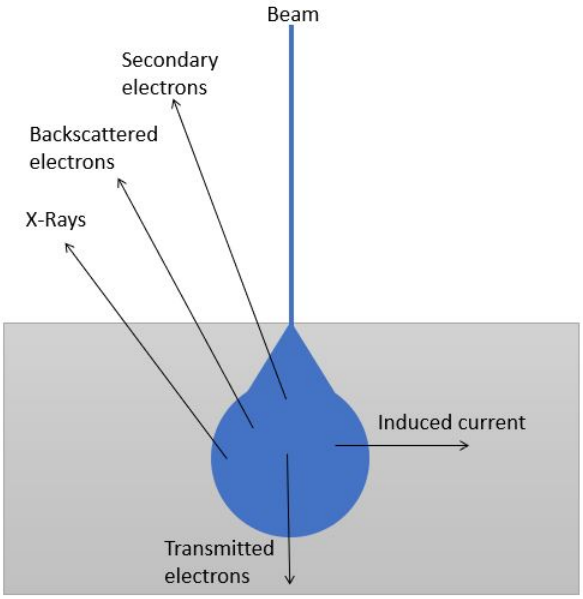

Figure 5.2: An illustration of the interaction between the beam of electrons and specimen highlighting the activation region and types of electrons that result from scattering events within the specimen. Illustration adapted from [62].

The interaction of the beam with the specimen forms an activation region, the teardrop shaped blue region in Figure 5.2. Within the activation region, several scattering mechanisms results in secondary electron ejections, backscattered electrons, or even X-rays. There are several uses of a scanning electron microscopy that span beyond just imaging the surface or nanopatterning devices. With specialized equipment, one can detect x-rays that correspond to a "fingerprint" of an element in a sample or image the cross section of a heterostructure for interface analysis.

5.2. ELECTRON BEAM LITHOGRAPHY

The electron beam lithography (EBL) begins with sample preparation. A sample is chosen and thoroughly cleaned with acetone, isopropyl alcohol, methanol, and then dried with N2 gas. If needed, samples are cleaned with a argon plasma etch to remove contaminants from the surface. Samples are pre-baked at 180°C for 60 seconds to promote adhesion between polymer resists and the sample surface. Next,

samples are placed in a spin coater where 2-3 drops poly(methyl methacrylate-co-methacrylic acid), MMA (EL 8.5) MAA, is delivered to the sample via a pippet, and spun at 500 rpm for 5 seconds and then 2000 rpm for 45 seconds. The samples are then baked again at 180°C for 60 seconds. This is repeated once more for the poly(methylmethacrylate), PMMA, resist.

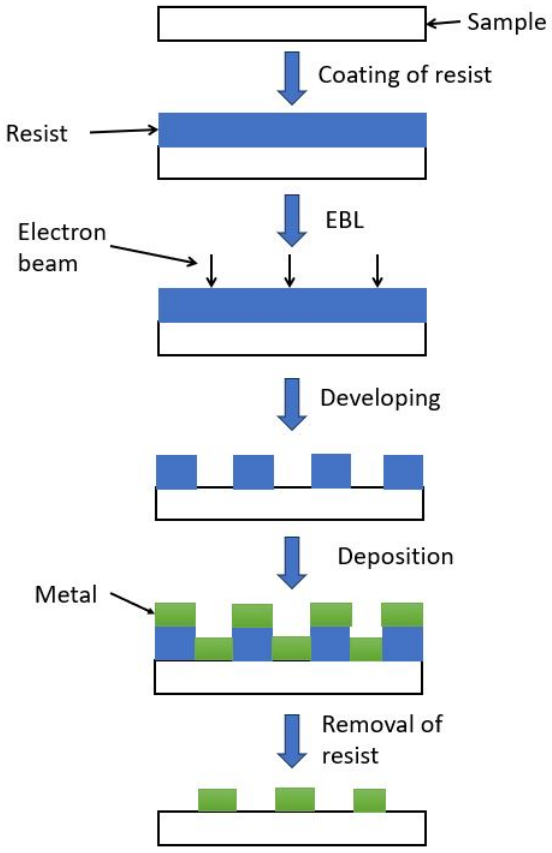

Figure 5.3: An overview of the electron beam lithography (EBL) procedure. Illustration adapted from[129]. A substrate is coated in a layer of resist and exposed to a beam of electrons that charge section of the resist that will become the device. A chemical development procedure follows to remove the charged resist. Afterwards, metal is deposited over the entirety of the sample surface and a final chemical lift-off removes unwanted material from the devices.

Using a nanometer pattern generation system (NPGS) software in combination with the SEM instrument, the electron beam is programmatically controlled

to traverse the specimen and expose precise sections of the resist layer. The long polymer strands are reduced to smaller components from the exposure. A chemical developer such as methylisobutylketone (MIBK) dissolves the exposed areas of the resist layer. Afterwards, a deposition step results in a metallic coating. The deposition techniques used in the experiments that follow are thermal evaporation and sputtering; however, there are a variety of other deposition techniques that exist[48,56,82,96,133,147,195,219,221,235]. Finally, the samples are submerged in an acetone bath and ultrasonically cleaned to remove leftover chemical resist and leaving behind a finished device.

Figure 5.4 illustrates cartoon diagrams of thermal evaporation and sputtering techniques.

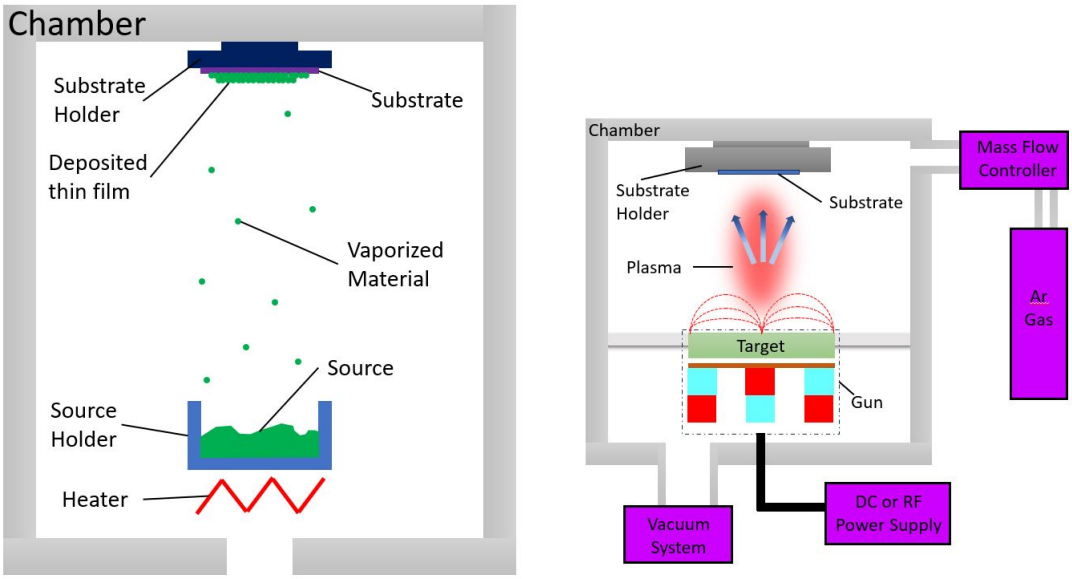

Figure 5.4: Cartoon diagrams that represent the thermal evaporation process (left) and sputtering (right). Illustrations adapted from[185].

For thermal evaporation, a source is heated with a large applied electric current that eventually boils off material that, in the end, make their way upwards and stick to a substrate. As for sputtering, the source material is bombarded by a high energy plasma created from an Ar gas environment. When momentum transfer is sufficient

to overcome the binding energies of the surface atoms of the source, the material is ejected from the source and rise upwards to a substrate.

5.3. PHOTOLITHOGRAPHY

Several of our devices were fabricated using photolithography techniques. The process for photolithography, depicted in Figure 5.5, begins with cleaning the sample surface with a nitrogen gas gun to remove any dust and debris from the film. Once cleaned, the films are placed onto a spin coater and held in place with a vacuum. A pipet is used to transfer KL5310 positive photoresist or APOL-LO 3202 Hi-Res negative lift off photoresist on the film so that hte film is uniformly covered by the respective resist. The sample is then spun at 2500 RPM for 4 minutes to create a uniform layer of photoresist. Once the spin coat process is finished, the film is transferred to a hot plate set at 100°C and baked for 60 seconds. The films are then transferred to the optical lithography mask aligner and aligned under their respective masks. The samples are then exposed for 4 seconds for positive resist or 16 seconds for negative resist via a Quans 20W UV LED light with a wavelength of 395-400 nm. Following the UV exposure, the sample is baked again on the hot plate under the same conditions. The samples are transferred to plastic hemostats and then submerged in a 0.26 normal tetramethyl ammonium hydroxide photoresist developer. Positive resist is developed for 50 seconds and then agitated via the hemostat for 10 seconds before removing the sample from the developer and rinsing thoroughly with distilled water and then blown dry with nitrogen gas. The negative resist follows a similar process, but is only developed for 40 seconds. Under an optical microscope, samples are checked for quality.

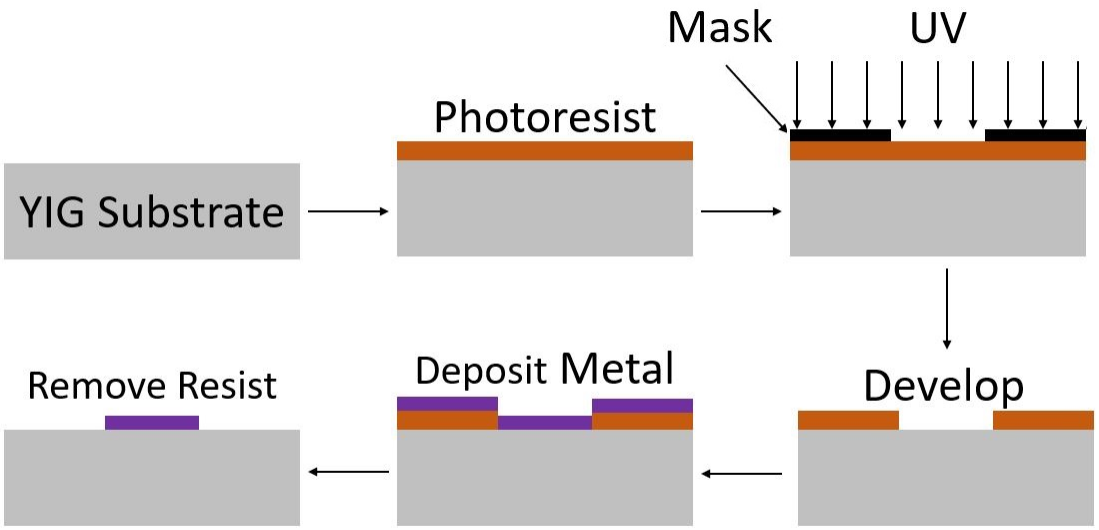

Figure 5.5: An overview of the photolithography process. Here a yttrium-iron-garnet (YIG) substrate is used. A uniform coat of photoresist covers the substrate surface. Using a mask with the desired device patterns and an ultra-violet (UV) light source, the device patterns are imprinted onto the photoresist. A chemical development follows and, if the devices are of high quality, metal is deposited over the entire substrate. A final chemical development removes the unnecessary metal and leaves behind our devices.

Samples undergoing positive lithography will then be transferred to the deposition chamber for ion milling. The samples are ion milled for a total of 90 seconds and then resistance of the film is measured to ensure no film remains except under the positive patterns, the ion milling is repeated as necessary to completely remove the film. Following the ion milling the positive resist is removed via an acetone bath and sonication to strip the positive resist from the patterned film. The films are cleaned with a sequential rinse of acetone and distilled water and then dried with nitrogen. Once the resist is fully removed the positive films may then undergo the negative photolithography process described below.

Samples undergoing negative lithography will be transferred to the deposition chamber for thin film deposition. The deposition chamber has a base pressure of

8E-8 Torr and the films are sputtered in a 3 mTorr Ar atmosphere. Following deposition, the negative photoresist undergoes a lift off process to remove unwanted material from the sample and leaves behind the devices. It should be cautioned that unlike EBL, photolithographic chemical resist is sensitive to ambient light sources. If samples with photoresist are left and exposed to ambient light sources, then it could be prematurely exposed and can ruin the quality of the photoresist.

CHAPTER 6: NON-LOCAL "SPIN" TRANSPORT IN AMORPHOUS GERMANIUM THIN FILMS

6.1. INTRODUCTION

In spin transport studies, a fairly common measurement technique used is the measurements of a non-local resistance[99,105,113,208]. In geometries that measure non-local resistances, there is a dc charge current through a metal, typically one with a high spin-orbit coupling, to generate a spin current and measured some distance away by another metal with high spin-orbit coupling. The important aspect of this non-local geometry is that the wire that injects spin into the system and the wire that detects the spin are isolated from each other. This results in experiments where one can measure pure spin currents in the absence of any associated charge currents flowing through the medium. However, in situations where the materials allows charge transport in conjunction with spin, the interpretation of the non-local resistance becomes difficult[202]

Amorphous semiconductors, including recently explored amorphous oxide semiconductors[159] have been studied extensively and have a range of important applications for large-area electronic devices. The strong disorder in the system leads to Anderson localization of the electronic states near the band edges and the boundary in energy between these localized states and extended states is the mobility edge[138,170]. In addition, a high level of defect states often forms near the middle of the gap, and nominally undoped amorphous semiconductors show electronic transport through these localized states via Mott's variable-range hopping mechanism, which has a characteristic temperature dependence at low temperature (T) given by:

$$\sigma = \sigma_\circ e^{-(T_\circ/T)^{1/4}}, \tag{6.1}$$

where $\sigma_\circ$ and $T_\circ$ are constants.

Here, we first present simple dc circuit models that clarify how dc leakage currents can generate non-local voltages in these experiments, and how they interact with various geometries of metal strips. We present charge conductivity and non-local resistance measurements of an amorphous germanium film. The results clearly show charge conductivity via the Mott variable-range hopping mechanism, indicating that amorphous germanium is best described as an amorphous semiconductor. The non-local resistance measurements show clear correlations with the charge conductance. We also clarify the conditions for observation of spin transport in non-0local resistance measurements in the presence of charge transport, and compare non-local resistance measurements made using two common measurement techniques: quasi-dc current reversal, and lock-in detection with a know range of ac frequencies. Data presented here shows that reactive components of the non-local measurement circuit can cause artifacts in t he quasi-dc measurement that mimic the spin transport signal in certain geometries, causing serious challenges for studies of systems such as antiferromagnets and disordered spin systems where the magnetic order is not easily manipulated.

6.1.1. CIRCUIT MODEL OF CHARGE LEAKAGE

Figure 6.1 shows a schematic view of a non-local spin transport experiment where spin in injected and detected via the spin Hall effect (SHE). Two strips of a metal film that supports spin-charge conversion (here characterized as a spin Hall effect, though any mechanism converting charge current to spin current could be employed) are in contact with a spin transport medium as shown in Figure 6.1(a). In the case of a purely insulating magnetic medium, the spin can excite magnons that flow to the distant contact, length L away, and be detected via the inverse spin Hall

effect (ISHE) when the spin current flows into the metal strip. If the spin medium also allows charge to flow, this leakage current can flow across the spin transport medium to the (typically) much lower resistivity metal detector, eventually returning to the opposite charge terminal as shown in Figure 6.1(b). Here, we show two of the many possible current paths as black lines. Note that electrons have negative charge, the electron drift velocity direction is opposite to the arrows shown, which indicate the direction of current flow. The portion of the current flowing along path $i_{c,1}$ will generate spin current according to the SHE. The portion of the current that follows path $i_{c,2}$ and similar paths can lead to significant current density, $\vec{j}$, present in the detector strip. According to Ohm's law, $\vec{E} = \rho\vec{j}$, where ρ is the charge resistivity, this current density must be accompanied by an electric field $\vec{E}$, which is parallel to the current as indicated by the orange vector. This electric field leads to a voltage drop on the Pt wire, which is measured at the terminals, V_{nl}. This voltage has the typical sign expected when current flows in a resistor (with positive V_{nl} vs I_{bias}). However, as shown in Figure 6.1(c), when current flowing in the current path $i_{c,1}$ leads to a spin current that is injected downward into the transport medium, it flows through the medium and then upward into the detector. The inverse spin Hall effect, assuming the detector has the same sign of the spin Hall angle as the detector, causes both spin up and spin down electrons to collect at the positive voltage measurement terminal when positive I_{bias} is applied, as indicated. In Open circuit conditions for the voltage measurement on the detector strip, the electrons cause a charge accumulation that leads to an electric field. As indicated in the figure again with an orange vector, this electric field points in the opposite direction as the field in Figure 6.1(b) and leads to the opposite sense of the potential difference. A measurement of this voltage as a function of bias current when the experiment is dominated by spin flow in the medium will show a slope of the IV curve that is negative. This is often taken as proof of spin transport, though we will show that certain purely electrical artifacts can also mimic this sign reversal.

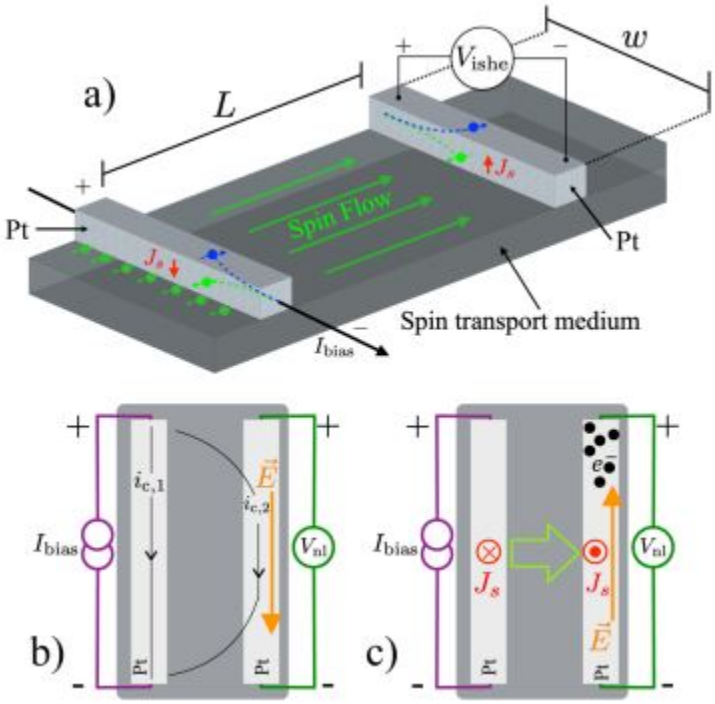

Figure 6.1: (a) Schematic of SHE-driven non-local spin transport. Typically, two Pt strips with length w along the charge flow direction, separated by a distance L, are placed in contact with a spin transport medium. A charge current, I_{bias}, driven into the injector strip (here shown at left) is converted to spin current via the SHE. This resulting spin current absorbed into this Pt detector generates a charge voltage via the ISHE. (b) A top-view schematic of a charge leakage contribution to a non-local voltage measurement. If the spin transport medium also allows charge flow, charge current can flow from the injector through the spin medium into a distant Pt strip. This travels down the typically much lower resistance Pt strip, generating a voltage with a positive sign with lead polarity chosen as shown by the + and − symbols. The charge then returns to ground by passing back through the spin medium. (c) Schematic view of spin transport in the same geometry, clarifying the direction of spin flow. The opposite sense of the spin flow in the injector and detector leads to a non-local voltage with the opposite sign from charge leakage.

The simple view of charge flow in a SHE-driven non-local transport experiment, shown in Figure 6.2(a), can be represented with the lumped-element circuit model shown in Figure 6.2(c). The requirement for the current to return to ground after any shunting by a nearby metallic strip means that, at an absolute maximum, the top half of the film is available to allow charge flow from the injector with resistance

R_{inj} to the detector with resistance R_{det}, with the lower half returning the current to low potential. Thus, the parallel charge conductance path is formed with effective shunt resistors $R_{vb}/2$, where R_{vb} is the total resistance of the spin transport medium between the relevant contacts, determined in our case by measuring current flow in response to a voltage bias. This avoids thermal, thermoelectric, and other non-ideal effects in typically very high resistance measurements. Any charge that flows across the spin transport film travels through the metallic detector, producing the voltage drop measured as a non-locl voltage, V_{nl}, before returning to ground. We calculate this voltage using

$$V_{nl} = I_{bias} R_{det} f \left(1 - \frac{R_{vb} + R_{det}}{R_{vb} + R_{inj} + R_{det}} \right), \tag{6.2}$$

which represents the relevant current division with the addition of the factor f, which accounts for the difference between the actual charge flow paths and those used in this highly simplified lumped-element model. We expect f to be a small number, and the experiments below suggest it is on the order of 0.012 for our work. When $R_{inj}<R_{vb}$ Equation 6.2 is simply

$$V_{nl} \approx I_{bias} \left(f \frac{R_{inj} R_{det}}{R_{vb}} \right), \tag{6.3}$$

and the term in parentheses is the expected non-local charge leakage resistance.

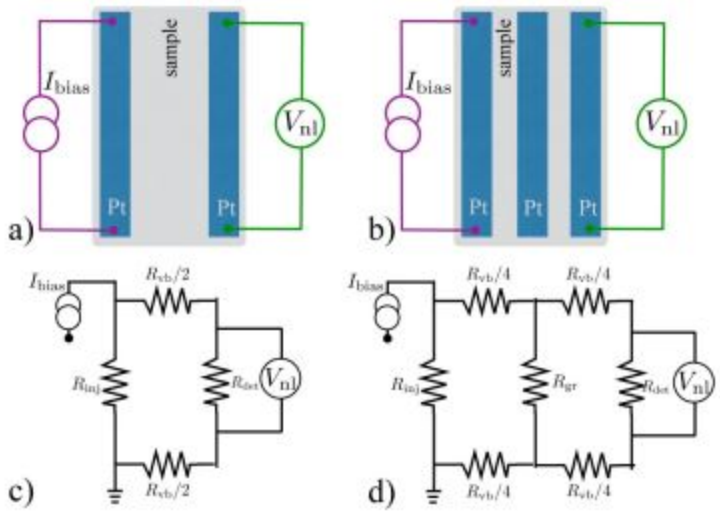

Figure 6.2: Schematic views and circuit models describing dc charge leakage in SHE-driven non-local spin transport experiments. (a) A top-down schematic view of a typical lead arrangement where Pt strips are in contact with a sample spin transport medium. (b) A similar view with a third metallic strip added between the spin injector and the detector. (c) Simplified circuit model describing charge leakage in the standard two-strip geometry. When R_{vb} is large compared to R_{inj} and R_{det}, a small portion of the total injected bias current flows on the right current path and generates a non-local voltage V_{nl} via leakage. (d) A modified circuit model demonstrates the possible reduction in V_{nl} in dc from the third metal strip.

We observe that intermediate metal strips can potentially reduce the leakage current in dc, though also add capacitance and inductance to the circuit and make any ac or effectively ac measurements less clear to interpret. In dc, we can model such an insertion of a "guard rail" as shown in Figure 6.2(b) using the circuit shown in Figure 6.2(d). Here, the third metal strip, with resistance R_{gr}, provides an additional low resistance region in the middle of the sample. The film resistance between the injector and detector at each step is approximately halved, so we take $R_{vb}/4$ to be the film resistance in each branch of the circuit. Again applying simple current division, we can write the guarded leakage voltage as

$$V_{nl,gr} = I_{bias} R_{det} f f^* \left(\frac{R_{inj}}{R_{inj} + R_{eff}} \right) \left(\frac{R_{gr}}{R_{gr} + R_{vb}/2 + R_{det}} \right), \tag{6.4}$$

where the effective resistance, R_{eff}, of all elements other than R_{inj} is

$$R_{eff} = \frac{R_{vb}}{2} + \frac{R_{gr}\left(R_{vb}/2 + R_{det}\right)}{R_{gr} + R_{vb}/2 + R_{det}}, \tag{6.5}$$

and f^* takes into account the different effective geometry of charge flow from the guard rail to the detector strip from the idealized model. As before, when R_{vb} is the largest resistance, Equation 6.4 is simply

$$V_{nl,gr} \approx I_{bias}\left(f\frac{R_{inj}R_{det}}{R_{vb}}\right)\left(f^*\frac{4R_{gr}}{R_{vb}}\right), \tag{6.6}$$

and the leakage resistance is reduced from the simple model of Equation 6.4 by the factor $4f^*R_{gr}/R_{vb}$. Assuming that the charge conductivity of the sample medium is uniform, then $f^* \approx f$, and with a value of R_{gr}/R_{vb} on the order of 10^{-2} or smaller, this factor could cause a reduction of leakage voltage by several orders of magnitude for purely dc measurements. This overly simple model makes a number of somewhat speculative assumptions. Two-dimensional finite element calculations, on both simple lead configurations and the more complicated geometries used in experiments, show similarly dramatic reductions in dc charge leakage, though these also rest on the assumption of a uniform conducting medium.

6.2. EXPERIMENTAL DETAILS

We prepared amorphous germanium films via thermal evaporation of Ge from 99.999% pure source material in high vacuum (approximately 10^{-6} Torr or 1.3×10^{-4} Pa) onto amorphous Si-N coated Si substrates at a rate of approximately 0.13 nm/s. Note that this deposition rate and base pressure, the film likely have significant defect atoms included in the disordered matrix. For amorphous germanium (a-Ge) we explored two methods for patterning metal leads to measure charge transport and test non-local spin transport. These were deposition of the sample

film on Si-N/Si substrates with pre-patterned strips of 40 nm thick Pt with a 10 nm thick Cr sticking layer, and patterning of Pt and Cu strips on the top surface of the samples via e-beam lithography (EBL) and lift-off. For the EBL lead patterns, we also prepared the lead patterns on a highly insulating Si-N coated Si substrate with no other film added. Figure 6.3(a) is a scanning-electron micrograph top-view of an example of the EBL-patterned leads. Figure 6.3(b) shows a cross-sectional view of these lead patterns, which we produced with three different injector-detector separations and, for one separation, with an additional Cu lead. To form these, we used a PMMA layer (Microchem 950 PMMA A3) with Co-PMMA underlayer [MMA(8.5) MAA EL 6], each spun for 5 s at 500 rpm then for 45 s at 2000 rpm and baked at 180°C. We sputtered platinum leads after reaching a base pressure of 4×10^{-8} Torr at 100 W in 3 mTorr of Ar, giving a growth rate of 0.125 nm/s. We evaporated the Cu leads after reaching a base pressure of 7×10^{-7} Torr at a rate of $\approx$0.14 nm/s. Before the Cu deposition, the sample film surface was Ar plasma cleaned in a separate vacuum chamber for 1 min.

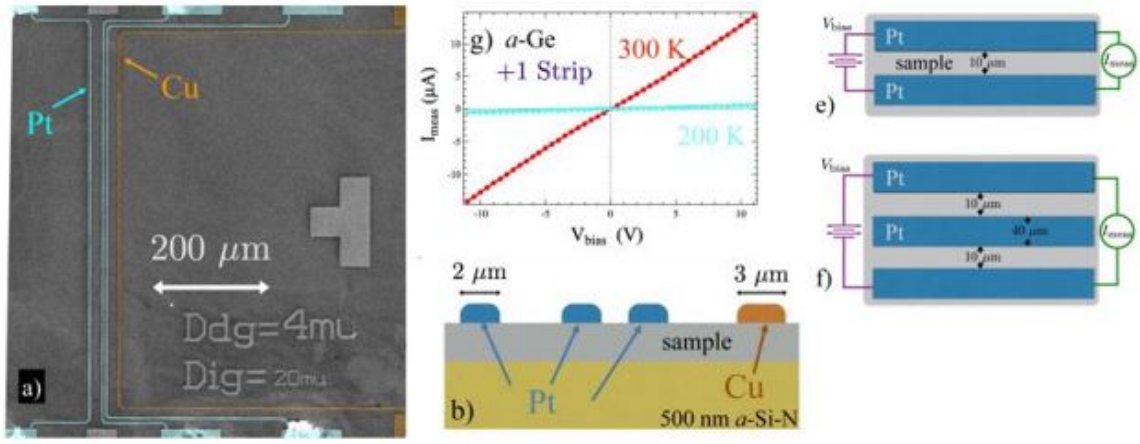

Figure 6.3: (a) False-color scanning electron micrograph of Pt and Cu leads patterned via EBL on a 75 nm thick a-Ge film. Leads shown in blue (orange) are 25 nm thick Pt (Cu). We produced three different patterns with varying Pt lead separations. (b) Cross-sectional schematic of the EBL samples with Pt and Cu leads width indicated. (c)-(d) Schematic views of the voltage-biased setup used to measure the resistivity of the amorphous semiconducting samples (distances indicated relate to pre-patterned leads). Since Pt has many orders of magnitude higher conductivity than the sample films, the total length of the current path used to determine ρ is only the distance between the Pt strips, as indicated. (e) Current measured, I_{meas}, vs voltage bias, V_{bias}, for the geometry shown in (c) for the a-Ge sample measured at 200 and 300 K for pre-patterned Pt leads shows predominantly linear response.

For all transport measurements, the substrates are mounted on the cold finger of a sample-in-vacuum cryostat using gold coated OFHC copper sample mounts. Leads are ultrasonically wire-bonded and a radiation shield installed to ensure an isothermal sample environment. Transport measurements use standard computer controlled source-meter equipment. Voltage-biased a-Ge film resistance were measured with a Keithley 2400 sourcemeter. We compare two methods for measuring the non-local IV and R: the "quasi-dc" measurements using either the differential conductance or "delta mode" measurement features of the Keithley 2182a/6221 nanovoltmeter and precision current source, and frequency-dependent ac measurements using a Stanford Research Systems 830 lock-in amplifier, using an external function generator and bias resistor to apply the ac bias current. Most experiments were performed at relatively

low bias current and used a 90 kΩ bias resistor that is much larger than the ≈1 kΩ resistance of the injector strips. To apply the largest bias currents (up to 7 mA), we used much smaller bias resistance (in some cases we used only the in-line lead resistance). Where this was done, we observed no qualitative change in the balance between in-phase and out-of-phase components of the ac signal.

6.3. RESULTS AND DISCUSSION

Before detailing the consequences of this hopping conductivity on non-local transport experiments, we first clarify the effective nature of the "delta mode" and differential conductance measurements performed with the Keithley nanovoltmeter (NVM) and current source. In Figure 6.4, we compare a series of electrical measurements on Pt strips formed via EBL on a highly insulating 500 nm Si-N layer deposited on a Si substrate. These strips, with geometry shown schematically in the inset to Figure 6.4(a), have the same layout as the device shown Figure 6.3(d), with a "guard rail" Pt strip placed between t he injector and detector strips, and the charge resistance between the Pt strips is unmeasurably large at all T described here. In Figure 6.4(a), we present the non-local voltage determined by numerical integration of the differential conductance voltage measured with the Keithley NVM in response to a series of excitation currents, I_{bias}, sourced by the linked Keithley current source. In both this measurement mode and the related "delta mode", the timing between voltage measurements is affected by a parameter termed "delay time" by the manufacturer. Figure 6.4(a) plots curves acquired for four different choices of this parameter, ranging from 2 ms (the shortest possible value) to 20 ms. Strikingly, the non-local VI curve has the negative slope often associated with spin transport in experiments with a spin conductive media (obviously absent here). The slope of the curve also clearly depends on the choice of the value of the "delay time". High values of this parameter (not shown) begin to display an apparent oscillatory response, though the overall negative slope vanishes.

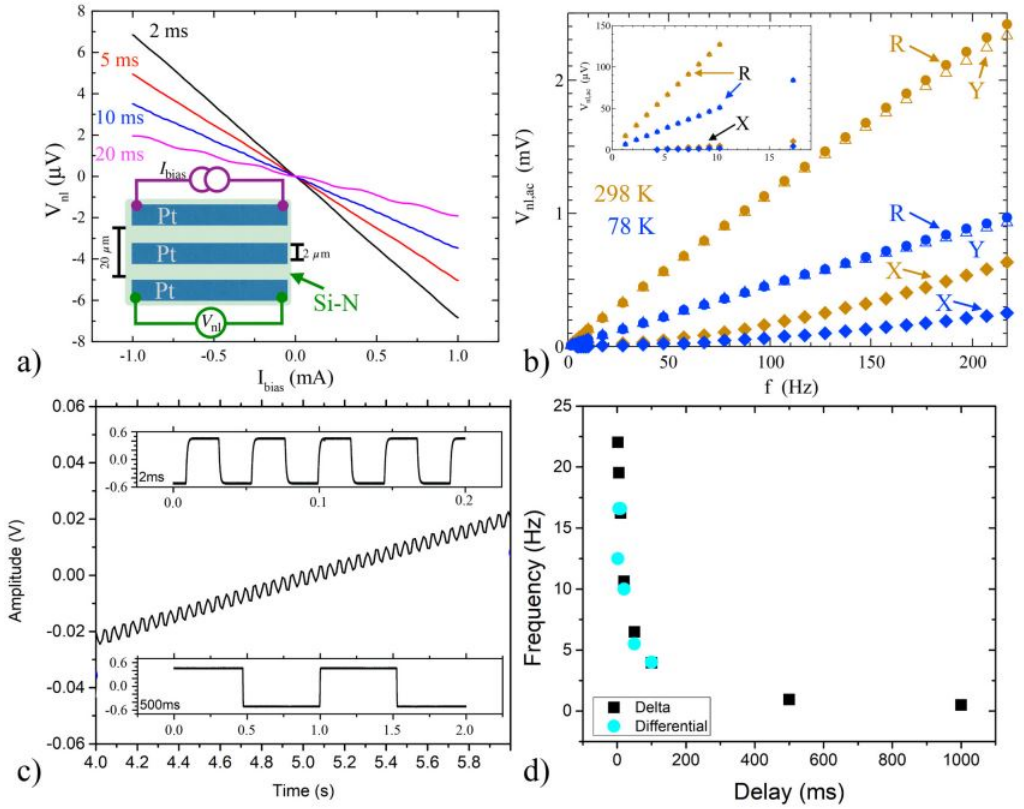

Figure 6.4: Comparison of "quasi-dc" and ac lock-in measurements of non-local voltage on a device with Pt strips patterned directly on Si-N, with no spin or charge conducting medium. (a) V_{nl} vs I_{bias} determined from the "quasi-dc" differential conductance method with four different choices of the delay time parameter, starting with the 2 ms value that is the default for this instrument. All show a spurious negative slope. Inset: Schematic view of the non-local leads with current bias and voltage measurement connections indicated. (b) $V_{nl,ac}$ vs f measured with a lock-in amplifier, where I_{bias} is a sine wave with frequency f and the V_{nl} is connected to the lock-in input. At both 298 K (orange symbols) and 78 K (blue symbols), the response is dominated across this frequency range by the out-of-phase response. Inset: Closer examination of the f<17 Hz range. (c) measurement of the time dependent voltage across the injector strip under "quasi-dc" excitation plotted vs time. The main panel shows the excitation pattern during a differential conductance measurement, and the upper and lower insets show the excitation during the "delta mode" measurements for two choices of delay time, as indicated in the insets. (d) Effective frequency of the "quasi-dc" measurements determined from the time dependent measurements plotted against the delay time parameter.

Measurement of the same exact Si-N device in the same cryostat with controlled ac excitation of $I_{rms} \approx 75\,\mu A$ and detection of V_{nl} with a lock-in amplifier indicate that the apparent negative VI slope measured by the "quasi-dc" method is an artifact arising from a large reactive component of the effective circuit. Figure 6.4(b) shows measured ac voltage response, $V_{nl,ac}$, to a well-defined ac bias current, including the in-phase component, X, out-of-phase component, Y, and the total magnitude, $R = \sqrt{X^2 + Y^2}$, for two different base temperatures, 298 K and 78 K. Despite a relatively low f, the out-of-phase component dominates the response at all f and T shown here. This is seen clearly by R and subsequently Y having much larger values than the in-phase response X. Note that measurements of a resistive load (for example, when both excitation current and voltage detection are attached to a single Pt strip) are dominated by the in-phase component, as expected. this large out-of-phase component of the response is perhaps not surprising when neither charge nor spin can flow from injector to detector, leaving capacitive and inductive coupling as the only mechanisms for modifying the detected voltage. However, the large reactive component presents a special challenge for the "quasi-dc" measurement.

Figure 6.4(c) plots the current excitation from the Keithley current source during the "delta mode" or differential conductance vs time. The main plot shows the current ramp used during differential conductance measurement, while the top and bottom inserts show the current excitation used in "delta mode" for two different choices of the "delay time" parameter discussed above. All of these signals are better understood as low-frequency ac excitations. We explicitly measure the period of these signals for a range of the "delay time" parameter and plot the resulting ac frequency vs the "delay time" in Figure 6.4(d). This shows that the default, short delay time used in these measurements is the functional equivalent of exciting a device with a square wave with f between 5 and 22 Hz. As we show in Figure 6.4(b) and is typical in non-local measurements of spin transport through nominally insulating systems [53], at these frequencies, the Si-N device is dominated by the out-of-phase response. This explains

the apparent sign inversion of the resistance as determined either from the VI curves measured with the Keithley differential conductance mode or the resistance reported by the "delta mode". here, the dc NVM is sampling an effective ac response at a time where the ac voltage has swung out-of-phase. Such as signal can, therefore, not be taken as strong evidence of spin transport without additional verification from magnetic field dependence or other control experiments.

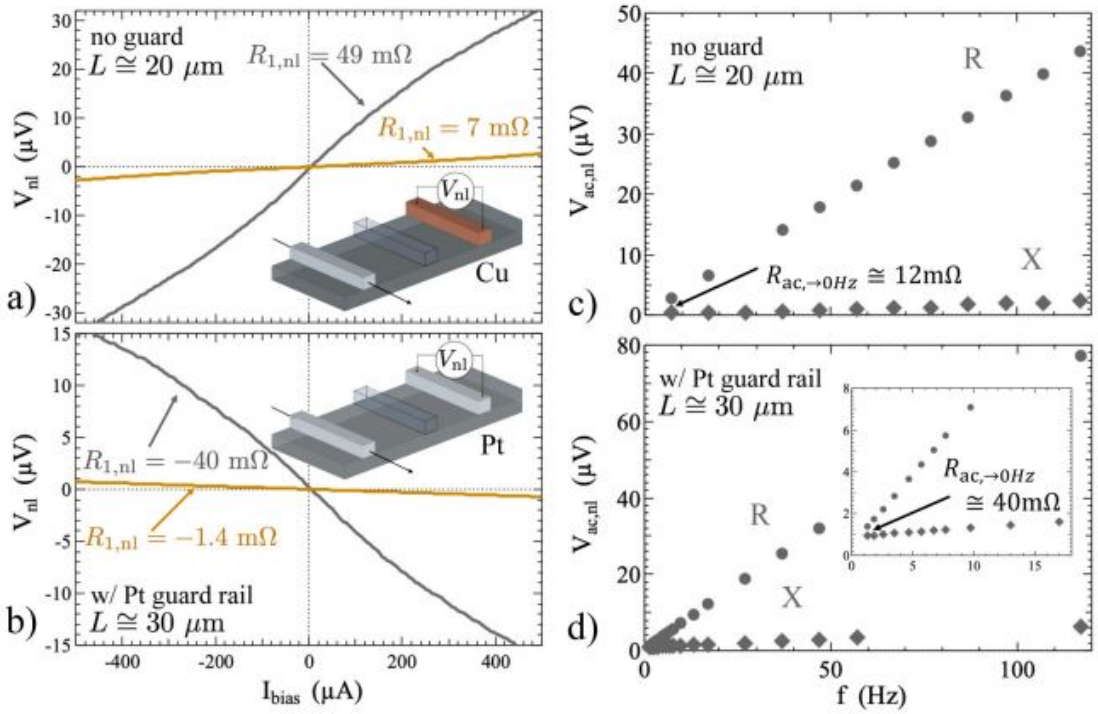

Figure 6.5: Non-local voltage measurements on 75 nm thick a-Ge. (a) V_{nl} vs I_{bias} using the "quasi-dc" measurements with Pt injector and Pt detector strips with $L \approx 20\,\mu m$ (gray line) and using a Pt injector and a Cu detector (orange line). Inset: Schematic view of the non-local setup with a Cu detector, with the possible third "guard-rail" strip shown in outline. (b) Similar V_{nl} vs I_{bias} measured with "quasi-dc" approach with the additional third strip in place. An apparent inversion of the sign of the non-local resistance occurs. (c) Lock-in amplifier measurements of the same device with Pt strips and no "guard rail", $V_{nl,ac}$ vs f with an ac excitation $I_{rms} \approx 5\,\mu A$ (similar behavior occurs for larger excitations). As seen on Si-N, the signal is dominated by an out-of-phase component. (d) Lock-in measurements of the device with the third Pt strip added, where the out-of-phase component is significantly increased. No negative values of non-local resistance are observed. Inset: Closer view of the f<17 Hz range shows the in-phase component always remains below the total signal magnitude.

Figure 6.5 compares non-local voltage measurements made with quasi-dc and ac lock-in techniques when an amorphous germanium film is placed beneath the metal strips. The quasi-dc measurements, measured at a delay time of 2 ms, compare four different strip geometries shown schematically in the insets in Figure 6.5(a) and 6.5(b). Figure 6.5(a) compares two "unguarded" geometries with strips separated by distance $L \approx 20\,\mu m$. The gray line presents results with both Pt injector and detector, whereas the copper-colored line was measured with Pt injector and a copper detector. Both curves have a positive slope at $I_{bias} = 0$, which could be interpreted as arising from charge leakage through the Ge. The values of these slopes, determined from the linear term of a polynomial fit to the curves, define the first-order non-local resistance $R_{1,nl}$ and are given for each curve in the figures. The lower voltage and smaller slope for the Cu detector, seen in the values from linear fits that are indicated in the figure, could arise form the lower resistance of the Cu detector strip, as suggested in Equation 6.4. The deviation of the IV curve for the Pt strip apparent here seems to match expectations for Joule heating, though we caution that the presence of the electrical artifacts related to the quasi-dc measurement complicate such an interpretation. Figure 6.5(b) shows similar data but with the additional Pt strip placed between the injector and detector, while somewhat increasing the overall distance between injector and detector at $L \approx 30\,\mu m$. Here, both quasi-dc VI curves invert sign, though the Cu detector again shows much smaller values than the Pt. Without confirmation from the ac lock-in measurements, this pattern could be interpreted as evidence of spin transport, clarifying the importance of the more controlled frequency-dependent non-local voltage measurements shown at right.

Figure 6.5(c) and 6.5(d) present $V_{ac,nl}$ vs f measured with a lock-in amplifier again on the same device with the same Pt strips and the same cryostat wiring. As with the controlled experiment on Si-N, the ac voltage is dominated by the large out-of-phase component, with $X<R$ even at frequencies below 10 Hz. This si true for both the case with no third Pt strip [panel (c)] and when the "guard rail" is inserted

[panel (d)]. Note the larger $V_{ac,nl}$ range in (d), indicating as in the Si-N case that one major consequence of the additional Pt strip is to increase the reactive components of the overall circuit, leading to a larger out-of-phase component. The inset shows a closer view of the low f region, again clarifying that the in-phase portion of the response is always less than the reactive, out-of-phase component. With the third Pt strip in place, at the ≈17 Hz effective frequency of the quasi-dc IV measurement, the out-of-phase components is 10× greater than the in-phase response. Without the third Pt strip, the out-of-phase response still dominates, but R is roughly half of the three-strip value. This significant shift in the reactive impedance drives the false inversion of sign between the experimental conditions of Figures 6.5(a) and 6.5(b).

In Figures 6.5(c) and 6.5(d), we also indicate the value of the non-local resistance determined from the in-phase ac voltage component for the two-strip "no guard" and three-strip "w/Pt guard rail" cases, extrapolated to zero f based only on the lowest frequency data points. If the Pt strip between injector and detector was actually acting to shield the detector from charge leakage, one would expect this value to be dramatically lower in the "guard rail" case. The experimental values provide no evidence of this, as $R_{ac,\rightarrow 0\,Hz}$ instead increases by a factor of 2-4× when the third Pt strip is added, and the overall distance between injector and detector increases. Though we caution that determining the true dc resistance accurately is difficult when such large reactive components of the circuit are present, the pattern shown here provides no clear evidence of the "guard rail" effect. The increase in $R_{ac,\rightarrow 0\,Hz}$ upon adding a strip and increasing L does not have a simple interpretation as charge leakage in a uniform conducting medium.

6.4. CONCLUSION

In summary, we presented charge resistivity and conductivity measurements on a-Ge films in geometries used for non-local voltage measurements. These show that the material should be viewed as an amorphous semiconductor with charge conductiv-

ity dominated by Mott's variable-range hopping. We also presented simple analytic models to help explain how charge leakage through such a medium can lead to signals in non-local voltage measurements that originate purely from charge. Finally, we also compared two experimental techniques to carry out non-local voltage measurements, including control measurements on Pt strips patterned on a Si-N coated Si substrate and Pt and Cu strips patterned on the a-Ge thin film. These show clearly that the fairly common automated "quasi-dc" measurement carried out with a linked nominally dc current source and nanovoltmeter actually applies an ac current with frequency of 22 Hz in the common default settings, and that this frequency falls in a range where our non-local voltage devices are dominated by reactive contributions to the circuit. This has the consequence that an inversion of the sign of a measured IV curve can occur. This suggests strongly that when measurements with these "quasi-dc" techniuqes are used, the sign inversion itself is not sufficient to prove spin transport in a given device.

CHAPTER 7: LARGE SPIN SEEBECK VOLTAGES IN THERMALLY-EVAPORATED CHROMIUM THIN FILMS DEPOSITED ON YTTRIUM-IRON-GARNET (YIG) SUBSTRATES

Spin-to-charge conversion and the reverse process are now critically important physical processes for a wide range of fundamental and applied studies in spintronics. Here, we experimentally demonstrate effective spin-to-charge conversion in thermally evaporated chromium (Cr) thin films using the longitudinal spin Seebeck effect (LSSE). We present LSSE results measured near room temperature for Cr films with thicknesses from 2 to 11 nm, deposited at room temperature on bulk polycrystalline yttrium-iron-garnet (YIG) substrates. Comparison of the measured LSSE voltage, V_{LSSE}, in Cr to a sputtered platinum (Pt) film at the same nominal thickness grown on a matched YIG substrate shows that both films show comparably large spin-to-charge conversion. As perviously shown for other forms of Cr, the LSSE signal for evaporated Cr/YIG shows the opposite sign compared to Pt, indicating that Cr has a negative spin Hall angle, θ_{sh}. We also present measured charge resistivity, ρ, of the same evaporated Cr films on YIG. These values are large compared to Pt and comparable to β-W at a similar thickness. Non-monotonic behavior of both ρ and V_{LSSE} with film thickness suggests that spin-to charge conversion in evaporated Cr, which we expect has a different strain state than previously investigated sputtered films, could be modified by spin density wave antiferromagnetism in Cr.

7.1. INTRODUCTION

The ability to generate a detectable charge voltage in response to the presence of a spin current[109,165], a flow of angular momentum in a material that can be mediated by conduction electrons[65,152] or magnons[152], is one of the most important tools of current spintronics research. These spin-to-charge conversion processes and charge-to-spin conversion phenomena have been described under various names in literature such as the spin Hall effect (SHE)[65,97,100,224], the Edelstein-Rashba effect[67,210], or a spin galvanic effect[84]. At the core of these phenomena is the spin-orbit coupling in the spin-conversion material or at a relevant interface that transform the spin angular momentum into a detectable voltage. It has been theoretically predicted that the scaling of spin-orbit coupling in materials will follow a Z^4 law[61], where Z is the atomic number. For this reason, the heavy metals, namely platinum, has been the workhorse of the spintronics community for it's large spin-orbit coupling[89,142,178,206].

The cost of platinum raises concerns for widespread use for applications, so it is essential to find a low cost spin conversion material with equal or better performance than platinum. Early spin pumping experiments, where spin currents are driven from ferromagnetic resonance (FMR) in a nominally insulating ferromagnet yttrium-iron-garnet, $Y_3Fe_5O_{12}$ (YIG), into Cr films where spin-charge conversion generates a measurable voltage via the inverse spin Hall effect (ISHE), were among the first to demonstrate significant spin-charge conversion in lighter metal films, including chromium[61]. This study also demonstrated that the resulting voltages in chromium were opposite in sign to both the other 3d metals tested and to platinum. This work was followed by studies on Cr thin films using thermal spin injection from a bulk YIG substrate[189,248]. In this technique, known as the longitudinal spin Seebeck effect (LSSE)[252], a thermal gradient applied at the interface between the insulating ferromagnet YIG drives a magnon-mediated spin current toward the interface between YIG and the adjacent metallic spin-conversion medium. Spin-to-charge conversion

processes generate a transverse flow of charge, which produces a detectable voltage via ISHE. An experimental diagram for the LSSE set-up can be viewed in Figure 7.1. One of the earliest works on LSSE on Cr/YIG systems investigated a sputtered thin film of Cr with a special focus on the question of whether the antiferromagnetic ground state plays a role in spin-to-charge conversion. The LSSE measurements of Qu,*et al*[189]. showed no clear features in the range between 30 and 345 K in their sputtered Cr on polycrystalline YIG sample. Likewise, a controlled sample of Pt on YIG from the same batch showed similar dependence to that of the sputtered Cr. Due to the similarities of the LSSE vs temperature measurements of both samples, the authors concluded that antiferromagnetism did not play a role in spin conversion in their Cr films.

Literature on Cr films suggests a complicated interplay of confinement, strain, and proximity effects that could play a role in spin-to-charge conversion under various circumstances. In bulk single-crystals, antiferromagnetism in Cr is the result of an incommensurate spin density wave (ISDW), where the spin of itinerant electrons is sinusoidally modulated[70]. The wavevector of this modulation is incommensurate with the atomic spacing of Cr, and the direction of this wavevector orients in different directions above and below a spin-flip transition temperature near 120 K[9,266]. The ISDW state affects a range of electronic properties and is highly sensitive to impurities[72]. Early investigations of the SDW nature of chromium thin films came indirectly from measurements of exchange bias[283]. Exchange bias is the shift in a hysteresis loop in a ferromagnetic/antiferromagnetic heterostructure caused by interfacial magnetic interactions between the magnetization of the ferromagnet and the Néel vector of the antiferromagnet . These measurements of exchange bias show not only an oscillatory nature, but also a suppression of the Néel temperature in systems such as epitaxial Fe/Cr[186] and permalloy/Cr[278].

Polycrystalline systems have also show unexpected spin density wave phenomena with samples retaining the antiferromagnetic state to temperature much higher than bulk Cr. Sputtered 35 nm thick polycrystalline Cr films on permalloy show no loss of antiferromagnetic ordering until 425 K, far above the Néel temperature in bulk single crystals[277]. This occurs due to a strain state in the Cr that drives a transition from the incommensurate spin density wave to a commensurate spin density wave, with stronger exchange and higher ordering temperature near 475 K in the absence of any finite size or grain effect. In polycrystalline thin film antiferromagnetic systems, the temperature probed by exchange bias is often related to the interactions between grains, called the blocking temperature, T_b. On reducing the thickness of sputtered polycrystalline films to roughly 10 nm, T_b dropped to 130 K[277]. These authors also identified an onset of exchange bias at Cr thickness near 6 nm. A mixed state where incommensurate and commensurate spin density waves coexist is also possible in polycrystalline films and has been shown to play a role in interfacial coupling, exchange bias and other electronic properties[30,277].

Electrical resistivity, ρ, is another key property of Cr thin films relevant to spin-charge conversion. Here, the literature also suggests a broad range of resistivities for various growth techniques and defects, though importantly ρ is often fairly large for a metal[29]. Such large ρ can be favorable for spin-charge conversion, since the spin-converting film often short circuits the transverse voltage generated from the spin conversion in various experiments. A high ρ with adequate spin-conversion efficiency can produce useful detectors for spin currents[94].

Here we present longitudinal spin Seebeck (LSSE) results measured near room temperature for chromium (Cr) films with thicknesses from 2 to 11 nm, deposited at room temperature on bulk polycrystalline yttrium-iron-garnet (YIG) substrates. We also present comparative measurements of a sputtered platinum (Pt) film at the same nominal thickness grown on a matched YIG substrate. We also provide measurements of the resistivity of our chromium thin films across a wide range of temperatures. The

thickness dependence of both the LSSE voltages and ρ of our chromium thin films versus thickness shows a nonmonotonic behavior. At the same thickness, the Cr thin film shows opposite sign to that of Pt and a LSSE voltage that is comparable in magnitude. This suggests that thermally-evaporated Cr can be a useful detector for spin currents.

7.2. EXPERIMENTAL DETAILS

We grew chromium (Cr) thin films via thermal evaporation from Cr plated tungsten rod sources in high vacuum ($\approx 10^{-6}$ Torr). We deposited Cr films with thickness, as determined by a calibrated quartz crystal mass balance, ranging from 2 to 11 nm onto $10\times2\times0.5\text{mm}^3$ bulk polycrystalline yttrium-iron-garnet (YIG) substrates at a rate of ≈0.3nm/s. The 2 nm Cr thin film had a measurable but high electrical resistivity immediately after growth, oxidized within a 24-48 hr period, and was no longer measurable. A second 2 nm Cr sample was thermally evaporated with a capping layer of a 2 nm Pd to prevent oxidation and was used for measurement. We attached voltage leads to the surface of the ends of these samples with indium dots, to perform resistance measurements and measurements of the LSSE voltage. WE clamp each sample between two Peltier elements of length $L = 5$ mm, each containing K-type thermocouples to monitor temperature. We use these to establish a stable ≈ 17 K temperature difference between the Peltier elements, with average sample temperature near room temperature. The resulting temperature gradient lies along the z-direction. The resulting LSSE voltage is measured with a Keithley 2182 A nanovoltmeter measured along the sample in the y-direction. The clamped sample is held inside a rotatable electromagnet, aligned to apply a field in the plane of the Cr film. When the field is perpendicular to the voltage leads, in the x-direction, the LSSE voltage is maximized and when parallel to the voltage leads the LSSE voltage is zero within error.

This type of apparatus, which is common for measuring the LSSE, robustly generates a thermal gradient at the interface between the YIG and metal film,

and reliably indicates resulting spin-charge conversion in the metal. However, comparison of resulting absolute values of the resulting LSSE voltage have been experimentally proven not to agree well across different experimental setups and different laboratories[229]. For this reason, we also prepared a comparison sample using the common spin Hall material, Pt. Here we sputtered a 10 nm thick film on a polycrystalline YIG substrate of the same dimension and cut from the same larger wafer. The Pt film was sputtered after reaching a base pressure of 4×10^{-8} Torr, at a rate of 0.125 nm/s at a DC sputtering power of 100 W. We measured the Pt/YIG sample in the same apparatus with the same experimental conditions and measurement parameters as the Cr/YIG samples.

The electrical resistivities we report were measured with a typical source-measure equipment either using four contacts wire-bonded near or on the indium connections after measurement of the LSSE voltage (for temperature dependent data, refer to Figure 7.3, or using the same two-wire leads as the LSSE voltage measurements (shown in Figure 7.4).

7.3. RESULTS AND DISCUSSION

Figure 7.1(a) illustrates a cartoon version of the experimental set-up to measure the longitudinal spin Seebeck effect (LSSE). We have a thermal gradient, represented by the blue-red gradient arrow, driving a thermal spin current from the YIG substrate (in green) to either a Cr or Pt (in gray). The voltage leads are attached with to the surface of the metal film along the long-axis of the film held by indium dots. An applied magnetic field, represented by an orange arrow, is directed into the plane of either the Cr or Pt metal. When the thermal gradient, magnetic field, and voltage leads or mutually perpendicular to each other a transverse voltage is detected via the inverse spin Hall effect (ISHE) resulting from magnon-mediated spin current produced from LSSE[200].

Figure 7.1(b) compares the LSSE voltage, V_{LSSE} vs applied field H for 10 nm thick thermally-evaporated Cr (green symbols) and sputtered Pt films (blue symbols).

This shows the reversal of the voltage with applied magnetic field, as one would expect, and shows the thermally-evaporated Cr to have an opposite sign to that of Pt. This is to be expected since Cr has a spin Hall angle, θ_{sh}, that is opposite in sign to that of Pt[189,253]. The most interesting aspect of this comparison is the large voltage the thermally-evaporated Cr has relative to the sputtered Pt sample at the same thickness; the voltage produced by the Cr is roughly 80% to that of Pt. The ratio of these two voltages would suggest that the thermally-evaporated Cr potentially has a larger spin-charge conversion compared to sputtered Cr, where the spin Hall angle measured via similar thermal spin injection from polycrystalline YIG was previously reported to be only ≈30% of Pt[189]. Note the large coercivitiy and complicated reversal patterns that are typical for bulk polycrystalline YIG substrates that we use as a spin source[190,191].

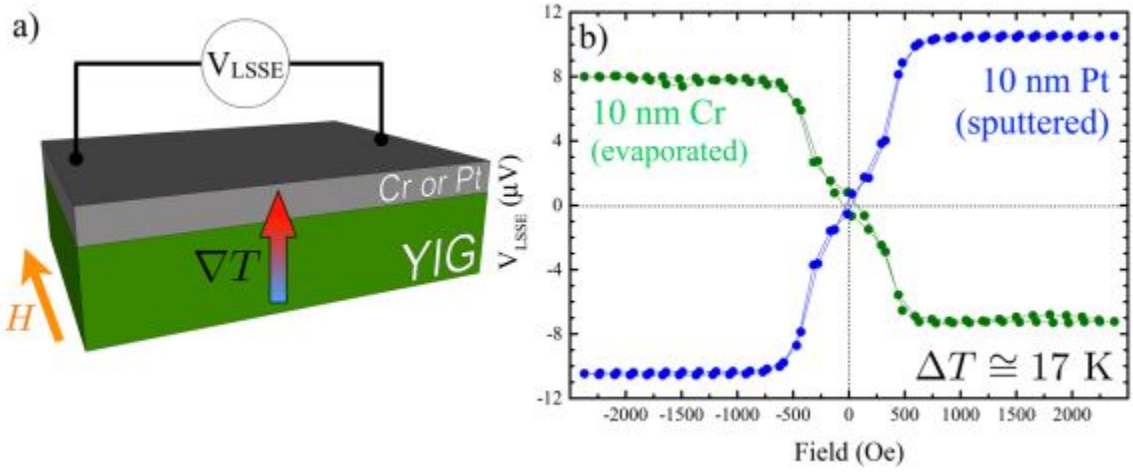

Figure 7.1: (a) Schematic of thermal spin injection via the longitudinal spin Seebeck effect (LSSE). A thermal gradient applied to the interface between bulk YIG substrate and Cr or Pt film drives spin current from the YIG into the metal, which is then converted to measurable transverse charge voltage, V_{LSSE}. (b) V_{LSSE} vs applied field H with a 17 K applied temperature difference for a 10 nm thick thermally-evaporated Cr film (Green symbols) and a 10 nm sputtered Pt film (Blue symbols). The sign of the resulting voltage for the thermally-evaporated Cr film is opposite in sign to that of the sputtered Pt film. The thermally-evaporated Cr film has a large thermally generated signal, roughly 80% that of sputtered Pt.

Figure 7.2 compares the V_{LSSE} vs applied in-plane magnetic field H for a series of Cr films of different thickness ranging from 2 to 11 nm. The simplest expectations of bulk spin-to-charge conversion suggest a monotonic drop in V_{LSSE} with increasing film thickness[248]. The thermally-evaporated Cr does not show this trend, seen clearly since the Cr/YIG samples in the middle range of thickness are plotted on a larger voltage scale (indicated by the dashed line wrapped around the plots). We also notice little change when annealing as indicated in the 10 nm Cr plot. A second 10 nm Cr/YIG sample was made and annealed immediately after growth in a vacuum cryostat at $\approx 100°$C for 2 hours. Annealing only caused a slight shift in both V_{LSSE} (seen as the red line in Figure 7.2) and ρ (shown in Figure 7.4). The excellent agreement between these two separate 10 nm thick samples also indicates that both the growth of the Cr and the measurement techniques are robust and repeatable.

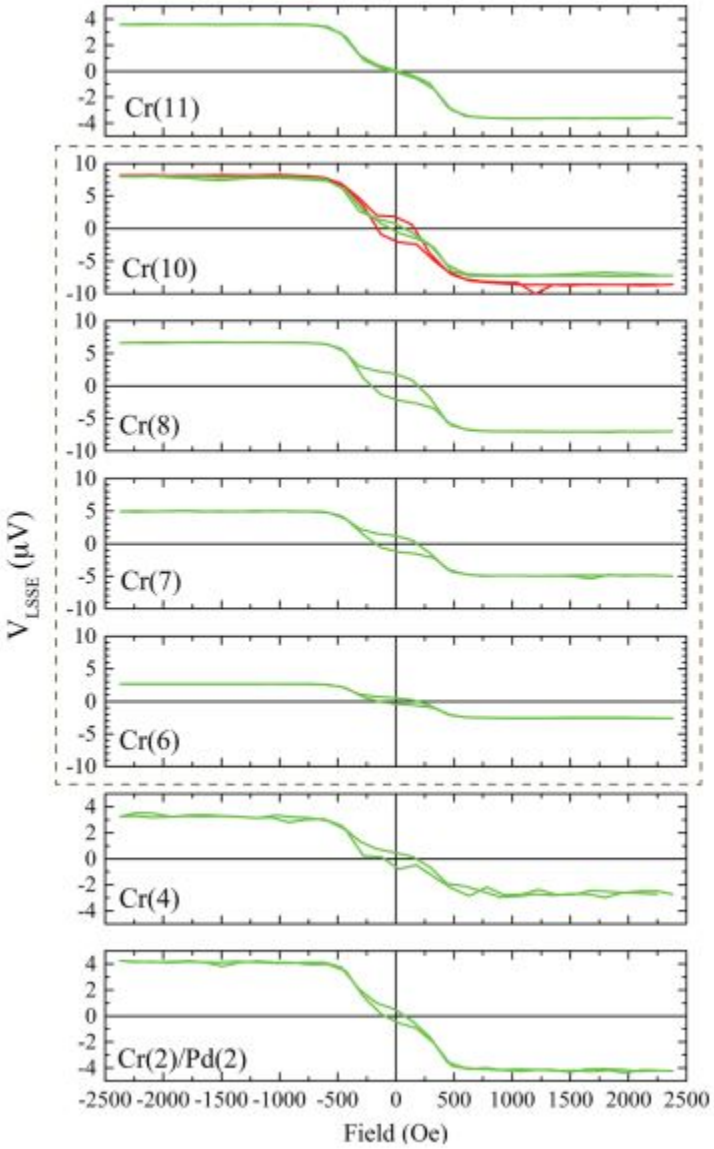

Figure 7.2: Longitudinal spin Seebeck voltage, V_{LSSE} vs applied in-plane magnetic field H for eight Cr/YIG films with thickness indicated, in units of nanometers, by the number in parenthesis. The thickness ranges from 2 nm to 11 nm. The thinnest Cr film is capped with a 2 nm Pd to prevent oxidation. Two 10 nm thick samples are shown, one (red line) that was annealed at ≈ 100°C in vacuum for 2 hrs after growth. Note the plots in the dashed box are plotted on a larger voltage scale than the other three plots.

Figure 7.3 plots the electrical resistivity, ρ, versus temperature, T, measured in a four-wire configuration for the 6 nm and 10 nm thick Cr samples. The thermally-evaporated Cr films show large values of resistivity, which is not unusual for Cr films, which are know to demonstrate a high degree of sensitivity to defects and film morphology[29,30,137,283]. The 10 nm thick film has essentially constant resistivity over the measured temperature range and the thinner 6 nm thick film shows resistivity values larger at low temperatures, comparable to values of a 200 nm sputtered Cr film[29], that decrease with increasing temperature. This negative slope of ρ with T is not typical for a metal, but often observed in Cr for certain ranges of T when various impurity atoms are added[72]. Despite ρ being much larger than the measured value of the 10 nm thick sputtered Pt film on YIG (Blue triangle in Figure 7.3), the Cr films still have smaller ρ values as compared to some polycrystalline films, such as the much thicker 200 nm sputtered film (black dashed line)[29]. Both thermally-evaporated Cr films have ρ values consistent with large values of residual resistivity, which in some studies has been correlated with mixed spin density wave (SDW) state[29,30]. These values of ρ are also comparable to those seen in other negative spin Hall angle materials, such as tungsten (gray dashed line)[94]. In both cases, the large resistivity values seem to promote a larger spin conversion in thermally-evaporated Cr films.

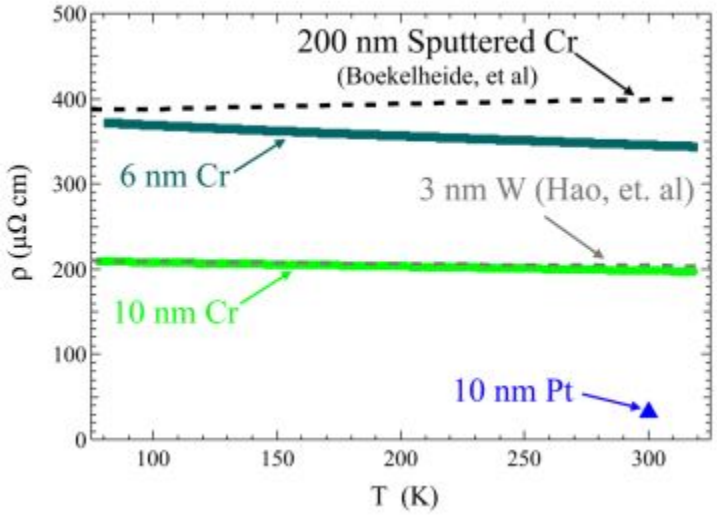

Figure 7.3: Charge resistivity, ρ, versus temperature, T, for two Cr films of thickness 10 nm and 6 nm and a 10 nm Pt film measured on the same samples as the longitudinal spin Seebeck voltages, V_{LSSE}, compared to literature values for 200 nm thick sputtered Cr[29] and a previously established negative spin-charge conversion material, 3 nm thick tungsten[94]. Both evaporated Cr films have large values.

In Figure 7.4(a), we plot the saturated absolute value of the spin Seebeck voltage, $|V_{LSSE}| = |V_{LSSE}(+H_{sat}) - V_{LSSE}(-H_{sat})|$ vs the thickness of the metallic layer for our thermally-evaporated Cr/YIG, our sputtered 10 nm Pt/YIG reference sample, and literature data for sputtered Cr[189]. In the given equation, $V_{LSSE}(\pm H_{sat})$, refers to the measured voltage at either a saturating positive applied magnetic field or a saturating negative applied magnetic field. Note that, we rescaled the literature data to match the $\approx 1.7\times$ larger applied thermal gradient used in our experiment; the published values for sputtered Cr are somewhat lower. The thermally-evaporated Cr spin-charge conversion is non-monotonic with thickness in this range, and it does not follow the simple expectations of a modified $1/t$ dependence[165,287]. Instead, the values become sharply larger above 6 nm, increases further in value of to 10 nm, and then sharply decreases at 11 nm. Note there are two values for the 10 nm thick Cr; one refers to the annealed sample that was previously discussed in this chapter (the green triangle that is slightly lower than the other). These longitudinal spin Seebeck

voltages not only increase within the 6 nm to 10 nm thickness range, but grows larger than the sputtered Cr sample and becomes comparable (as seen also in Figure 7.1(b)) to sputtered Pt at the same thickness.

Figure 7.4(b) compares the charge resistivity, ρ, to the thickness, t, near room temperature for the same set of samples. The uncapped thermally-evaporated Cr samples all show much larger ρ values, which is again non-monotonic with t, though with a different pattern than seen in V_{LSSE}. The thinnest thermally-evaporated Cr sample was capped with a thin 2 nm Pd film, which may be the cause for the much lower value for that sample. In literature, Pd has a large spin-orbit coupling and has been reported to show significant spin-charge conversion in some samples[6,241]. A thermally-evaporated Pd deposited on YIG showed $> 10\times$ lower V_{LSSE} than any of the thermally-evaporated Cr samples. As a result, we do not expect the Pd cap to significantly effect V_{LSSE} of the thermally-evaporated Cr.

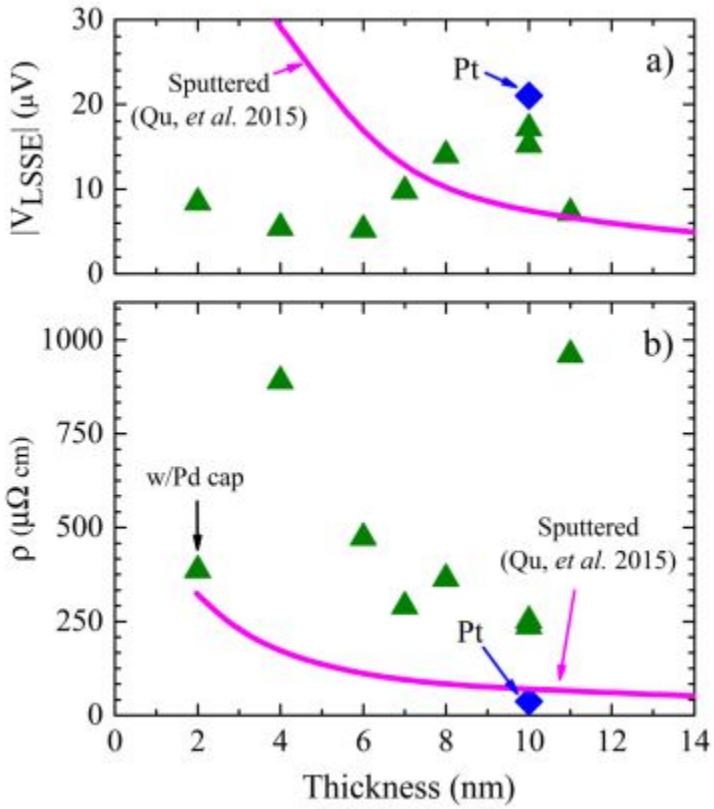

Figure 7.4: (a) Absolute value of saturated V_{LSSE} vs thickness comparing evaporated Cr (green triangles) and 10 nm thick Pt (blue diamond) to literature values for sputtered Cr (pink line) all scaled to equal applied thermal gradient, ∇T[189]. Estimated uncertainty is $\approx$ 5%to $\approx$ 10% on order of the size of the data points. (b) Charge resistivity, ρ vs thickness measured on the same samples as in (a).

Figure 7.5 compares the same samples using a measure of the overall spin-charge conversion, based on the typical theoretical analysis of the spin Seebeck effect. Thermally generated spin voltage, with the assumption of spin-charge conversion occurring in the bulk of the film via the spin Hall effect, is typically described by

$$V_{LSSE} = 2(CL\nabla T)(\rho\theta_{sh})\frac{\lambda_{sf}}{t}\tanh\left(\frac{t}{2\lambda_{sf}}\right), \tag{7.1}$$

where ∇T is the applied thermal gradient, ρ is the charge resistivity, θ_{sh} is the spin Hall angle, λ_{sf} is the spin diffusion length in the metal film, t is the metal film thickness, and C refers to the efficiency of spin injection from the YIG to the metal film[189,190,191] . From equation 7.1, there are three obvious ways of increasing the thermal signal: increasing ∇T, increasing L (which increases V_{LSSE} simply by integrating the same electric field over a longer path), and increasing ρ (which reduces simple electrical shoring of the generated voltage by charge flow in the metal film). We can rewrite equation 7.1 as

$$\frac{V_{LSSE}}{L\nabla T\rho} = 2(C\theta_{sh})\frac{\lambda_{sf}}{t}\tanh\left(\frac{t}{2\lambda_{sf}}\right), \tag{7.2}$$

such that the right-hand side depends only on t and spin-related properties of the heterostructure. Comparison of the quantity $|V_{LSSE}|/L\nabla T\rho$ between samples therefore removes the three trivial effects. With this view of spin-charge conversion, we see that both sputtered and thermally-evaporated Cr have a much lower spin-conversion efficiency than Pt (which is off the plot with a value of $3300\mu\mathrm{V}/\Omega$ cm K in Figure 7.5), but that the thermally-evaporated Cr retains roughly half the spin-charge conversion efficiency to that of sputtered Cr between 6-11 nm.

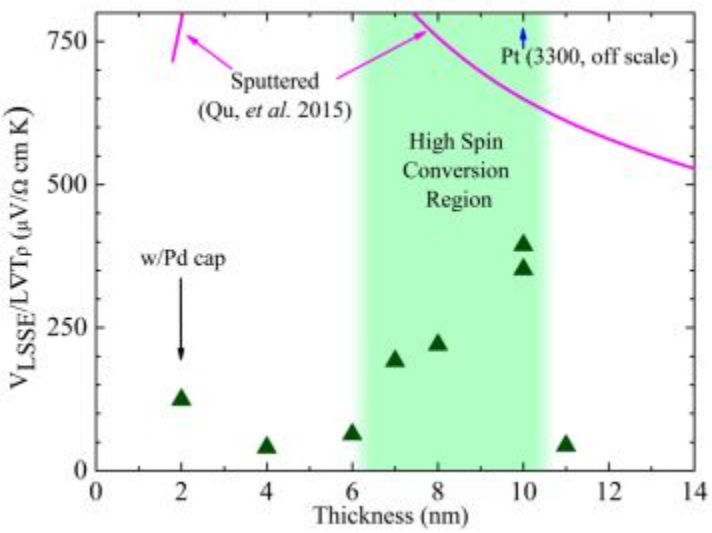

Figure 7.5: Comparison of the spin conversion efficiency, $V_{LSSE}/L\nabla T\rho$, for literature values of sputtered Cr (pink line) and thermally-evaporated Cr (green triangles). In the green highlighted region between 6 and 11 nm, the thermally-evaporated Cr develops a much larger spin-conversion efficiency, reaching about 1/2 to values reported for sputtered Cr at the same thickness. Pt (represented by the blue arrow) at 10 nm has the largest efficiency value of $3300\mu\text{V}/\Omega$ cm K.

As shown by the literature data for sputtered Cr, when well described by equation 7.2, λ_{sf} and θ_{sh} can be determined from these data. As shown in Figure 7.5, the thermally-evaporated Cr/YIG samples do not obey equation 7.2, instead showing essentially the same non-monotonic pattern seen in V_{LSSE}, again with sudden increase in spin conversion above 6 nm and sudden drop below 11 nm. This behavior with thickness suggests, as seen in earlier reports on exchange bias, that the evolution of strain in the thermally-evaporated film modifies the nature of the spin density wave, which in turn causes the sudden changes in spin-charge conversion. From our experiments, we cannot determine if this change is driven by modified coupling at the interface (represented by changing the C parameter), a change in the spin conversion itself (changing θ_{sh}), or a change in λ_{sf}. Indeed, the modification in the Fermi surface that is expected based on strain-induced changes of the nature of the spin density wave in Cr could affect any or all of these parameters. As the strain state of evapo-

rated and sputtered films are generally different [1,132,245], strain is a likely explanation of the very different charge and spin properties of thermally-evaporated and sputtered Cr films.

7.4. CONCLUSION

In summary, we presented evidence of large negative spin-charge conversion in thermally-evaporated Cr films on bulk polycrystalline YIG substrates using the longitudinal spin Seebeck effect. The large thermally driven spin voltages, which are larger than those previously seen in sputtered Cr for some thicknesses, are partly achieved due to large charge resistivity, which is comparable to negative spin-charge conversion materials demonstrated by others. A non-monotonic pattern in both the unscaled V_{LSSE} and that scaled by ρ for thermally-evaporated Cr suggests, as previouslyu seen in exchange bias experiments in Cr heterostructures, that changing thickness changes the film strain, which modifies the nature of the spin density wave electronic state of Cr, modifying the spin-charge conversion process. This demonstrates that, for thicknesses chosen in the optimal range, cheap and easy to prepare thermally-evaporated Cr films can be useful spin detectors in a range of spintronic and spincaloritronic measurements and applications.

CHAPTER 8: TEMPERATURE DEPENDENCE OF SPIN SEEBECK VOLTAGES OF THERMALLY-EVAPORATED CHROMIUM THIN FILMS DEPOSITED ON YTTRIUM-IRON-GARNET (YIG) SUBSTRATES

In this report, we experimentally demonstrate significant spin-to-charge conversion in our thermally-evaporated chromium thin film via the longitudinal spin Seebeck effect (LSSE). We present LSSE results between 78 K and 350 K for a 10 nm Cr thin film and a sputtered 10 nm Cr thin film deposited at room temperature on a bulk polycrystalline yttrium-iron-garnet (YIG) substrate. Furthermore, we present dimensionless sensitivity measurements, $dR/dT * (T/R)$, where our evaporated Cr shows two distinct peaks centered at roughly 350 K and 200 K. These two peaks likely indicate the separate Néel of the incommensurate and commensurate spin density wave antiferromagnetic states coexisting in a strain-driven mixed state. We make comparisons of our evaporated Cr to a sputtered Cr film on YIG from the same batch and to literature data for sputtered Cr of nominally the same thickness grown on similar bulk polycrystalline YIG substrate. The two sputtered films agrees reasonably well at all measured temperatures and the evaporated film agrees well above 200 K; below 200 K, there is a significant enhancement to the LSSE voltage for the evaporated film as compared to the sputtered films. This suggest the enhanced spin-charge conversion in our evaporated Cr thin film is a combination of finite-size effects and strain that leads to a modified spin-density wave nature with the underlying YIG substrate.

8.1. INTRODUCTION

Chromium (Cr) is an antiferromagnetic below the characteristic ordering Neél temperature. For bulk Cr this temperature is 311 K, but can vary with thickness[45,146,160]. The AF ordering in Cr is characterized by a spin density wave. In bulk single crystal Cr, the spin density wave is a incommensurate spin density wave (ISDW), where the spin of itinerant electrons is sinusoidally modulated incommensurately with atomic lattice spacing[71]. The modulation of the spin density wave can change above and below a characteristic temperature, known in literature as a spin-flip transition temperature[71], which is roughly 120 K in bulk Cr. The nature of the spin density wave (SDW) play a major role in the observed electronic and magnetic properties of Cr and are sensitive to impurities and strain[71,71,72]. For thin film systems, the nature of the SDW can be drastically altered from the reduced thickness of the film and accompanying strain and finite-size affects, leading to not only changes in Neél temperatures, but also in the spin-flip temperature as observed in various thin film Cr systems[27,81,135,203].

In thin film polycrystalline systems, where the polycrystallline nature of the films create a high degree of disorder, the SDW nature of Cr can be dramatically altered due to the degree of disorder and accompanying stress and finite-size effects. Depending on the degree of disorder in the film, polycrystallline thin film Cr samples can be magnetically characterized by an incommensurate SDW, commensurate SDW, or a mixed SDW state. The mixed SDW state includes the incommensurate spin-density wave and two different forms of commensurate spin-density waves[30]. In the mixed SDW state, the associated incommensurate and commensurate spin-density waves states are separated by temperature.

Our previous work in thermally-evaporated Cr thin films grown on polycrystalline yttrium-iron-garnet (YIG) substrates[26] investigated the spin-charge conversion for various thicknesses of evaporated Cr via the longitudinal spin Seebeck effect (LSSE). We showed that, for thicknesses between 6-10 nm, the evaporated Cr

thin films had an enhanced spin-charge conversion that was roughly half that of sputtered Cr. It was concluded that, due to the different strain states, as inferred from resistivity measurements, between sputtered and evaporated thin films[1,132,245], the strain in the evaporated Cr was modifying the nature of the spin density wave in Cr for certain thicknesses that, in turn, enhanced the spin-charge conversion. The largest enhancement seen in our experiment was for a 10 nm thermally-evaporated Cr thin film.

The investigations of Qu *et al*[189] on a 10 nm sputtered Cr thin film on a bulk polycrystalline YIG substrate showed no clear evidence of the antiferromagnetic nature of Cr playing a role in spin-to-charge conversion. Spin Seebeck effect measurements were taken over a large range of temperatures between 30 and 345 K. Their data on the longitudinal spin Seebeck voltage, V_{LSSE}, vs T showed a steady increase in V_{LSSE} between 350 and 250 K, followed by a roughly constant V_{LSSE} between 250 and 100 K, and a sharp decrease at temperature below 100 K. Comparative measurements were made with a sputtered 10 nm platinum (Pt) on an identical bulk polycrystalline YIG substrate and showed similar V_{LSSE} vs T behavior as the sputtered Cr film. Because of this, the authors concluded that the antiferromagnetic order in their sputtered Cr thin film did not play a significant role.

We continue our investigation on 10 nm thermally-evaporated Cr grown on polycrystalline YIG via the longitudinal spin Seebeck effect utilizing a local heating method with a current reversal technique[33,214,261]. A thermal gradient is applied at the interface between the insulating ferromagnet YIG via Joule heating that drives a magnon-mediated spin current toward the interface between YIG and the metallic spin conversion medium. Spin-to-charge conversion generates a transverse flow of charge, which produces a detectable voltage via the inverse spin Hall effect[2,275].

8.2. EXPERIMENTAL DETAILS

Bulk polycrystalline yttrium-iron-garnet (YIG) substrates were chemically cleaned and coated by a thin layer of photoresist. Using a mask, an array of $1 \times 0.1\text{mm}^2$ Hall bars, see Figure 8.1, were printed and developed via standard photolithographic and chemical development methods. We grew a thin 10 nm layer of chromium (Cr), as determined by a calibrated quartz crystal mass balance, via thermal evaporation from a Cr plated tungsten rod source in high vacuum ($\approx 10^{-7}$ Torr) onto a $10{\times}10{\times}0.5\,\text{mm}^3$ bulk polycrstalline YIG substrate at a rate of ≈ 0.3 nm/s. An additional 10 nm Cr sample, using the same photolithographic and chemical procedures, was sputtered on an identical YIG substrate. The base pressure was 8×10^{-8} Torr, the Cr was sputtered in a 3 mTorr Ar atmosphere at a rate of 0.44 Å/s. The samples were not intentionally heated and remain near room temperature during growth. Measurements of both resistance and longitudinal spin Seebeck (LSSE) effect were performed.

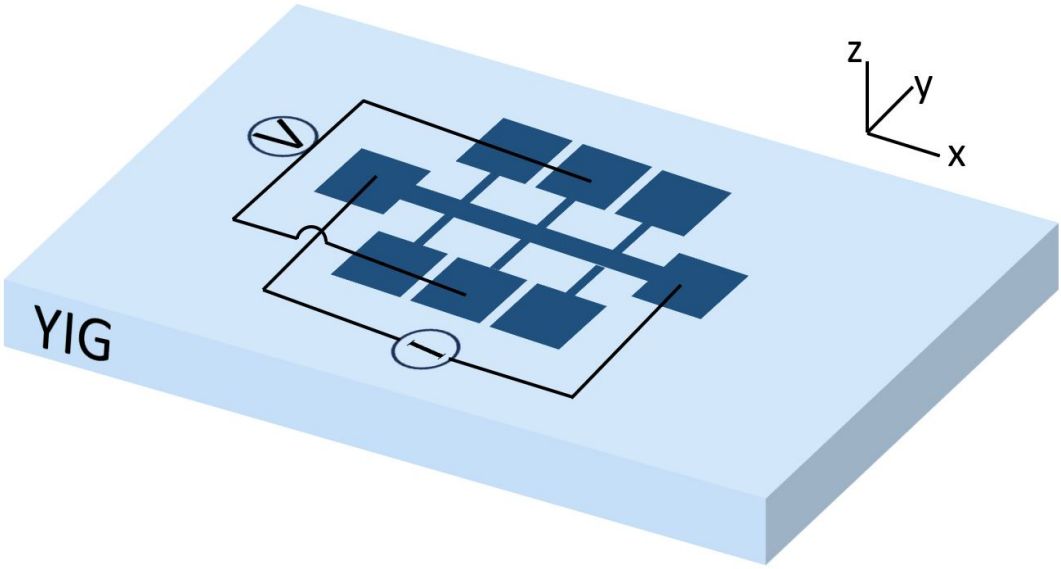

Figure 8.1: Schematic of the Hall bar device patterned on our bulk polycrystalline YIG substrates. The applied DC current, I, generated a thermal gradient via Joule heating. Using current reversal techniques, the longitudinal spin Seebeck voltage can be acquired from transverse voltage measurements. Resistivity measurements were also performed when measuring the longitudinal voltage

Samples were mounted to a temperature-regulated oxygen-free highly conductive (OFHC) copper block in a sample-in-vacuum cryostat. Environmental temperature was regulated and monitored with a LakeShore 331 Temperature Controller. Calibration on the local heating on the Hall bar allowed an estimation of the temperature and thermal gradient of the sample. A Keithley 6221 sourcemeter drove a DC current along the $\hat{\mathbf{x}}$-direction resulting in an established thermal gradient, in the $\hat{\mathbf{z}}$-direction, between the thin films and the YIG substrate via Joule heating. A Keithley 2182 A nanovoltemeter detected the resulting transverse voltage, in the $\hat{\mathbf{y}}$-direction. An externally applied magnetic field was used to align the magnetization of the YIG substrate in the plane of the film. The field was subsequently swept from 1500 Oe to -1500 Oe and back again to 1500 Oe. According to theory for this type of LSSE measurement [33,214,262], we can estimate the longitudinal spin Seebeck voltage

from transverse voltage measurements through the following equation:

$$V_{LSSE} = \frac{V_t(+I) + V_t(-I)}{2}, \tag{8.1}$$

where $V_t(+I)$, and $V_t(-I)$ are the measured transverse voltages using a positive and negative DC current, respectfully.

To make comparisons to the Cr thin films, we grew a 25 nm Pt and 25 nm Cu thin film. We expect, from theory[2], the Pt film to have opposite sign to that of Cr and Cu to not result in an LSSE voltage. The Pt film was sputtered after reaching a base pressure of 8×10^{-8} Torr at a rate of $0.1 - 0.125$ nm/s at a DC sputtering power of 100 W. The Cu sample was thermally-evaporated in high vacuum($\approx 10^{-7}$ Torr) at a rate of 1 nm/s. Both samples were shaped into a Hall bar geometry through the same potolithographic and chemical procedures and deposited onto bulk polycrystalline YIG substrate from the same batch.

8.3. RESULTS AND DISCUSSION

The Hall bars used in this experiment were calibrated in a temperature-regulated vacuum cryostat. Temperature outside the OFHC copper block was monitored and regulated with a LakeShore 331 Temperature Controller for a reference background temperature. Two Hall bars were used in the calibration process; one Hall bar had voltage connections to a Keithley 2182 A nanovoltemeter and current connections to a Keithely 2400 sourcemeter and another Hall bar had voltage and current connections to a Stanford Research System 4-wire AC resistance bridge.

The Hall bar connected to the Stanford Research System would monitor the resistance using a small current in the μA range to precisely, with minimal amount of heating, determine the resistance in accordance with the background temperature.

This provides a reference between the resistance of the metal thin film and the surrounding temperature. The Hall bar connected to the Kiethleys would supply a range of powers and measure the corresponding resistance after waiting a sufficient amount of time for thermal equilibrium. From this we can determine the change in resistance with applied power at every temperature giving us curves of resistance values using a large applied power (Heated) and one with a low applied power (non-heated) as seen in Figures 8.2 and 8.3.

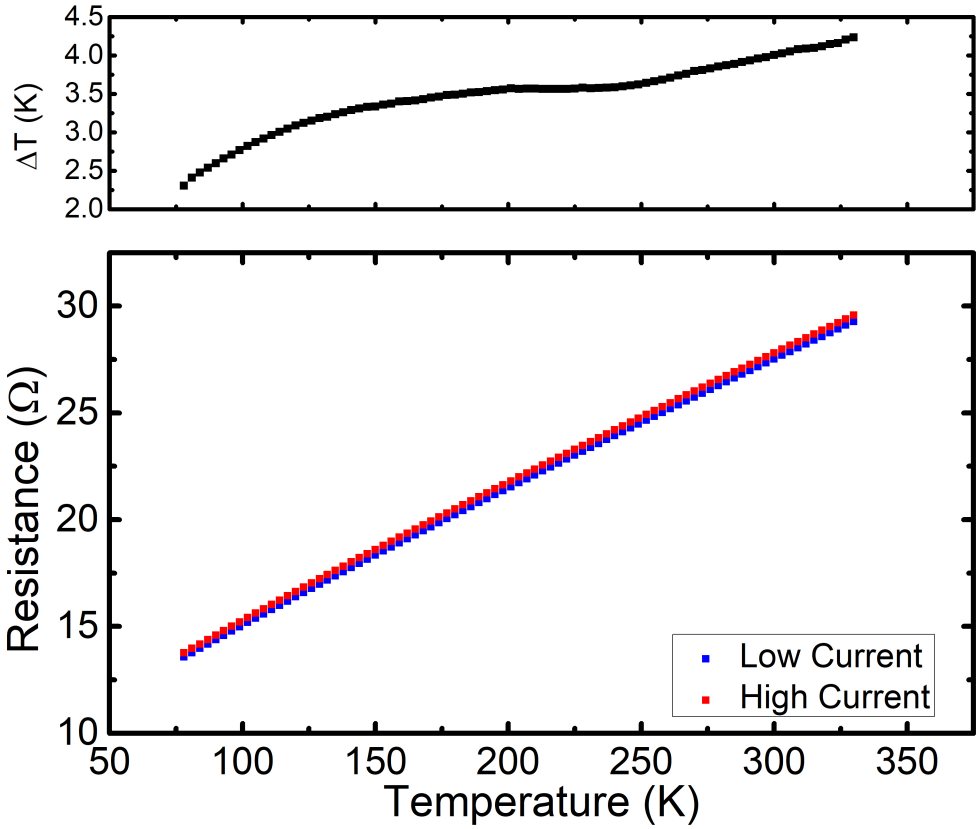

Figure 8.2: The resistance versus temperature curves for a low current, blue symbols, and high current, red symbols, of a 25 nm Pt Hall bar. The inset is the estimated temperature difference versus temperature.

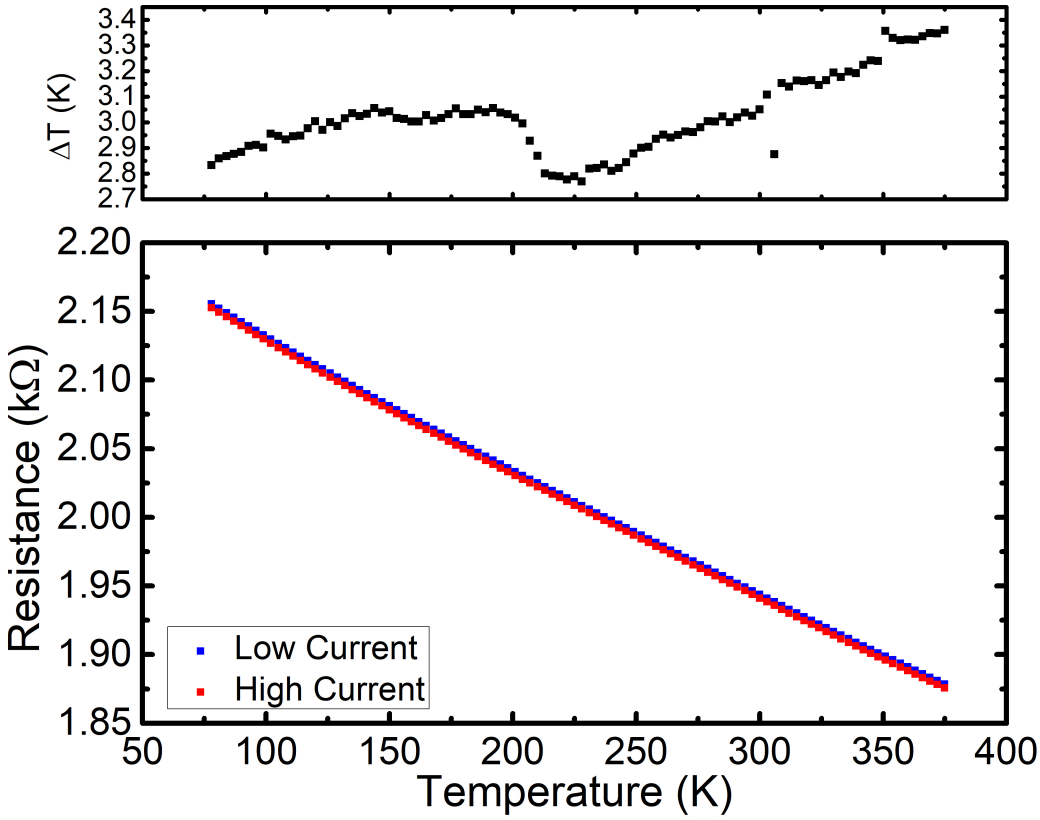

Figure 8.3: The resistance versus temperature curves for a low current, blue symbols, and high current, red symbols, of a 10 nm Cr hall bar. The inset is the estimated temperature difference versus temperature.

Figure 8.2 represents the resistance vs temperature curves for a low power (blue symbols) and a high power (red symbols) for the 25 nm Pt/YIG sample. The above graph is the estimated temperature difference, ΔT vs temperature. The ΔT's are estimated from the change in resistance of the sample for some heating power. We use these determined temperature differences to make accurate and reasonable comparisons between samples.

Figure 8.4 is the raw LSSE voltage, as calculated from equation 1, versus applied in-plane magnetic field for a 10 nm evaporated Cr sample (blue), a 25 nm sputtered Pt sample (green), and a evaporated 25 nm Cu sample (red) at 78 K. As

one would expect, the Cr thin film has opposite sign to that of Pt[61,189] and that Cu gives no measurable signal[261].

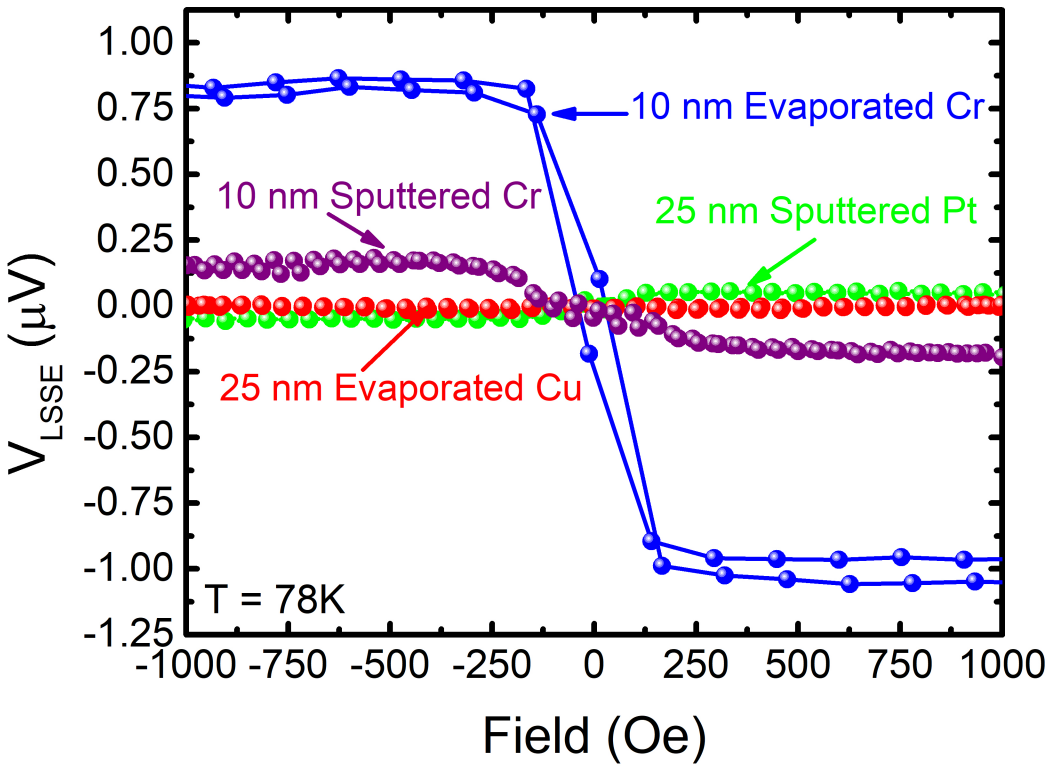

Figure 8.4: The raw thermal voltage as calculated from Equation 1 vs an in-plane external magnetic field for a 10 nm thermally-evaporated Cr sample (blue symbols), a 10 nm sputtered Cr sample (purple symbols), a 25 nm sputtered Pt sample (green symbols), and a 25 nm thermally-evaporated Cu samples (red symbols). Data had been vertically shifted to center to 0 V. All data was taken at 78 K

From Figure 8.4, the 10 nm evaporated Cr thin film produces a much larger raw spin Seebeck voltage as compared to the other samples. Since the 25 nm sputtered Pt is more than twice as thick than both Cr samples, it makes intuitive sense that it should have a much lower spin Seebeck voltage considering that inverse spin Hall voltages tend to decrease exponentially with the thickness of the film. The evaporated Cu film shows no indication of spin Seebeck voltage, which is in line with

the previous observations that Cu tends to have a rather small or zero spin Hall angle.

Figure 8.5 compares the LSSE voltage divided by length, resistivity, and thermal gradient vs applied field for the 10 nm Cr sample (blue) and the 25 nm Pt sample (green) at selected temperatures between 78 K and 303 K.

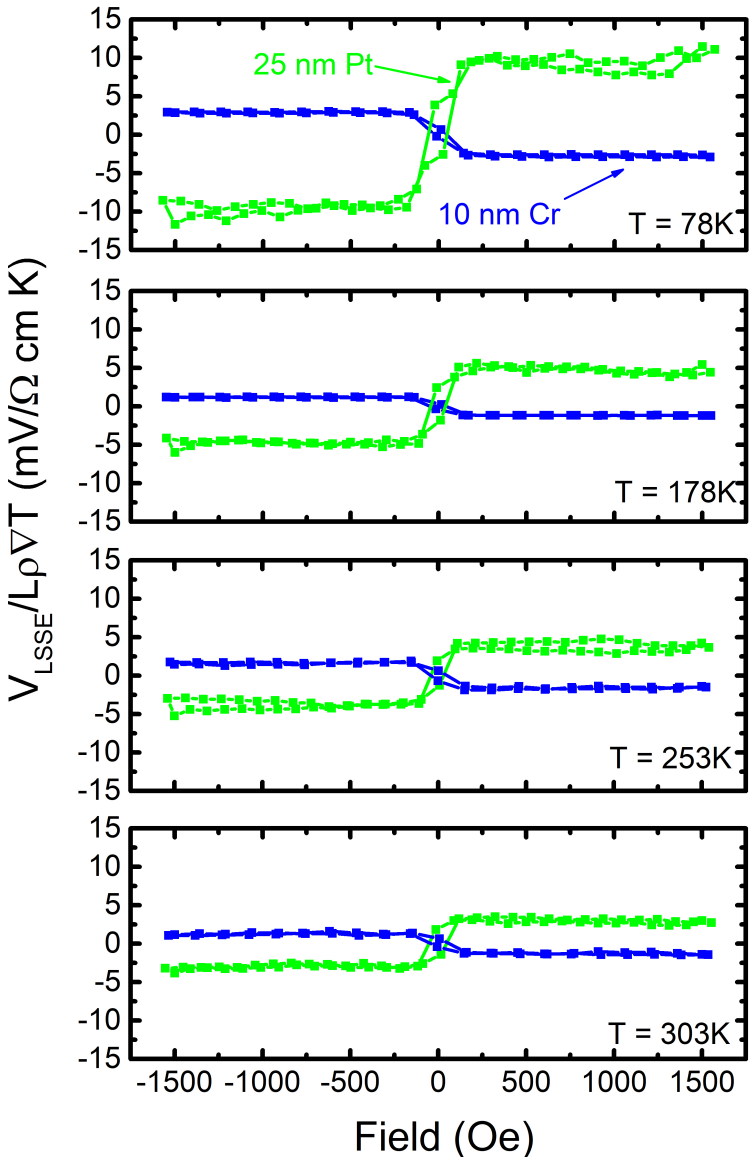

Figure 8.5: LSSE voltage, V_{LSSE}, normalized by length, L, resistivity, ρ, and thermal gradient, ∇T, versus applied magnetic field for Cr(10)/YIG (blue) and Pt(25)/YIG (green) at selected temperatures between 78 K and 303 K with same scaled vertical axes.

When appropriately scaling the spin Seebeck voltage, we can see that over this temperature range, the 25 nm sputtered Pt film showcases a larger spin Seebeck voltage than the evaporated 10 nm evaporated Cr thin film; despite the fact that the sputtered Pt film is in a non-optimized thickness[173]. Over this temperature range

we can also note the comparable voltages the evaporated Cr film has with respect to the sputtered Pt film. At 78 K, the evaporated Cr film spin Seebeck voltage difference of 5 μV and the sputtered Pt film is 17.5 μV, which is a 28.5% difference between the two samples. As we increase the temperature to 303 K, the evaporated Cr film is approximately 2.5 μV and the sputtered Pt film is 5 μV, which is now a 50% difference between the two samples. This shows that the evaporated Cr thin film has comparable voltages to that of a sputtered Pt film over a wide temperature range.

Thermally generated spin voltage, with the assumption of spin-charge conversion occurring in the bulk of the film via the spin Hall effect, is typically described by

$$V_{LSSE} = 2\left(CL\nabla T\right)\left(\rho\theta_{sh}\right)\frac{\lambda_{sf}}{t}\tanh\left(\frac{t}{2\lambda_{sf}}\right), \tag{8.2}$$

where V_{LSSE} is the longitudinal spin Seebeck (LSSE) voltage, L is the length of the sample, ∇T is the applied thermal gradient, ρ is the charge resistivity, θ_{sh} is the spin Hall angle, λ_{sf} is the spin diffusion length in the metal film, t is the film thickness, and C is a constant related to the efficiency of spin injection from the YIG to the metal film[189,190,191]. We can rewrite this equation to obtain, on the left hand side, $V_{LSSE}/L\nabla T\rho$, which is proportional to spin-charge conversion efficiency. This provides a way, based on measurable parameters in our experiment, to estimate the spin-charge conversion efficiency and make meaningful comparisons between samples. Although not explicitly written in equation 2, the spin Hall angle and spin diffusion length can be temperature dependent[110,242].

Figure 8.6 compares the absolute value of the spin-charge conversion efficiency $\mid V_{LSSE} \mid /L\rho\nabla T$ vs temperature for a 10 nm thick thermally-evaporated Cr (blue symbols), a 10 nm thick sputtered Cr film (purple symbols), and 25 nm sputtered Pt films (green symbols). ∇T is defined as $\nabla T = \Delta T/L_z$, where ΔT is the temperature difference between the metal film and YIG substrate and L_z

is the thickness of the YIG substrate. The assumption being that YIG is the largest thermal sink in the system. Although some discrepancies have been reported[228,230,231]; we assume the local heating method establishes a relatively uniform thermal gradient in our thin films and that the YIG substrate is our largest heat sink.

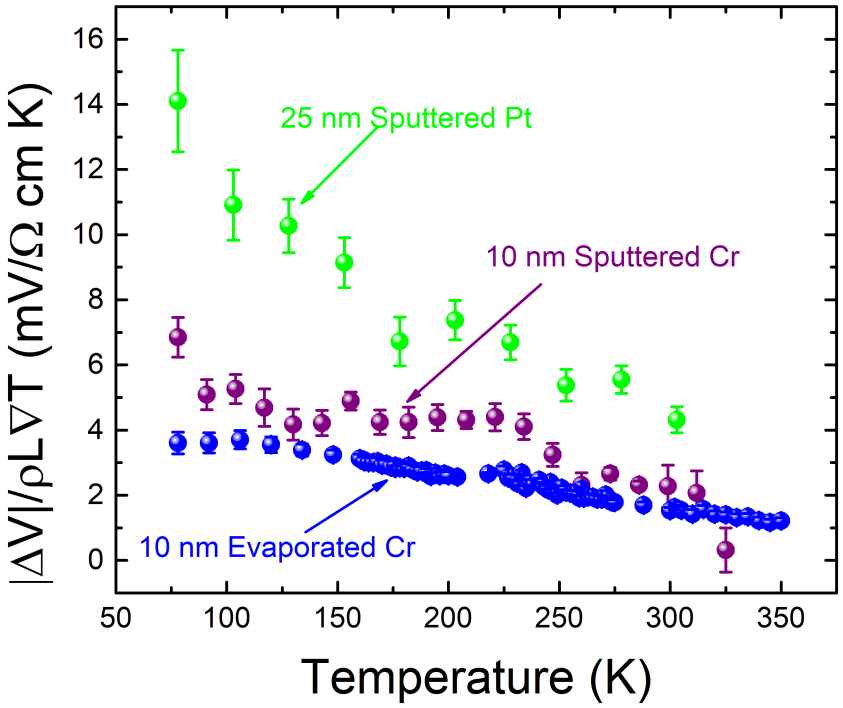

Figure 8.6: The absolute value of the longitudinal spin Seebeck voltage, V_{LSSE}, normalized by the length of the Hall bar, L, the resistivity of the metal film, ρ, and the thermal gradient, ∇T versus temperature. The 10 nm thermally-evaporated Cr thin film is represented by blue spheres, the 10 nm sputtered Cr thin film data is in purple, and the 25 nm sputtered Pt film data is in green.

For all measured temperatures, the Pt sample clearly shows a larger efficiency in comparison to the evaporated Cr sample. Both samples show a larger spin-to-charge efficiency at lower temperatures. Interestingly the evaporated Cr film shows a distinct peak near 100 K. The dependence with temperature and location of a peak is

similar to that seen in the spin conductivity of bulk polycrystalline YIG [88] and could suggest the unusual peak seen in the evaporated Cr data; however, this peak should also be present in the sputtered Pt sample since they were deposited on comparable YIG substrates. It could be, for the case of Pt, the different interface quality with YIG and thickness of the film will either obscure the small peak or suppress it. The sputtered Cr thin film shows a clearly larger efficiency than the evaporated Cr. This could be due to the overall cleanness of the sputtered Cr film which has a much lower resistivity than the evaporated Cr film. The spin-to-charge efficiency of the sputtered Pt film is not as high as one would expect, but the sputtered Pt film is 25 nm thick makes it weaker for spin-to-charge conversion as opposed to a 10 nm film [207].

Figure 8.7**a)** compares the dimensionless sensitivity defined as $dR/dT * (T/R)$ versus temperature for our thermally-evaporated Cr thin film (blue line) and sputtered Cr thin film (green line). Figure 8.7**b)** compares the ratio of the V_{LSSE} over the product of resistance and temperature difference versus temperature for our 10 nm evaporated Cr (blue symbols), our sputtered 10 nm Cr sample (green symbols), and literature data [189] of a sputtered 10 nm Cr (red symbols) sample.

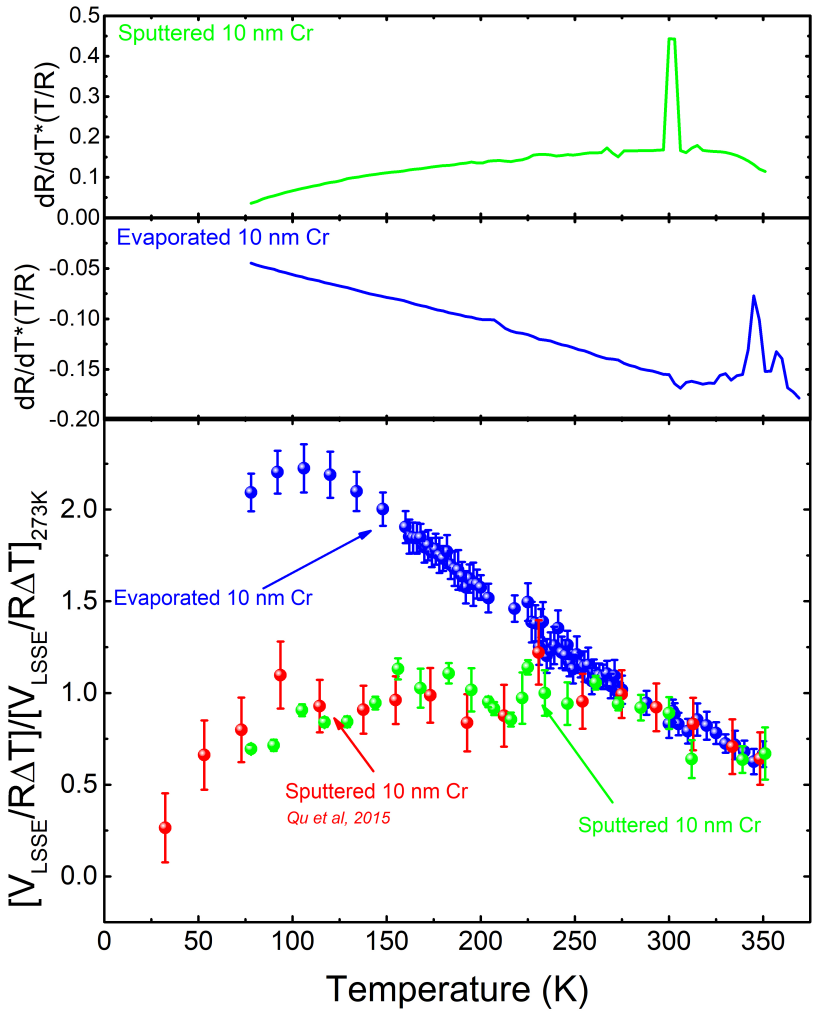

Figure 8.7: **a)** The dimensionless sensitivity $(dR/dT*(T/R))$ for the 10 nm thermally-evaporated Cr thin film vs temperature. Two distinct peaks are visible with their centers at ≈350 K and ≈200 K. **b)** A comparison of the temperature dependence of the longitudinal spin Seebeck voltage divided by film resistance and temperature difference $(V_{LSSE}/R\Delta T)$ between a 10 nm sputtered Cr thin film[189] (navy blue symbols) and a 10 nm thermally-evaporated Cr thin film (blue symbols). The $(V_{LSSE}/R\Delta T)$ values at 273 K are used as reference data.

Our 10 nm sputtered Cr sample shows excellent agreement with literature data over the measured temperature range. The two sputtered Cr samples compared to the thermally-evaporated one show excellent agreement at temperatures above 200 K;

however, below this temperature there is a significant divergence. The evaporated Cr sample increases monotonically with decreasing temperature until it reaches a peak near 100 K, whereas the sputtered Cr samples stays relatively constant until rapidly decreasing below 100 K. To further investigate our evaporated Cr thin film, Figure 8.7**a)** shows dimensionless sensitivity vs temperature for our 10 nm evaporated Cr thin film (blue symbols) and 10 nm sputtered Cr film (green symbols). Two distinct peaks appear near 350 K and 200 K. These two peaks likely indicate the separate Néel temperatures of the incommensurate and commensurate spin density wave antiferromagnetic states, coexisting in a strain-driven mixed state in the evaporated film. Thin film Cr samples[45,146,160] commonly show Néel temperatures that deviate from the bulk value. Mixed spin density wave states can exist in Cr thin film samples that have a high level of disorder, measured as having large resistivity and strain[30]. This could explain the notably higher signal below 200 K in our "dirty" evaporated Cr sample as compared to a more "clean" sputtered Cr film. Our sputtered 10 nm Cr film shows one distinct peak near 300 K, which could correspond to the typical bulk Néel temperature of Cr.

The evaporated Cr thin film has three distinct magnetic states: above 350 K the film is fully paramagnetic, between 200 K and 350 K the commensurate spin density waves are antiferromagnetic and the incommensurate spin density waves are paramagnetic, and below 200 K both spin density waves are antiferromagnetic. This is much different from the sputtered Cr film, where it is paramagnetic above 300 K and antiferromagnetic below.

From our experiments, we see large changes in the longitudinal spin Seebeck voltage in our evaporated Cr thin film as compared to sputtered thin films. These changes can be due to either a modification of the coupling at the Cr/YIG interface, a change in the spin conversion, a change in the spin diffusion length, or a combination of the three. The modification of these parameters could be due in part to modifications of the nature of the spin density wave due to strain-related effects in

evaporated Cr that can, in general, be different from sputtered films[1,30,132,245]. From our results, it is difficult to pin down exactly what parameter is most responsible for these modifications found in thermally-evaporated Cr.

8.4. CONCLUSION

In summary, we presented evidence of large spin-charge conversion in thermally-evaporated Cr thin films on polycrystalline YIG substrates using the longitudinal spin Seebeck effect. The enhanced thermal voltages, as compared to sputtered Cr, below 200 K, marked by a peak in the $dR/dT * (T/R)$ vs temperature curve, is indicative of a phase transition of the spin density wave in evaporated Cr. Literature suggest that thermally-evaporated Cr, with large resistivity as compared to sputtered Cr, has a mixed spin density wave state due to strain-induced effects with temperature that modify the spin-charge conversion process. This allows the evaporated Cr to have large spin Seebeck voltages and, when scaled appropriately, comparable thermal voltages to sputtered Pt. This suggests that thermally-evaporated Cr can be a useful spin detector over a wide range of temperatures for spintronics and spincaloritronic measurements and applications.

CHAPTER 9: SPIN HALL MAGNETORESISTANCE IN THERMALLY-EVAPORATED AND SPUTTERED CR THIN FILMS ON POLYCRYSTALLINE YIG SUBSTRATES

With the current reversal technique on our Hall bar structures we can estimate thermal effects that scale with even powers of current, but we can also estimate magneoresistive or electrical contributions to the signal that scale with odd powers of current as well. In this chapter we explore and analyze the magnetoresistive response on the evaporated and sputtered chromium thin films.

9.1. INTRODUCTION

Magnetoresistance (MR) is a critical element in contemporary technologies, spanning applications from magnetic sensors[279] to magnetic random access memory (MRAM) devices[7]. The advancement of the next generation of spintronic devices for these technologies necessitates a depper comprehension of more recent MR phenomena, notably spin Hall magnetoresistance (SMR) and Rashba-Edelstein magnetroresistane (REMR). In recent years, experimental investigations have predominately centered around heavy metal (HM)/ferromagnetic insulator (FMI) heterostructures such as: $Pt/Y_3Fe_5O_{12}$ (YIG)[166,262], Ta/YIG[90,280], W/YIG[191], and Pt/Fe_3O_4[58]. The remakrable progress observed in these heterostructures can be attributed to the substantial spin-orbit-coupling (SOC) exhibited by these HMs, leading to heightened spin-to-charge conversion efficiencies via the spin Hall (SHE) and inverse spin Hall (ISHE) effect[97,118,224].

The interplay between SHE and ISHE at the interface of HM/FMI heterostructures facilitates the interaction between spin currents and magnetization through spin-transfer torques (SOTs) or spin-orbit torques (SOTs). Consequently, this interaction modifies the resistance of the metal, contingent on the alignment of the magnetization with respect to the spin polarization. This leads to the reflection and absorption of spin currents at the HM interface, resulting in simultaneous SHE and ISHE, a phenomenon known as spin Hall magnetoresistance (SMR)[11,73,211].

In the pursuit of more-cost-effective spintronic devices, there has been a shift in focus from heavy noble metals to much lighter 3d transition metals. Chromium (Cr), in particular, has garnered attention due to recent reports of substantial spin-to-charge conversion[26,35,61,189]. Similar effects to SMR are observed in these lighter 3d transition metals, where a Rashba interface is formed. At this interface, the spin-orbit coupling (SOC) of the metal in contact with an FMI can be altered, detected through processes analogous to SHE/ISHE coupling, specifically the Rashba-Edelstein effect (REE) and inverse Rashba-Edelstein effect (IREE)[42,149,179].

Chromium, identified as a collinear antiferromagnet wit ha bulk Néel temperature of 311 K[70], presents a promising prospect for cost-effective spintronic devices. The antiferromagnetic property of Cr is characterized by spin density waves (SDWs), as opposed to traditional antiferromagnets characterized by antiparallel localized magnetic moments[70,72]. These SDWs are fluctuations of spin density with respect to lattice spacing of itinerant electrons[27,30,70,136] that host a variety of modes: incommensurate spin density waves (ISDWs) that are incommensurate with the lattice spacing, commensurate spin density waves (CSDWs) that are commensurate with lattice spacing, and a mixed state where both ISDW and CSDW are observed[70]. Some investigators claim the notably high spin-to-charge conversion in Cr is not strictly dependent on its antiferromagnetic order, instead originates from an effective SOC[42,189].

In our previous work, 10 nm thick Cr Hall bars were deposited by both thermal evaporation and DC magnetron sputtering on a bulk polycrystalline yttrium-iron-garnet (YIG). We showed a large spin-to-charge conversion efficiency via the longitudinal spin Seebeck effect. On the sample samples, we measured both the transverse and longitudinal magnetoresistance. In this report, we will explore the effets of different growth methods and oxidation of Cr has on the magnetoresistance. Furthermore, investigations into the interfacial interactions between the bulk polycrystalline YIG substrate and the sputtered Cr thin film are also reported. To study the effects of oxidation, we cap our sputtered Cr thin film with a thin layer of aluminum (Al) and allow that Al layer to oxidize at ambient conditions. We assume the natural oxidation of the thin Al cap prevents excessive oxidation of the Cr underneath leading to a more pure Cr thin film[102]. Lastly, we insert a thin Al layer between the Cr and YIG substrate and note an abrupt change in magnetoresistance behavior when the interfacial symmetries are broken.

In this letter, we observe the oxidation of sputtered Cr has a distinctive asymmetric and unidirectional behavior in the MR curves, in contrast to the oxidized thermally evaporated Cr/YIG bilayer that has a more symmetric behavior. When the sputtered Cr sample is capped with a thin Al layer, the asymmetry in the saturating resistance values of the MR curves ceases to exist, while the zero field transition persists implying an induced magnetic proximity effect (MPE) or reconfiguration of the ferromagnetic domains of the YIG substrate. As evidence for this claim, another sputtered Cr sample was created with an Al insertion layer breaking magnetic interactions between the Cr and YIG. The MR behavior of this samples reveals a more AMR-like behavior, implying that a magnetic phase in our oxidized Cr. We postulate the numerous FM/AFM phases of Cr, due to oxidation, could participate in canting of the AFM moments and lead to a combined anomalous Hall (AHE) like and MPE-induced AMR contribution to the MR of the sputtered Cr.

9.2. EXPERIMENTAL DETAILS

Bulk polycrystalline yttrium-iron-garnet (YIG) were chemically cleaned, spin coated with a negative resist (APOL-LO3202), and baked at 100° C for 1 minute. A mask of pre-patterned Hall bars was aligned to the substrate under an optical microscopy. The substrates are exposed to ultraviolet light for approximately 20 seconds, baked again at 100° C for 1 minute, and developed using AD-10. The 10 nm of thermally evaporated Cr is deposited from a chrome platted Cr tungsten rod source in high vacuum ($\approx 10^{-7}$ Torr) at room temperature at a rate of ≈ 0.3 nm/s with nominal thickness determined by a calibrated piezoelectric quartz crystal monitor. The 10 nm DC sputtered Cr is deposited from a Cr sputtering target near room temperature in ultra high vacuum ($\approx 10^{-8}$ Torr) at a rate of 0.03 nm/s in a 5 mTorr Ar atmosphere with a nominal thickness determined by the same fashion. Both samples undergo a similar liftoff procedure of an acetone bath followed by a N2 drying.

The deposited Hall bars have dimensions of $1000 \times 100\,\mu\text{m}^2$ for the current channel and $150 \times 50\,\mu\text{m}^2$ adjacent legs for the voltage taps. We note that both Cr samples are allowed to naturally oxidize and to understand the effects of oxidation on the magnetoresistance, we create similar devices that are either capped with 4 nm of aluminum (Al) or have an interlayer of 4 nm of Al for the sputtered Cr sample. Both reference the Al/Cr/YIG and Cr/Al/YIG samples have the Al layers grown by DC sputtering. The capped Al sample is allowed to naturally oxidize that we refer to as AlO_x/Cr/YIG. The interlayer Al sample, Cr/Al/YIG, is used to understand the interfacial effects between the sputtered Cr thin film and bulk polycrystalline YIG by breaking any interfacial magnetic interaction and symmetries between Cr and YIG.

All samples are mounted to a oxygen-free highly conductive (OFHC) copper block inside a vacuum cryostat. Samples are ultrasonically wire bonded to current and voltage taps as shown in Figure 9.1.

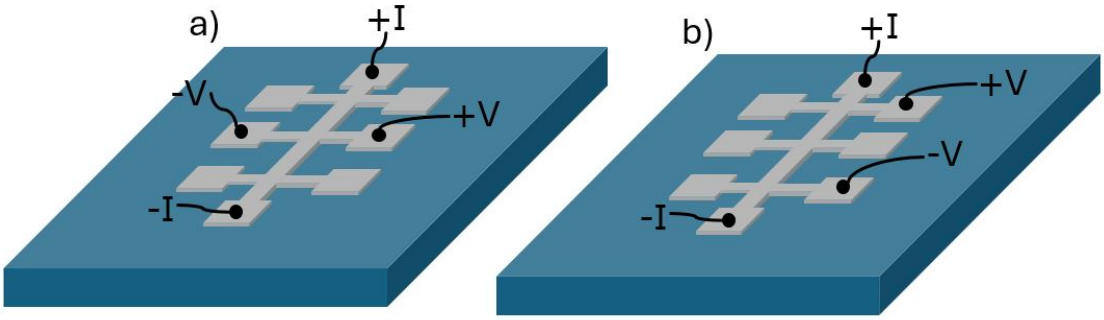

Figure 9.1: Schematic diagrams of the Hall bar structures configured with a) transverse voltage taps and b) longitudinal voltage taps.

Temperature is regulated and monitored by a Lakeshore 331 temperature controller, a DC current is provided by a Keithley 6221 DC/AC current source meter, and voltage is picked up by a Keithley 2182a nanovoltmeter. From our previous work, we utilize the current reversal technique[33,214,262] given by the following equation:

$$V_{MR} = \frac{V(+I) - V(-I)}{2}, \tag{9.1}$$

where V_{MR} are electrical components that scale in odd powers of current such as magnetoresistance, $V(+I)$ is the measured voltage for a positive current, and $V(-I)$ is the measured voltage for a negative current. Both longitudinal and transverse resistances are determined by Ohm's law.

9.3. RESULTS AND DISCUSSION

Figure 9.2 we have the non-thermal resistance defined as $V_{non-thermal}/I$, where $V_{non-thermal}$ is the non-thermal voltage estimated from the current reversal technique and I is the applied current, for the 10 nm thermally-evaporated Cr thin film (blue) and the 10 nm sputtered Cr thin film (purple) at 78 K and 273 K.

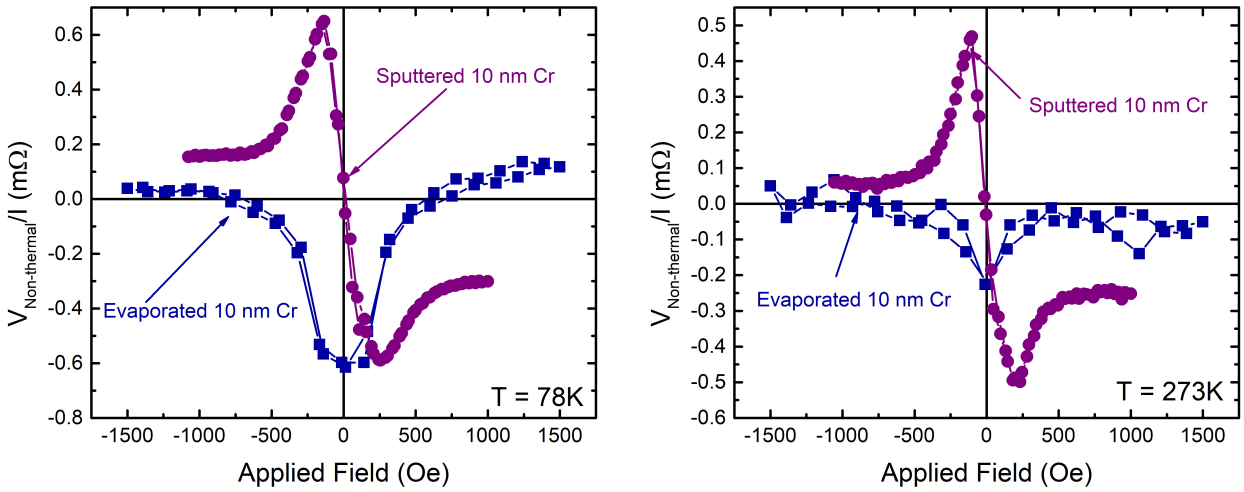

Figure 9.2: The non-thermal resistance, $V_{non-thermal}/I$, where $V_{non-thermal}$ is the non-thermal voltage detected from the current reversal technique and I is the applied current. Displayed are the non-thermal resistances of the thermally-evaporated Cr thin film (blue) and the sputtered Cr thin film (purple) at a) 78 K and b) 273 K.

Immediately one can see the vastly different resistance behavior as a function of applied magnetic field for the two Cr samples. The thermally-evaporated Cr sample shows a much more symmetric appearance with applied field that decreases with increasing temperatures. This magnetoresistance response is akin to other experimentally observed spin Hall magnetoresistance[256]. There are possible contributions of anisotropic magnetoresistance (AMR) that are commonly observed in these types of experiments since both AMR and SMR share common symmetries[44,49,289]. The sputtered Cr sample, however, displays a much more asymmetric behavior as a function of applied magnetic field. Besides the possible AMR and SMR contributions to the signal, there is an obvious dominant asymmetry component that exists not only at low temperatures, but also near the Néel temperature of the sample. This strong asymmetry could be a result of anomalous Hall effect-like (AHE) contributions caused by magnetic interactions with the YIG substrate. This asymmetric behavior could

have resulted from interfacial effects with the YIG substrate that caused uncompensated moments with possible canting of magnetic moments to be out-of-plane of the film[68,217] that may have lead to contributions of AHE-like features[217] to the signal.

In Figure 9.3 we have displayed three samples: a) the bare sputtered Cr on YIG, b) an AlO_x/Cr/YIG sample, and c) Cr/Al/YIG sample. The Al capping and insertion layer samples were created to explore the interfacial and oxidation effects of Cr has on its magnetoresistance.

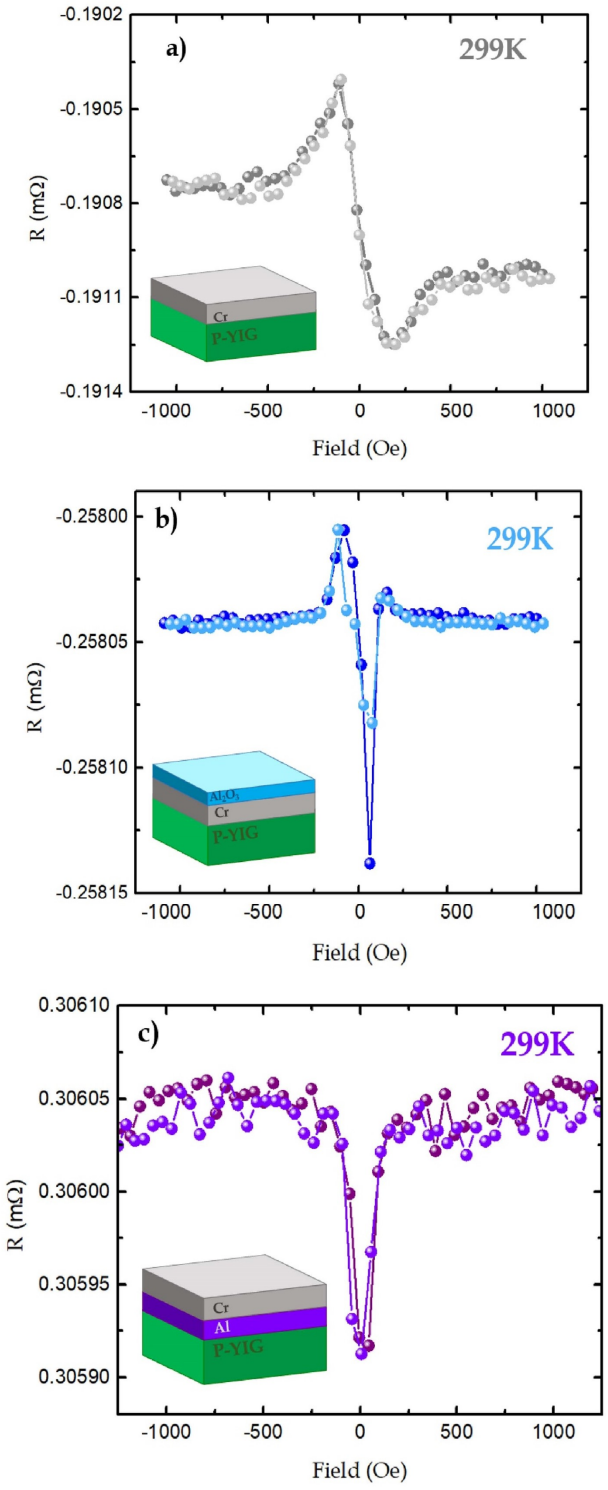

Figure 9.3: The transverse magnetoresistance versus applied magnetic field at 299K for a) sputtered Cr/YIG, b) AlO_x/Cr/YIG and c) Cr/Al/YIG.

We can see that the capping layer of Al has a drastic effect on the asymmetry of the signal. The saturating resistance values are now equal value at either saturating field value; however, the Al capped sample still displays some asymmetry near zero field with a sharp dip and rise. Aluminum is a nonmagnetic metal that easily oxidizes and is used to protect the Cr layer underneath from oxidation. The Cr layer is still in full contact with the YIG substrate and some of the asymmetry remains; therefore, it is not necessarily just interfacial effects causing the AHE-like component, but possible Cr oxidation states. Chromium does not oxidize in a manner akin to typical metals[54], instead there can exist regions in the film that are metallic and other parts that have oxidized. Of the possible oxidation states, one in particular is ferromagnetic, CrO_2[134,232]. We speculate that the asymmetry found in the sputtered Cr/YIG sample is partly due to interfacial effects with the YIG substrate, but also with the complex oxidation in the sputtered Cr that leads to a complex magnetic landscape. It is only when the Al is inserted between the sputtered Cr and YIG substrate that the asymmetry is completely eliminated. The sputtered Cr will oxidize in the Cr/Al/YIG sample, but since it is not in direct contact with the YIG, we do not observe any asymmetry caused by either magnetic proximity effects at the interface with the oxidized Cr nor AHE-like effects.

9.4. CONCLUSION

In summary, based on growth methodology and interface quality, chromium can exhibit either a symmetric magnetoresistance response characterized by a combination of anisotropic magnetoresistance and spin Hall magnetoresistance or a asymmetric magntoresistance response with dominant anomalous Hall-like that possibly stem from interactions at the interface with a yttrium-iron-garnet substrate and oxidation effects. Upon inserting an aluminum layer between the sputtered chromium and ferromagnetic substrate, the magnetoresistance exhibited a symmetric response, whereas the aluminum capping showed a small asymmetric component a low fields,

and is it is based on these observations that we conclude that possible oxidation states in the chromium thin film and interface quality with the substrate lead to anomalous Hall-like and magnetic proximity effects that gave rise to asymmetric field behaviors.

CHAPTER 10: SPIN TRANSPORT MEASUREMENTS IN MAGNETICALLY COUPLED LSFO/LSMO/STO AND LSFO/LSMO/LSAT HETEROSTRUCTURES

In this chapter, we report measurements on a $La_{1-x}Sr_xFeO_3$(LSFO)/$La_{1-x}Sr_xMnO_3$(LSMO)/$(LaAl_3)_{0.3}\,(Sr_2TaAlO_6)_{0.7}$(LSAT) perovskite heterostructure with patterned Hall bars and 8-terminal devices fabricated via e-beam lithography. Collaborators performed atomic force microscopy (AFM), x-ray reflectivity (XRR), and x-ray diffraction (XRD) to characterize the perovskite heterostructure. Our devices aimed to probe the spin transport in this spin-flopped coupled perovskite heterostructure via longitudinal spin Seebeck effect (LSSE) and spin-orbit torques (SOT) via current pulses. Due to uncontrolled pinholes permeating the surface of the LSFO layer that is electrically shorted with the LSMO underneath, the transport measurements had uncontrolled current path ways making it difficult to realize any spin transport phenomena. Despite this pinhole problem, magnetoresistance was still captured using the Hall bar devices.

10.1. INTRODUCTION

Perovskites of the ABO_3 structure, where A is a alkaline-earth metal, B is a 3d transition metal, and O is oxygen. In this system, the A sites are divalent or trivalent metals, for example Sr or La atoms. The B sites are tetravalent or trivalent atoms, such as Co or Fe atoms. Usually, the B cations generally determine the physical properties by either the localized or collective behavior of the d electrons[114]. The valency of the B sites depends on the valency of the A cations and thus lead to unusual electronic and magnetic properties such as colossal magnetoresistance[69,193,196],

ferroelectricity[51], and superconductivity[20,153], which make them attractive for spintronic devices[168,197].

If one has lanthanum (La) and strontium (Sr) on the 'A' sites, and the 'B' sites occupied by manganese (Mn) atoms, then one obtains a perovskite of the name lanthanum strontium manganite ($La_{1-x}A_xMnO_3$, LSMO). Instead, if one substitutes the manganese atom for an iron atom (Fe), then one obtains the perovskite of the name lanthanum strontium ferrite ($La_{1-x}A_xFeO_3$, LSFO). These perovskite structures are often characterized with high degree of carrier spin-polarization and colossal magnetoresistivity that have an interesting potential for spintronic applications[34,120,154].

The lattice structure of these perovskites is approximately a face-centered-cubic (fcc) with a Mn ion at the center and La/Sr cations at the corners of the cubic unit cell. Six oxygen ions surround the Mn ion and together they form a MnO6 octahedron (or a FeO6 for LSFO). This is illustrated in Figure 10.1. Depending on the amount of A doping, the lattice becomes distorted due to the mismatch between the radii of the cations and the Mn-O-Mn (Fe-O-Fe) bond angle changes giving a rhombohedral crystal structure[154]. These perovskites can be tailored into a rich range of electronic and magnetic phases depending on the concentration of A doping (in this particular case with LSMO and LSFO, it is the concentration of Sr). For LSMO with a Sr concentration between 0.2 to 0.5, it exhibits ferromagnetic and metallic properties[139]. As for LSFO, an antiferromagnetic insulating phase can be achieved with an optimal doping of Sr of $x \leq 0.4$[276].

The ferromagnetism in LSMO is mediated through the double exchange mechanism between the Mn^{+3} and Mn^{4+} ions through an oxygen atom[284]. Likewise, in LSFO the antiferromagnetism originates from an exchange interaction between Fe^{3+} and Fe^{4+} ions through an oxygen atom. Forming heterostructures from these perovskite materials leads to an interesting coupling through a spin-flop exchange interaction between the antiferromagnetic LSFO layer and ferromagnetic LSMO layer. For idealized planar interfaces with uncompensated antiferromagnetic spins, such as

the (111)-plane of a G-type antiferromagnet (LSFO), the magnetic moments of the ferromagnet tend to align with the antiferromagnetic spins at the interface to reduce the exchange energy of the system[115]. Alternatively, interfaces with compensated antiferromagnetic spins experience spin frustration where the moments of the ferromagnetic layer (LSMO) align perpendicular to the antiferromagnetic spin axis in order to minimize energy[116]. This type of coupling is referred to as a spin-flop coupling.

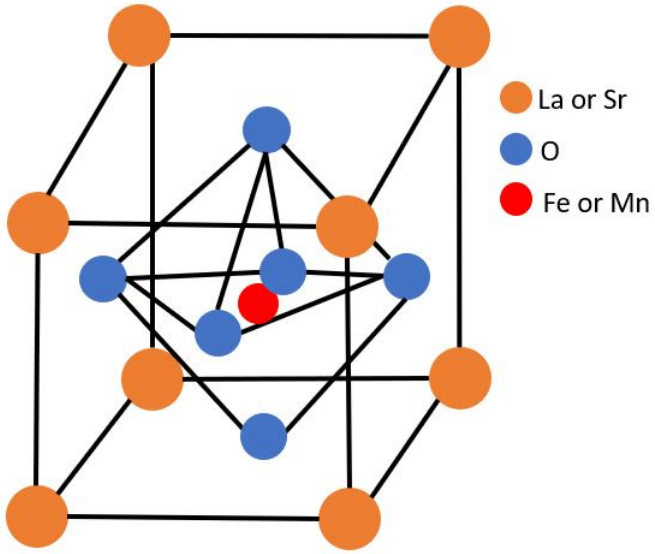

Figure 10.1: The typical perovskite crystal structure. The orange spheres represent either lanthanum or strontium, blue is oxygen, and red is either manganese or iron (manganese for LSMO and iron for LSFO). This illustration is adapted from[154].

Antiferromagnetic/ferromagnetic heterostructures offer unique magnetic interactions such as exchange bias, the shifting of a hysteresis loop[180], and for the case of spin-related phenomena, exchange bias switching driven by spin-orbit torque[187]. LSFO/LSMO bilayers with their spin-flop coupled interaction can serve to host potentially exciting spintronic applications.

$La_{1-x}Sr_xFeO_3$(LSFO)/$La_{1-x}Sr_xMnO_3$(LSMO)/$(LaAl_3)_{0.3}$ $(Sr_2TaAlO_6)_{0.7}$(LSAT) perovskite heterostructure were grown via pulsed laser deposition (PLD). These samples were characterized by atomic force microscopy (AFM), x-ray reflectivity (XRR), and x-ray diffraction (XRD) in order to determine the density of pinholes

on the top LSFO surface, the thickness of the samples, and c-axis of the crystalline structure. Two types of devices were fabricated: Hall bar devices and 8-terminal structures via e-beam lithography. Spin transport measurements were conducted on the Hall bar device via longitudinal spin Seebeck effect (LSSE)[214] and spin-orbit torque (SOT) measurements on the 8-terminal device[63,258]. Magnetoresistance data was taken on the Hall bar devices with and without a main current channel. The 8-terminal device recorded the magnet state with resistance measurements as a large DC current pulse switches the magnetic moment direction in accordance to planar Hall effect (PHE) data. A 8-terminal devices made from 10 nm Pt/ 3 nm Py on a SiO_x substrate was fabricated as a reference sample.

10.2. EXPERIMENTAL DETAILS

Samples of $La_{1-x}Sr_xFeO_3$ (LSFO)/$La_{1-x}Sr_xMnO_3$ (LSMO)/$(LaAl_3)_{0.3}(Sr_2TaAlO_6)_{0.7}$ (LSAT), referred to as the IN series for this study, were grown via pulsed laser deposition (PLD). A more detailed procedure of the growth is given elsewhere[8,239,240]. These samples are doped to a concentration of 50% Sr. At this concentration, the LSFO is nominally in an insulating antiferromagnetic phase[276] and the LSMO is in a conductive ferromagnetic phase[154,215]. Atomic force microscopy(AFM) images were taken, see Figure 10.2, to understand the surface roughness of these samples and the density of pinholes that have the potential to short the two layers together. X-ray reflectivity (XRR) was performed to estimate the thickness of these samples.

The sample was first cleaned with a combination of acetone, isopropyl alcohol, and methanol with a N2 gas drying between each step. Next, the sample was placed on a hot plate for a pre-bake process for 60 seconds at a temperature of 180°C. Afterwards, a thin coat of MMA(8.5)MAA EL6 (Co-PMMA) was spin coated across the entirety of the top surface of the heterostructure. An additional baking process for 60 seconds at 180°C was performed. Another resist layer made from 950 PMMA A6 was spin coated with a final baking step immediately after. The Hall bars

and 8-terminal devices were imprinted into the resist via e-beam lithography. A development step using methylisobutylketone (MIBK) with a 1:3 ratio of isopropyl alcohol with an isopropyl alcohol rinse developed our devices. 10 nm of platinum (Pt) was dc sputtered under an initial vacuum of 8×10^{-8} Torr, and deposited in a 3 mTorr Ar atmosphere at a rate of 0.44 Å/s. A final acetone bath removed all unwanted leftovers and left only the devices on the perovskite heterostructure.

Measurements on the Hall bar devices were performed utilizing a Keithley 6221 DC and AC current source as a means of producing a thermal gradient in the device via Joule heating and measuring the transverse and longitudinal voltages with a Keithley 2182a nanovoltmeter. The DC current pulse experiments used the same Keithley instruments as the Hall bar device to send a small current to probe the resistance, but with the addition of a Tektronix AFG 3022 function generator to send in large DC current pulses. These device structures can be viewed in Figure **??** and Figure 10.3.

10.3. RESULTS AND DISCUSSION

We provide material characterization of our IN042 sample using atomic force microscopy (AFM), x-ray reflectivity (XRR), and x-ray diffraction (XRD). We also provide transport measurements using both a Hall bar design and an 8-terminal device.

10.3.1. SAMPLE CHARACTERIZATION

Here we show growth characteristics and pulse current data of our LSFO/LSMO/LSAT, referred to as IN042. AFM images, shown in Figure 10.2, shows a $5 \times 5\,\mu\text{m}^2$ scan of the surface morphology of our IN042 sample.

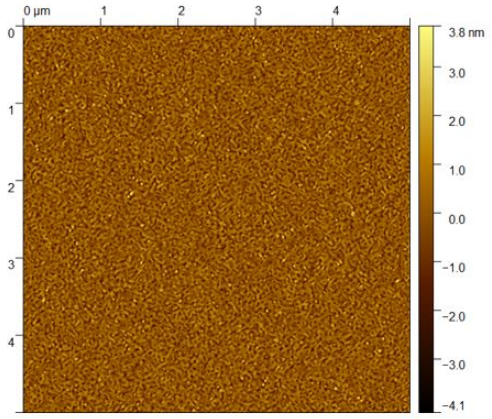

Figure 10.2: A $5 \times 5\,\mu\text{m}^2$ AFM scan of our IN042 sample. Figure was adapted with permission of our collaborators

From the AFM scan, the surface root mean squared roughness was estimated to be 0.7307 nm with a maximum pit depth of 4.109 nm. Note the lack of pinholes that can cause shorting between the LSFO and LSMO layers. The low density of pinholes give the top LSFO layer a clean surface.

The XRR measurements on the IN042 sample estimates a total thickness of 47 nm and a LSFO layer thickness of 11.76 nm. This signifies that it is unlikely that there are pinholes on the LSFO surface that penetrates completely and electrically shorting it to the LSMO layer.

X-ray diffraction (XRD) measurements were taken, not shown here, for measurements of the crystallographic c-axis of the IN042 sample. It was revealed that the c-axis length for two layers to be 3.92Åand 3.88Å, respectfully. These values are consistent with literature[8,47,264]. According to the Goldschmidt tolerance factor, t:

$$t = \frac{r_A + r_O}{\sqrt{2}\,(r_B + r_O)}, \tag{10.1}$$

where r_A, r_B, and r_O are atomic radii of A cation, B cation, and O^{2-} anion, respectively. Values of t, which can be estimated from the ratio of measured c-axis over

a-axis, indicate the crystal symmetry of the perovskite structure[86,144]. According to this factor, our IN042 perovskite is cubic.

10.3.2. TRANSPORT MEASUREMENTS

The 8-terminal device, illustrated in Figure 10.3, is a structure to pulse a large DC current, which acts as a large magnetic pulse, that may cause a switching of the magnetization direction[46,270,286]. According to literature[28,64,177], field-like spin-orbit torques are generated in the ferromagnetic/antiferromagnetic layer that act upon the magnetic order parameter that eventually causes that order parameter to switch directions after relaxation. Excluding thermal effects, the field-like torque should be proportional to the planar Hall effect, which is used to understand the switching behavior and serve has a map, and the damping-like torques be proportional to the anomalous Hall effect, which we do not measure here.

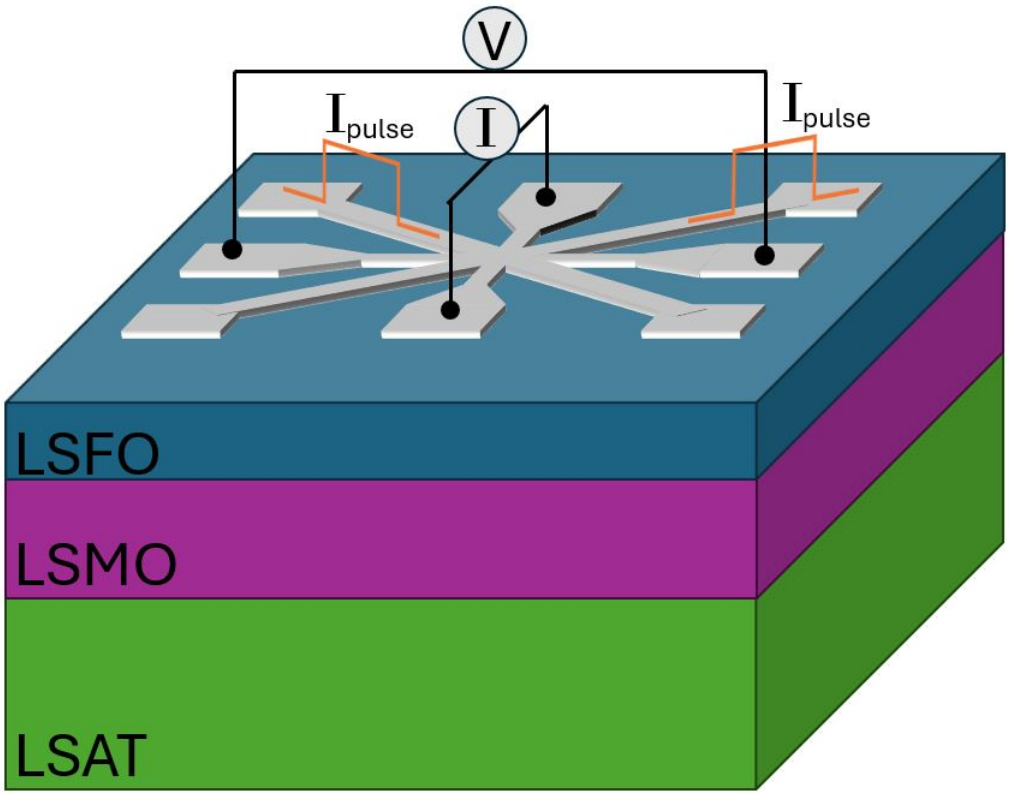

Figure 10.3: Schematic illustration of the 8-terminal device on the perovskite heterostructure. V is the measurable transverse voltage, I is a low DC current on the order of only a few μA, and I_{pulse}, represented by the orange square pulse, is a large DC current on the order of several mA to drive oscillations of the magnetization for SOT.

These 8-terminal structures were fabrication via e-beam lithography onto two samples: the LSFO/LSMO/LSAT structure and a reference structure SiO_x/3 nm Py ($Ni_{81}Fe_{19}$)/10 nm Pt.

Planar Hall effect (PHE) results can be seen in Figure 10.4 for the Py/Pt reference sample. We record the voltage response of a Keithley 2182a nanovoltmeter with a low externally applied magnetic field sweep from 10 Oe to -10 Oe at 300 K. Py is a ferromagnetic conductor that does not require large magnetic fields to saturate[148] and often characterized as a soft ferromagnet with its low coercivity[3]. We can see the sample saturates as low as 10 Oe and two notable dips in the voltage response

near ±1 Oe, in line with typical values of its coercivity. The PHE response is typical values from literature[204].

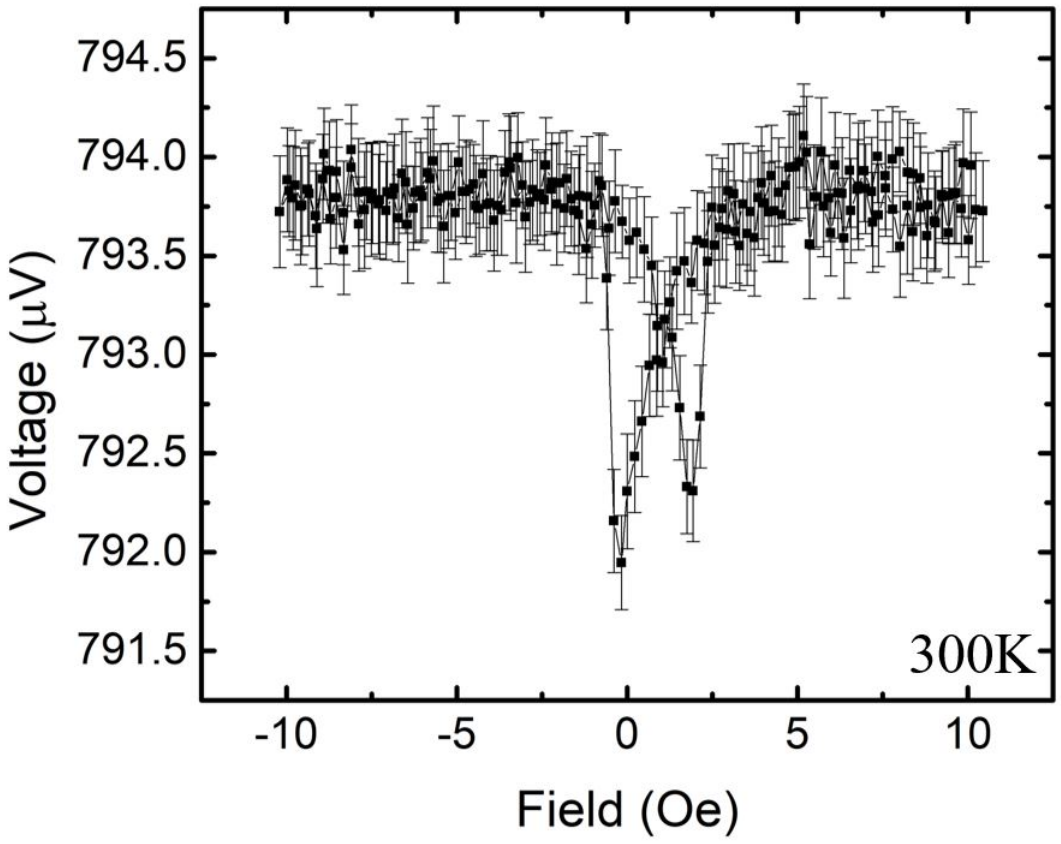

Figure 10.4: Voltage data versus externally applied magnetic field for a SiOx/Py/Pt sample with the magnetic field orientated at 45° with respect to the applied DC current. This measurement was performed at 300 K and shows two notable dips near ±1 Oe.

The PHE data is used to coordinate the pulse experiment. We can follow the PHE response curve to organize a sequence for the current pulse experiments. We can reset the magnetic moments by saturating the ferromagnetic material and then decrease the applied field to the coercive field (i.e. the lowest resistance peak in the PHE data). Pulsing with a large current will cause magnetic moments to oscillate and eventually relax into a more stable configuration. The pulse experiment follows this

sequential order: saturate the magnetic moments, lower the field to a low point on the PHE curve, pulse along one wire, pulse along a different wire that is 90° rotated from the first, and repeat. Figure 10.5 show the results of a pulse experiment on the Py/Pt sample at 300 K and with a pulse magnitude of 16.7 mA.

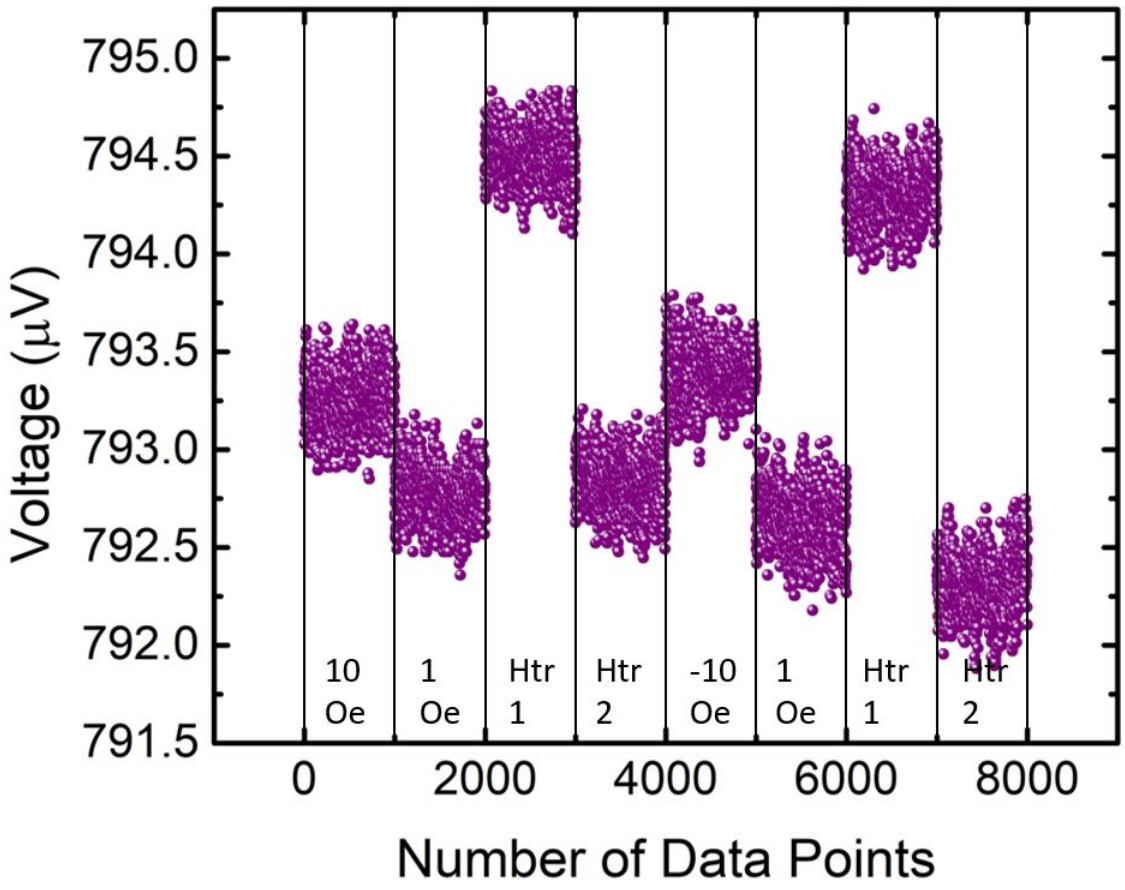

Figure 10.5: The pulse results for a SiO_x/Py/Pt sample. Outlined in the figure are the individual stages of the experiment wit data sectioned accordingly.

From the figure, "Htr 1" and "Htr 2" represent the larger width wires that are angled at 45° with respect to both the low DC current tap and voltage tap. Refer to Figure 10.3 for context. From the 10 Oe saturated voltage, we decrease the field to 1 Oe, and note a slight decrease in voltage response in line with values measured on the PHE curve. We pulse along a 45° angled wire (Htr 1) and notice a sizable increase

in voltage response in line with the saturating values of the PHE curve. Pulsing along the $-45°$ angled wire (Htr 2), the voltage response decreases to values similar to those measured at the 1 Oe field. This pattern is repeated when using a -10 Oe field to reset the magnetic moments.

For a magnetically soft thin film, the magnetization is expected to be in the film plane due to shape anisotropy, unless the material exhibits a strong perpendicular anistropy.[237] Therefore, the planar Hall effect should be maximized at 45° angles. Doing the pulse experiment with an in-plane magnetic field oriented at 45° relative to the probing current direction gives the clearest results and follows the results from the PHE rather well. According to some literature, the read-out mechanism, that is the resistance measurements after each sequential step in the pulse experiments, could either be due to spin Hall magnetoresistnace, planar Hall effect, or a combination of both[63]. These changes in resistances following the current pulse and reading the transverse resistance should follow the PHE or measuring the longitudinal resistance for anisotropic magnetoresistance (AMR)[28,260]. Since the pulsing experiment follows reasonably well with the planar Hall results, it is reasonable to assume that we are causing a switching of the magnetization of the Py layer from these large DC current pulses.

In Figure 10.6 illustrates the PHE results of the LSFO/LSMO/LSAT perovskite sample. This measurement was conducted at 78 K for the clearest results since it disappears near room temperature since the Curie temperature of the LSMO layer is near room temperature[151,288]. Like the Py/Pt sample, we see two distinguishable and symmetric peaks at ± 95 Oe corresponding to the coercivity of the LSMO layer.

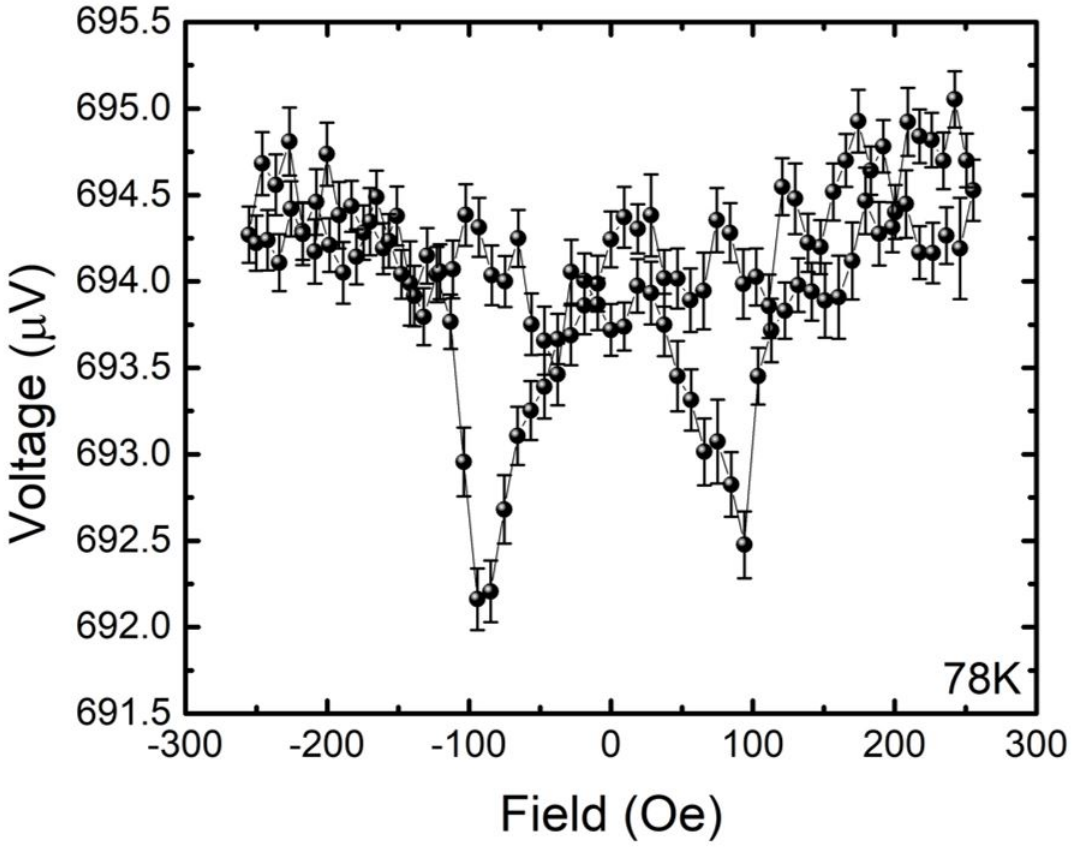

Figure 10.6: The planar Hall effect at 78 K for the LSFO/LSMO/LSAT perovskite sample.

Following a similar procedure with the Py/Pt sample, we pulse large DC currents through a Pt device on the surface of the LSFO layer of the perovskite heterostructure. This pulse experiment was conducted at 78 K to coincide with the PHE results. Saturating the LSMO magnetization at an applied magnetic field of 250 Oe, decreasing the magnetic field strength to 90 Oe to align with the lowest point on the PHE curve, and pulse a large DC current on "Htr 1" and ""Htr 2" back and forth for several loops. The pulse experiment data can be viewed in Figure 10.7.

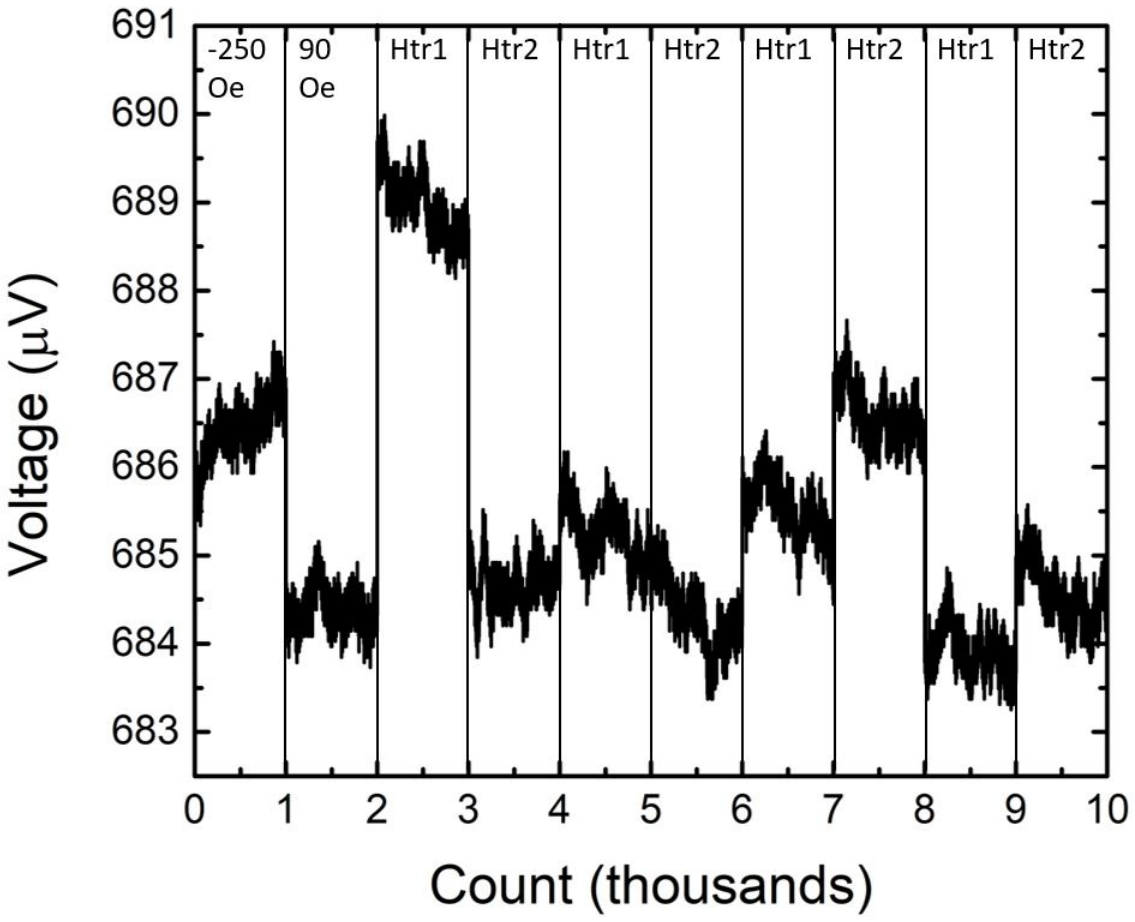

Figure 10.7: Voltage response for the pulse experiment on the LSFO/LSMO/LSAT IN042 perovskite. Each step of the sequence are separated for clarity and labeled. "Htr 1" and "Htr 2" represent the 45° and −45° angled wires with respect to the voltage taps that carry the current pulses, respectively. Data was collected at 78 K in line with the PHE data in Figure 10.6.

From Figure 10.7, we note that the voltage of the initial reset of the magnetization of the LSMO layer by saturating it with a -250 Oe in-plane magnetic field is slightly higher than those seen from the PHE data at saturation. Decreasing the field strength to 90 Oe drops the voltage response to values similar to those seen in the PHE data. Pulsing on the "Htr 1" wire causes the voltage to suddenly jump to values greater than that of the saturating values and pulsing on "Htr 2" drops the voltage response back to values seen at 90 Oe. This pattern is similar to that seen in

the Py/Pt reference sample; however, repetition is absent in this perovskite sample. Repeating current pulses on "Htr 1" and "Htr 2" does not repeat the initial high and low states. In any attempted current pulsing experiment, the features in the Py/Pt reference does not occur in the perovskite heterostructure.

The presence of pinholes on the surface of the LSFO layer that create uncontrolled current pathways between the insulating LSFO and conductive LSMO underneath may be diverting a substantial component of the current pulse away from the intended area and electrically shorting these two layers. Without the required current pulse magnitude to effectively switch the magnetic order parameter, the consistent switching as seen in our reference sample is absent from the perovskite heterostructure.

10.4. CONCLUSION

The insulating antiferromagnetic lanthanum strontium ferrite and conductive ferromagnetic lanthanum strontium manganite, spin-flop coupled heterostructure shows potentially interesting spintronic applications for magnetic switching. Unfortunately, a more robust growth process needs to be implemented to avoid pinholes that electrically shorts the two perovskite layers together. If the prevailing pinhole problem is unavoidable, then a revised methodology for spin transport in this heterostructure needs to be realized.

CHAPTER 11: CONCLUSION

In the course of this research, a diverse array of devices and measurement techniques were employed to comprehensively characterize the charge, heat, and spin transport in various thin film systems.

I investigated the non-local resistance in both amorphous germanium and silicon nitride systems, utilizing non-local devices fabricated from platinum. Conventional measurement techniques such as differential conductance and delta mode initially suggested spin transport through the observation of a negative non-local resistance; however, further analysis using a lock-in amplifier revealed that these findings were attributable to dominant out-of-phase components to the signal, characterized by a combination of inductive and capacitive signals.

Moreover, longitudinal spin Seebeck measurements were conducted on thermally-evaporated chromium thin films deposited onto a bulk polycrystalline yttrium-iron-garnet, an commonly used insulating ferromagnetic material. Remarkably, the thermally-evaporated chromium exhibited spin Seebeck voltages comparable to those of a sputtered platinum sample under similar experimental conditions. A thickness dependent study unveiled an enhancement in spin-to-charge efficiency for thermally-evaporated chromium within the range of 6 nm to 11 nm, peaking at 10 nm. This enhancement, reaching an efficiency of 50% compared to literature data on sputtered chromium, was attributed to the influence of film thickness on the strain state, subsequently modifying the spin-density wave nature of the film.

Continued research on the longitudinal spin Seebeck effect in thermally-evaporated chromium lead to a temperature dependent study of another 10 nm film, grown under similar conditions. The study revealed an enhancement of the spin See-

beck voltage below 200 K, maximizing at 100 K. Sensitivity measurements, defined as dR/dT∗(T/R), indicated two distinct peaks centered near 350 K and 200 K. These two peaks are likely two separate Néel temperatures. Above 350 K, the chromium assumes a paramagnetic state. In temperatures between these Néel points, the chromium transitions into a mixed state marked by domains of antiferromagnetic commensurate spin-density waves and paramagnetic incommensurate spin-density waves. Temperatures below 200 K, the entirety of the chromium film is in a antiferromagnetic state. This behavior may be due to a combination of disorder and stress in the film that is otherwise absent in the sputtered films.

Investigations into the magnetoresistnace response of thermally-evaporated and sputtered chromium thin films vastly different behaviors under an externally applied in-plane magnetic field. While the evaporated chromium film displayed a symmetric behavior aligning with predictions from spin Hall magnetoresistance and anistropic magnetoresistance, the sputtered chromium thin film exhibited a dominant anomalous Hall-like asymmetric contribution, possibly arising from interface magnetic proximity effects and oxidation effects.

Lastly, experimental work on a spin-flop coupled insulating antiferromagnetic lanthanum strontium ferrite/conductive ferromagnetic lanthanum strontium manganite heterostructure revealed complex magnetic behavior. Attempts at magnetic switching using current pulses encountered challenges, potentially stemming from pinholes causes electrical shorts between the insulating and conductive layers. These unexpected conductive pathways complicated magnetic switching dynamics, diverting the current intended for field-like spin-orbit torques and leading to experimental limitations.

REFERENCES

[1] Abadias, G., Chason, E., Keckes, J., Sebastiani, M., Thompson, G. B., Barthel, E., Doll, G. L., Murray, C. E., Stoessel, C. H., & Martinu, L. (2018). Review Article: Stress in thin films and coatings: Current status, challenges, and prospects. *Journal of Vacuum Science & Technology A*, *36*(2), 020801.
URL https://doi.org/10.1116/1.5011790

[2] Adachi, H., ichi Uchida, K., Saitoh, E., & Maekawa, S. (2013). Theory of the spin seebeck effect. *Reports on Progress in Physics*, *76*(3), 036501.
URL https://dx.doi.org/10.1088/0034-4885/76/3/036501

[3] Akhter, M. A., Mapps, D. J., Ma Tan, Y. Q., Petford-Long, A., & Doole, R. (1997). Thickness and grain-size dependence of the coercivity in permalloy thin films. *Journal of Applied Physics*, *81*(8), 4122–4124.
URL https://doi.org/10.1063/1.365100

[4] Althammer, M., Meyer, S., Nakayama, H., Schreier, M., Altmannshofer, S., Weiler, M., Huebl, H., Geprägs, S., Opel, M., Gross, R., Meier, D., Klewe, C., Kuschel, T., Schmalhorst, J.-M., Reiss, G., Shen, L., Gupta, A., Chen, Y.-T., Bauer, G. E. W., Saitoh, E., & Goennenwein, S. T. B. (2013). Quantitative study of the spin hall magnetoresistance in ferromagnetic insulator/normal metal hybrids. *Phys. Rev. B*, *87*, 224401.
URL https://link.aps.org/doi/10.1103/PhysRevB.87.224401

[5] Ando, K., Kajiwara, Y., Takahashi, S., Maekawa, S., Takemoto, K., Takatsu, M., & Saitoh, E. (2008). Angular dependence of inverse spin–hall effect induced by spin pumping investigated in a $ni_{81}fe_{19}$/Pt thin film. *Phys. Rev. B*, *78*, 014413.
URL https://link.aps.org/doi/10.1103/PhysRevB.78.014413

[6] Ando, K., & Saitoh, E. (2010). Inverse spin-Hall effect in palladium at room temperature. *Journal of Applied Physics*, *108*(11), 113925.
URL https://doi.org/10.1063/1.3517131

[7] Apalkov, D., Dieny, B., & Slaughter, J. M. (2016). Magnetoresistive random access memory. *Proceedings of the IEEE*, *104*(10), 1796–1830.

[8] Arenholz, E., van der Laan, G., Yang, F., Kemik, N., Biegalski, M. D., Christen, H. M., & Takamura, Y. (2009). Magnetic structure of La0.7Sr0.3MnO3/La0.7Sr0.3FeO3 superlattices. *Applied Physics Letters*,

94(7), 072503.
URL https://doi.org/10.1063/1.3085765

[9] Arrott, A., Werner, S. A., & Kendrick, H. (1965). First-order magnetic phase change in chromium at 38.5°c. *Phys. Rev. Lett.*, *14*, 1022–1024.
URL https://link.aps.org/doi/10.1103/PhysRevLett.14.1022

[10] Asylum (????). *MFP-3D Manual*. Asylum Research.

[11] Avci, C. O., Garello, K., Ghosh, A., Gabureac, M., Alvarado, S. F., & Gambardella, P. (2015). Unidirectional spin hall magnetoresistance in ferromagnet/normal metal bilayers. *Nature Physics*, *11*(7), 570–575.
URL https://doi.org/10.1038/nphys3356

[12] Avery, A. D., Pufall, M. R., & Zink, B. L. (2012). Determining the planar nernst effect from magnetic-field-dependent thermopower and resistance in nickel and permalloy thin films. *Phys. Rev. B*, *86*, 184408.
URL https://link.aps.org/doi/10.1103/PhysRevB.86.184408

[13] Avery, A. D., Pufall, M. R., & Zink, B. L. (2012). Observation of the planar nernst effect in permalloy and nickel thin films with in-plane thermal gradients. *Phys. Rev. Lett.*, *109*, 196602.
URL https://link.aps.org/doi/10.1103/PhysRevLett.109.196602

[14] Azevedo, A., Vilela-Leão, L. H., Rodríguez-Suárez, R. L., Lacerda Santos, A. F., & Rezende, S. M. (2011). Spin pumping and anisotropic magnetoresistance voltages in magnetic bilayers: Theory and experiment. *Phys. Rev. B*, *83*, 144402.
URL https://link.aps.org/doi/10.1103/PhysRevB.83.144402

[15] Baltz, V., Manchon, A., Tsoi, M., Moriyama, T., Ono, T., & Tserkovnyak, Y. (2018). Antiferromagnetic spintronics. *Rev. Mod. Phys.*, *90*, 015005.
URL https://link.aps.org/doi/10.1103/RevModPhys.90.015005

[16] Bartzsch, H., Glöß, D., Böcher, B., Frach, P., & Goedicke, K. (2003). Properties of sio2 and al2o3 films for electrical insulation applications deposited by reactive pulse magnetron sputtering. *Surface and Coatings Technology*, *174-175*, 774–778. Proceedings of the Eight International Conference on Plasma Surface Engineering.
URL https://www.sciencedirect.com/science/article/pii/S0257897203003840

[17] Bauer, G. E. W. (2020). Anisotropic magnetoresistance: A 170-year-old puzzle solved. *Science China Physics, Mechanics & Astronomy*, *64*(1), 217531.
URL https://doi.org/10.1007/s11433-020-1618-7

[18] Bauer, G. E. W., Saitoh, E., & van Wees, B. J. (2012). Spin caloritronics. *Nature Materials*, *11*(5), 391–399.
URL https://doi.org/10.1038/nmat3301

[19] Baxter, D. V., Ruzmetov, D., Scherschligt, J., Sasaki, Y., Liu, X., Furdyna, J. K., & Mielke, C. H. (2002). Anisotropic magnetoresistance in $ga_{1-x}mn_xAs$. *Phys. Rev. B*, *65*, 212407.
URL https://link.aps.org/doi/10.1103/PhysRevB.65.212407

[20] Bednorz, J. G., & Müller, K. A. (1988). Perovskite-type oxides—the new approach to high-T_c superconductivity. *Rev. Mod. Phys.*, *60*, 585–600.
URL https://link.aps.org/doi/10.1103/RevModPhys.60.585

[21] Behnia, K. (2015). 1Basic Concepts. In *Fundamentals of Thermoelectricity*. Oxford University Press.
URL https://doi.org/10.1093/acprof:oso/9780199697663.003.0001

[22] Behnia, K., & Aubin, H. (2016). Nernst effect in metals and superconductors: a review of concepts and experiments. *Reports on Progress in Physics*, *79*(4), 046502.
URL https://dx.doi.org/10.1088/0034-4885/79/4/046502

[23] Berger, L. (1964). Influence of spin-orbit interaction on the transport processes in ferromagnetic nickel alloys, in the presence of a degeneracy of the 3d band. *Physica*, *30*(6), 1141–1159.
URL https://www.sciencedirect.com/science/article/pii/0031891464901053

[24] Berger, L. (1996). Emission of spin waves by a magnetic multilayer traversed by a current. *Phys. Rev. B*, *54*, 9353–9358.
URL https://link.aps.org/doi/10.1103/PhysRevB.54.9353

[25] Bethe, H. A. (1951). Theory of atomic collisions. *Nature*, *167*, 165–165.

[26] Bleser, S. M., Greening, R. M., Roos, M. J., Hernandez, L. A., Fan, X., & Zink, B. L. (2022). Negative spin Hall angle and large spin-charge conversion in thermally evaporated chromium thin films. *Journal of Applied Physics*, *131*(11). 113904.
URL https://doi.org/10.1063/5.0085352

[27] Bödeker, P., Schreyer, A., Zabel, & H. (1999). Spin-density waves and reorientation effects in thin epitaxial cr films covered with ferromagnetic and paramagnetic layers. *Phys. Rev. B*, *59*, 9408–9431.
URL https://link.aps.org/doi/10.1103/PhysRevB.59.9408

[28] Bodnar, S. Y., Šmejkal, L., Turek, I., Jungwirth, T., Gomonay, O., Sinova, J., Sapozhnik, A. A., Elmers, H.-J., Kläui, M., & Jourdan, M. (2018). Writing and reading antiferromagnetic mn2au by néel spin-orbit torques and large anisotropic magnetoresistance. *Nature Communications*, *9*(1), 348.
URL https://doi.org/10.1038/s41467-017-02780-x

[29] Boekelheide, Z., Cooke, D. W., Helgren, E., & Hellman, F. (2009). Resonant impurity scattering and electron-phonon scattering in the electrical resistivity of cr thin films. *Phys. Rev. B*, *80*, 134426.
URL https://link.aps.org/doi/10.1103/PhysRevB.80.134426

[30] Boekelheide, Z., Helgren, E., & Hellman, F. (2007). Spin-density wave in polycrystalline cr films from infrared reflectivity. *Phys. Rev. B*, *76*, 224429.
URL https://link.aps.org/doi/10.1103/PhysRevB.76.224429

[31] Boona, S. R., Myers, R. C., & Heremans, J. P. (2014). Spin caloritronics. *Energy Environ. Sci.*, *7*, 885–910.
URL http://dx.doi.org/10.1039/C3EE43299H

[32] Bougiatioti, P., Klewe, C., Meier, D., Manos, O., Kuschel, O., Wollschläger, J., Bouchenoire, L., Brown, S. D., Schmalhorst, J.-M., Reiss, G., & Kuschel, T. (2017). Quantitative disentanglement of the spin seebeck, proximity-induced, and ferromagnetic-induced anomalous nernst effect in normal-metal–ferromagnet bilayers. *Phys. Rev. Lett.*, *119*, 227205.
URL https://link.aps.org/doi/10.1103/PhysRevLett.119.227205

[33] Cai, Y., Li, W., Wu, Y., Meng, K., Miao, J., Xu, X., & Jiang, Y. (2019). Comparative measurements of local and nonlocal spin seebeck effect in yig/pt nano-thick films. *Journal of Magnetism and Magnetic Materials*, *476*, 166–170.
URL https://www.sciencedirect.com/science/article/pii/S0304885318328543

[34] Cesaria, M., Caricato, A. P., Maruccio, G., & Martino, M. (2011). Lsmo – growing opportunities by pld and applications in spintronics. *Journal of Physics: Conference Series*, *292*(1), 012003.
URL https://dx.doi.org/10.1088/1742-6596/292/1/012003

[35] Chen, H., Feng, Z., Yan, H., Qin, P., Zhou, X., Guo, H., Wang, X., Wu, H., Zhang, X., Meng, Z., & Liu, Z. (2021). Anomalous hall effect in antiferromagnetic cr thin films. *Phys. Rev. B*, *104*, 064428.
URL https://link.aps.org/doi/10.1103/PhysRevB.104.064428

[36] Chen, X., Shi, S., Shi, G., Fan, X., Song, C., Zhou, X., Bai, H., Liao, L., Zhou, Y., Zhang, H., Li, A., Chen, Y., Han, X., Jiang, S., Zhu, Z., Wu, H., Wang, X., Xue, D., Yang, H., & Pan, F. (2021). Observation of the antiferromagnetic spin hall effect. *Nature Materials*, *20*(6), 800–804.
URL https://doi.org/10.1038/s41563-021-00946-z

[37] Chen, X., Zhou, X., Cheng, R., Cheng, S., Zhang, J., Wu, Y., Ba, Y., Li, H., Sun, Y., You, Y., Zhao, Y., & Pan, F. (2019). Electric field control of néel spin–orbit torque in an antiferromagnet. *Nature Materials*, *18*(9), 931–935. Copyright - Copyright Nature Publishing Group Sep 2019; Last updated - 2019-08-22.
URL https://du.idm.oclc.org/login?url=https://www.proquest.com/scholarly-journals/electric-field-control-nÃľel-spin-orbit-torque/docview/2277418925/se-2

[38] Chen, X. Z., Zarzuela, R., Zhang, J., Song, C., Zhou, X. F., Shi, G. Y., Li, F., Zhou, H. A., Jiang, W. J., Pan, F., & Tserkovnyak, Y. (2018). Antidamping-torque-induced switching in biaxial antiferromagnetic insulators. *Phys. Rev. Lett.*, *120*, 207204.
URL https://link.aps.org/doi/10.1103/PhysRevLett.120.207204

[39] Chen, Y.-J., & Huang, S.-Y. (2019). Light-induced thermal spin current. *Phys. Rev. B*, *99*, 094426.
URL https://link.aps.org/doi/10.1103/PhysRevB.99.094426

[40] Chen, Y.-T., Takahashi, S., Nakayama, H., Althammer, M., Goennenwein, S. T. B., Saitoh, E., & Bauer, G. E. W. (2013). Theory of spin hall magnetoresistance. *Phys. Rev. B*, *87*, 144411.
URL https://link.aps.org/doi/10.1103/PhysRevB.87.144411

[41] Chen, Y.-T., Takahashi, S., Nakayama, H., Althammer, M., Goennenwein, S. T. B., Saitoh, E., & Bauer, G. E. W. (2016). Theory of spin hall magnetoresistance (smr) and related phenomena. *Journal of Physics: Condensed Matter*, *28*(10), 103004.
URL https://dx.doi.org/10.1088/0953-8984/28/10/103004

[42] Chen, Z., Chen, P., Wang, Y., Wang, W., Zhang, Z., Lu, X., Liu, R., Fan, X., Yu, G., & Ma, F. (2023). Experimental observation of interfacial rashba-edelstein magnetoresistance in cr/yig heterostructures. *Phys. Rev. B*, *107*, 014408.
URL https://link.aps.org/doi/10.1103/PhysRevB.107.014408

[43] Cheng, S.-g., Xing, Y., Sun, Q.-f., & Xie, X. C. (2008). Spin nernst effect and nernst effect in two-dimensional electron systems. *Phys. Rev. B*, *78*, 045302.
URL https://link.aps.org/doi/10.1103/PhysRevB.78.045302

[44] Cheng, Y., Yu, S., Ahmed, A. S., Zhu, M., Rao, Y., Ghazisaeidi, M., Hwang, J., & Yang, F. (2019). Anisotropic magnetoresistance and nontrivial spin hall magnetoresistance in Pt/$\alpha-Fe_2o_3$ bilayers. *Phys. Rev. B*, *100*, 220408.
URL https://link.aps.org/doi/10.1103/PhysRevB.100.220408

[45] Cheriet, L., Arajs, S., & Helbig, H. F. (1990). Internal stresses and antiferromagnetism in evaporated Cr films. *Journal of Applied Physics*, *67*(9), 5672–5673.
URL https://doi.org/10.1063/1.345922

[46] Chiang, C. C., Huang, S. Y., Qu, D., Wu, P. H., & Chien, C. L. (2019). Absence of evidence of electrical switching of the antiferromagnetic néel vector. *Phys. Rev. Lett.*, *123*, 227203.
URL https://link.aps.org/doi/10.1103/PhysRevLett.123.227203

[47] Chiu, C.-C., Chang, Y.-W., Shao, Y.-C., Liu, Y.-C., Lee, J.-M., Huang, S.-W., Yang, W., Guo, J., de Groot, F. M. F., Yang, J.-C., & Chuang, Y.-D. (2021). Spectroscopic characterization of electronic structures of ultra-thin single crystal la0.7sr0.3mno3. *Scientific Reports*, *11*(1), 5250.
URL https://doi.org/10.1038/s41598-021-84598-8

[48] Cho, A., & Arthur, J. (1975). Molecular beam epitaxy. *Progress in Solid State Chemistry*, *10*, 157–191.
URL https://www.sciencedirect.com/science/article/pii/0079678675900059

[49] Cho, S., Baek, S.-h. C., Lee, K.-D., Jo, Y., & Park, B.-G. (2015). Large spin hall magnetoresistance and its correlation to the spin-orbit torque in w/cofeb/mgo structures. *Scientific Reports*, *5*(1), 14668.
URL https://doi.org/10.1038/srep14668

[50] Chuang, T. C., Su, P. L., Wu, P. H., & Huang, S. Y. (2017). Enhancement of the anomalous nernst effect in ferromagnetic thin films. *Phys. Rev. B*, *96*,

174406.
URL https://link.aps.org/doi/10.1103/PhysRevB.96.174406

[51] Cohen, R. E. (1992). Origin of ferroelectricity in perovskite oxides. *Nature*, *358*(6382), 136–138.
URL https://doi.org/10.1038/358136a0

[52] Coleman, R. V., & Isin, A. (2004). Magnetoresistance in Iron Single Crystals. *Journal of Applied Physics*, *37*(3), 1028–1029.
URL https://doi.org/10.1063/1.1708320

[53] Cornelissen, L. J., Liu, J., Duine, R. A., Youssef, J. B., & van Wees, B. J. (2015). Long-distance transport of magnon spin information in a magnetic insulator at room temperature. *Nature Physics*, *11*(12), 1022–1026.
URL https://doi.org/10.1038/nphys3465

[54] Cortazar-Martínez, O., Torres-Ochoa, J.-A., Raboño-Borbolla, J.-G., & Herrera-Gomez, A. (2021). Oxidation mechanism of metallic chromium at room temperature. *Applied Surface Science*, *542*, 148636.
URL https://www.sciencedirect.com/science/article/pii/S0169433220333948

[55] Crépieux, A., & Bruno, P. (2001). Theory of the anomalous hall effect from the kubo formula and the dirac equation. *Phys. Rev. B*, *64*, 014416.
URL https://link.aps.org/doi/10.1103/PhysRevB.64.014416

[56] Davey, J. E., & Pankey, T. (2003). Epitaxial GaAs Films Deposited by Vacuum Evaporation. *Journal of Applied Physics*, *39*(4), 1941–1948.
URL https://doi.org/10.1063/1.1656467

[57] Dennison, J., Brunson, J., Swaminathan, P., Green, N., & Frederickson, A. (2006). Methods for high resistivity measurements related to spacecraft-charging. *IEEE Transactions on Plasma Science*, *34*(5), 2191–2203.

[58] Ding, Z., Chen, B. L., Liang, J. H., Zhu, J., Li, J. X., & Wu, Y. Z. (2014). Spin hall magnetoresistance in Pt/fe$_3$o$_4$ thin films at room temperature. *Phys. Rev. B*, *90*, 134424.
URL https://link.aps.org/doi/10.1103/PhysRevB.90.134424

[59] Dow, H. S., Kim, W. S., & Lee, J. W. (2017). Thermal and electrical properties of silicon nitride substrates. *AIP Advances*, *7*(9), 095022.
URL https://doi.org/10.1063/1.4996314

[60] Drude, P. (1900). Zur elektronentheorie der metalle; ii. teil. galvanomagnetische und thermomagnetische effecte. *Annalen der Physik*, *308*(11), 369–402.
URL https://onlinelibrary.wiley.com/doi/abs/10.1002/andp.19003081102

[61] Du, C., Wang, H., Yang, F., & Hammel, P. C. (2014). Systematic variation of spin-orbit coupling with *d*-orbital filling: Large inverse spin hall effect in 3*d* transition metals. *Phys. Rev. B*, *90*, 140407.
URL https://link.aps.org/doi/10.1103/PhysRevB.90.140407

[62] Dunlap, M., & Adaskaveg, D. J. E. (1997). *Introduction to the Scanning Electron Microscope: Theory, Practice, & Procedures*. U. C. Davis.

[63] Dunz, M., Matalla-Wagner, T., & Meinert, M. (2020). Spin-orbit torque induced electrical switching of antiferromagnetic mnn. *Phys. Rev. Res.*, *2*, 013347.
URL https://link.aps.org/doi/10.1103/PhysRevResearch.2.013347

[64] DuttaGupta, S., Kurenkov, A., Tretiakov, O. A., Krishnaswamy, G., Sala, G., Krizakova, V., Maccherozzi, F., Dhesi, S. S., Gambardella, P., Fukami, S., & Ohno, H. (2020). Spin-orbit torque switching of an antiferromagnetic metallic heterostructure. *Nature Communications*, *11*(1), 5715.
URL https://doi.org/10.1038/s41467-020-19511-4

[65] Dyakonov, M., & Perel, V. (1971). Current-induced spin orientation of electrons in semiconductors. *Physics Letters A*, *35*(6), 459–460.
URL https://www.sciencedirect.com/science/article/pii/0375960171901964

[66] Dyakonov, M., & Perel, V. I. (1971). Possibility of orienting electron spins with current. *Journal of Experimental and Theoretical Physics Letters*, *13*, 467.

[67] Edelstein, V. (1990). Spin polarization of conduction electrons induced by electric current in two-dimensional asymmetric electron systems. *Solid State Communications*, *73*(3), 233–235.
URL https://www.sciencedirect.com/science/article/pii/003810989090963C

[68] Eden, N., Kopnov, G., Fraenkel, S., Goldstein, M., & Gerber, A. (2019). Longitudinal and transverse magnetoresistance in films with tilted out-of-plane magnetic anisotropy. *Phys. Rev. B*, *99*, 064432.
URL https://link.aps.org/doi/10.1103/PhysRevB.99.064432

[69] Falcón, H., Sánchez-Benítez, J., Martínez-Lope, M. J., Alonso, J. A., Krezhov, K., Spirov, I., & Ruskov, T. (2007). Neutron diffraction, mössbauer and magnetotransport study of fe-substituted derivatives of cacu3mn4o12 perovskite with

colossal magnetoresistance. *Journal of Physics: Condensed Matter*, *19*(35), 356209.
URL https://dx.doi.org/10.1088/0953-8984/19/35/356209

[70] Fawcett, E. (1988). Spin-density-wave antiferromagnetism in chromium. *Rev. Mod. Phys.*, *60*, 209–283.
URL https://link.aps.org/doi/10.1103/RevModPhys.60.209

[71] Fawcett, E. (1997). Spin-density-wave antiferromagnetism in the chromium system iii effects of volume strain and doping in cr alloys. *Physica B: Condensed Matter*, *239*(1), 71–76. Proceedings of the Workshop on Transition Metals and Compounds under Multiextreme Conditions.
URL https://www.sciencedirect.com/science/article/pii/S0921452697003815

[72] Fawcett, E., Alberts, H. L., Galkin, V. Y., Noakes, D. R., & Yakhmi, J. V. (1994). Spin-density-wave antiferromagnetism in chromium alloys. *Rev. Mod. Phys.*, *66*, 25–127.
URL https://link.aps.org/doi/10.1103/RevModPhys.66.25

[73] Fayaz, M. U., Saleem, M. S., Gu, Y., Zhou, X., Pan, F., & Song, C. (2019). Simultaneous detection of the spin Hall magnetoresistance and Joule heating-induced spin Seebeck effect in Gd3Fe5O12/Pt bilayers. *Journal of Applied Physics*, *126*(18), 183901.
URL https://doi.org/10.1063/1.5117172

[74] Feng, X.-Y., Zhang, Q.-H., Zhang, H.-W., Zhang, Y., Zhong, R., Lu, B.-W., Cao, J.-W., & Fan, X.-L. (2019). A review of current research on spin currents and spin–orbit torques*. *Chinese Physics B*, *28*(10), 107105.
URL https://dx.doi.org/10.1088/1674-1056/ab425e

[75] Fert, A., & Jaffrès, H. (2001). Conditions for efficient spin injection from a ferromagnetic metal into a semiconductor. *Phys. Rev. B*, *64*, 184420.
URL https://link.aps.org/doi/10.1103/PhysRevB.64.184420

[76] Fischer, J., Gomonay, O., Schlitz, R., Ganzhorn, K., Vlietstra, N., Althammer, M., Huebl, H., Opel, M., Gross, R., Goennenwein, S. T. B., & Geprägs, S. (2018). Spin hall magnetoresistance in antiferromagnet/heavy-metal heterostructures. *Phys. Rev. B*, *97*, 014417.
URL https://link.aps.org/doi/10.1103/PhysRevB.97.014417

[77] Franz, R., & Wiedemann, G. (1853). Ueber die wärme-leitungsfähigkeit der metalle.
URL https://doi.org/10.1002/andp.18531650802

[78] Freitas, P. P., & Berger, L. (1985). Observation of s-d exchange force between domain walls and electric current in very thin Permalloy films. *Journal of Applied Physics*, *57*(4), 1266–1269.
URL https://doi.org/10.1063/1.334524

[79] Fu, C., Guin, S. N., Watzman, S. J., Li, G., Liu, E., Kumar, N., Süß, V., Schnelle, W., Auffermann, G., Shekhar, C., Sun, Y., Gooth, J., & Felser, C. (2018). Large nernst power factor over a broad temperature range in polycrystalline weyl semimetal nbp. *Energy Environ. Sci.*, *11*, 2813–2820.
URL http://dx.doi.org/10.1039/C8EE02077A

[80] Fukami, S., Anekawa, T., Zhang, C., & Ohno, H. (2016). A spin-orbit torque switching scheme with collinear magnetic easy axis and current configuration. *Nature Nanotechnology*, *11*(7), 621–625. Copyright - Copyright Nature Publishing Group Jul 2016; Last updated - 2023-07-17.
URL https://du.idm.oclc.org/login?url=https://www.proquest.com/scholarly-journals/spin-orbit-torque-switching-scheme-with-collinear/docview/1802023280/se-2

[81] Fullerton, E. E., Bader, S., & Robertson, J. (1997). Spin-density-wave antiferromagnetism of cr in fe/cr(0 0 1) superlattices. *Physica B: Condensed Matter*, *237-238*, 234–238. Proceedings of the Yamada Conference XLV, the International Conference on the Physics of Transition Metals.
URL https://www.sciencedirect.com/science/article/pii/S0921452697001154

[82] Furuya, K. (2008). Nanofabrication by advanced electron microscopy using intense and focused beam. *Science and Technology of Advanced Materials*, *9*(1), 014110. PMID: 27877936.
URL https://doi.org/10.1088/1468-6996/9/1/014110

[83] Gamino, M., S. Santos, J., R. Souza, A., Melo, A., Della Pace, R., Silva, E., Oliveira, A., Rodríguez-Suárez, R., Bohn, F., & Correa, M. (2021). Longitudinal spin seebeck effect and anomalous nernst effect in cofeb/non-magnetic metal bilayers. *Journal of Magnetism and Magnetic Materials*, *527*, 167778.
URL https://www.sciencedirect.com/science/article/pii/S0304885321000548

[84] Ganichev, S. D., Ivchenko, E. L., Bel'kov, V. V., Tarasenko, S. A., Sollinger, M., Weiss, D., Wegscheider, W., & Prettl, W. (2002). Spin-galvanic effect. *Nature*,

417(6885), 153–156.
URL https://doi.org/10.1038/417153a

[85] Gay, T. J., & Dunning, F. B. (1992). Mott electron polarimetry. *Review of Scientific Instruments*, *63*(2), 1635–1651.
URL https://doi.org/10.1063/1.1143371

[86] Goldschmidt, V. M. (1926). Die gesetze der krystallochemie. *Naturwissenschaften*, *14*(21), 477–485.
URL https://doi.org/10.1007/BF01507527

[87] Gulbrandsen, S. A., Espedal, C., & Brataas, A. (2020). Spin hall effect in antiferromagnets. *Phys. Rev. B*, *101*, 184411.
URL https://link.aps.org/doi/10.1103/PhysRevB.101.184411

[88] Guo, E.-J., Cramer, J., Kehlberger, A., Ferguson, C. A., MacLaren, D. A., Jakob, G., & Kläui, M. (2016). Influence of thickness and interface on the low-temperature enhancement of the spin seebeck effect in yig films. *Phys. Rev. X*, *6*, 031012.
URL https://link.aps.org/doi/10.1103/PhysRevX.6.031012

[89] Guo, G. Y., Murakami, S., Chen, T.-W., & Nagaosa, N. (2008). Intrinsic spin hall effect in platinum: First-principles calculations. *Phys. Rev. Lett.*, *100*, 096401.
URL https://link.aps.org/doi/10.1103/PhysRevLett.100.096401

[90] Hahn, C., de Loubens, G., Klein, O., Viret, M., Naletov, V. V., & Ben Youssef, J. (2013). Comparative measurements of inverse spin hall effects and magnetoresistance in yig/pt and yig/ta. *Phys. Rev. B*, *87*, 174417.
URL https://link.aps.org/doi/10.1103/PhysRevB.87.174417

[91] Hall, E. (1881). Xviii. on the "rotational coefficient" in nickel and cobalt. *The London, Edinburgh, and Dublin Philosophical Magazine and Journal of Science*, *12*(74), 157–172.
URL https://doi.org/10.1080/14786448108627086

[92] Hall, E. H. (1879). On a new action of the magnet on electric currents. *American Journal of Mathematics*, *2*(3), 287–292.
URL http://www.jstor.org/stable/2369245

[93] Hammar, P. R., Bennett, B. R., Yang, M. J., & Johnson, M. (1999). Observation of spin injection at a ferromagnet-semiconductor interface. *Phys. Rev. Lett.*, *83*,

203–206.
URL https://link.aps.org/doi/10.1103/PhysRevLett.83.203

[94] Hao, Q., Chen, W., & Xiao, G. (2015). Beta (β) tungsten thin films: Structure, electron transport, and giant spin Hall effect. *Applied Physics Letters*, *106*(18), 182403.
URL https://doi.org/10.1063/1.4919867

[95] Hellman, F., Hoffmann, A., Tserkovnyak, Y., Beach, G. S. D., Fullerton, E. E., Leighton, C., MacDonald, A. H., Ralph, D. C., Arena, D. A., Dürr, H. A., Fischer, P., Grollier, J., Heremans, J. P., Jungwirth, T., Kimel, A. V., Koopmans, B., Krivorotov, I. N., May, S. J., Petford-Long, A. K., Rondinelli, J. M., Samarth, N., Schuller, I. K., Slavin, A. N., Stiles, M. D., Tchernyshyov, O., Thiaville, A., & Zink, B. L. (2017). Interface-induced phenomena in magnetism. *Rev. Mod. Phys.*, *89*, 025006.
URL https://link.aps.org/doi/10.1103/RevModPhys.89.025006

[96] Hench, L. L., & West, J. K. (1990). The sol-gel process. *Chemical Reviews*, *90*(1), 33–72.
URL https://doi.org/10.1021/cr00099a003

[97] Hirsch, J. E. (1999). Spin hall effect. *Phys. Rev. Lett*, *83*, 1834–1837.

[98] Hoffman, S., Sato, K., & Tserkovnyak, Y. (2013). Landau-lifshitz theory of the longitudinal spin seebeck effect. *Phys. Rev. B*, *88*, 064408.
URL https://link.aps.org/doi/10.1103/PhysRevB.88.064408

[99] Hoffmann, A. (2007). Pure spin-currents. *physica status solidi c*, *4*(11), 4236–4241.
URL https://onlinelibrary.wiley.com/doi/abs/10.1002/pssc.200775942

[100] Hoffmann, A. (2013). Spin hall effects in metals. *IEEE Transactions on Magnetics*, *49*(10), 5172–5193.

[101] Holanda, J., Alves Santos, O., Cunha, R. O., Mendes, J. B. S., Rodríguez-Suárez, R. L., Azevedo, A., & Rezende, S. M. (2017). Longitudinal spin seebeck effect in permalloy separated from the anomalous nernst effect: Theory and experiment. *Phys. Rev. B*, *95*, 214421.
URL https://link.aps.org/doi/10.1103/PhysRevB.95.214421

[102] Huang, L., Li, Z., Zhang, C., Kong, L., Wang, B., Huang, S., Sharma, V., Ma, H., Yuan, Q., Liu, Y., Shen, G., Wu, K., & Li, L. (2019). Sacrificial oxidation

of a self-metal source for the rapid growth of metal oxides on quantum dots towards improving photostability. *Chem. Sci.*, *10*, 6683–6688.
URL http://dx.doi.org/10.1039/C9SC01233H

[103] Huang, S. Y., Fan, X., Qu, D., Chen, Y. P., Wang, W. G., Wu, J., Chen, T. Y., Xiao, J. Q., & Chien, C. L. (2012). Transport magnetic proximity effects in platinum. *Phys. Rev. Lett.*, *109*, 107204.
URL https://link.aps.org/doi/10.1103/PhysRevLett.109.107204

[104] Huang, S. Y., Wang, W. G., Lee, S. F., Kwo, J., & Chien, C. L. (2011). Intrinsic spin-dependent thermal transport. *Phys. Rev. Lett.*, *107*, 216604.
URL https://link.aps.org/doi/10.1103/PhysRevLett.107.216604

[105] Idzuchi, H., Fukuma, Y., & Otani, Y. (2015). Spin transport in non-magnetic nano-structures induced by non-local spin injection. *Physica E: Low-dimensional Systems and Nanostructures*, *68*, 239–263.
URL https://www.sciencedirect.com/science/article/pii/S1386947714004305

[106] Žutić, I., Fabian, J., & Das Sarma, S. (2004). Spintronics: Fundamentals and applications. *Rev. Mod. Phys.*, *76*, 323–410.
URL https://link.aps.org/doi/10.1103/RevModPhys.76.323

[107] Iguchi, R., Ando, K., Qiu, Z., An, T., Saitoh, E., & Sato, T. (2013). Spin pumping by nonreciprocal spin waves under local excitation. *Applied Physics Letters*, *102*(2), 022406.
URL https://doi.org/10.1063/1.4775685

[108] Ikhlas, M., Tomita, T., Koretsune, T., Suzuki, M.-T., Nishio-Hamane, D., Arita, R., Otani, Y., & Nakatsuji, S. (2017). Large anomalous nernst effect at room temperature in a chiral antiferromagnet. *Nature Physics*, *13*(11), 1085–1090.
URL https://doi.org/10.1038/nphys4181

[109] Inoue, H. Y., Harii, K., Ando, K., Sasage, K., & Saitoh, E. (2007). Detection of pure inverse spin-Hall effect induced by spin pumping at various excitation. *Journal of Applied Physics*, *102*(8), 083915.
URL https://doi.org/10.1063/1.2799068

[110] Isasa, M., Villamor, E., Hueso, L. E., Gradhand, M., & Casanova, F. (2015). Temperature dependence of spin diffusion length and spin hall angle in au and pt. *Phys. Rev. B*, *91*, 024402.
URL https://link.aps.org/doi/10.1103/PhysRevB.91.024402

[111] Jaworski, C. M., Yang, J., Mack, S., Awschalom, D. D., Heremans, J. P., & Myers, R. C. (2010). Observation of the spin-seebeck effect in a ferromagnetic semiconductor. *Nature Materials*, *9*(11), 898–903.
URL https://doi.org/10.1038/nmat2860

[112] Jedema, F. J., Filip, A. T., & van Wees, B. J. (2001). Electrical spin injection and accumulation at room temperature in an all-metal mesoscopic spin valve. *Nature*, *410*(6826), 345–348.
URL https://doi.org/10.1038/35066533

[113] Ji, Y., Hoffmann, A., Jiang, J. S., Pearson, J. E., & Bader, S. D. (2007). Non-local spin injection in lateral spin valves. *Journal of Physics D: Applied Physics*, *40*(5), 1280.
URL https://dx.doi.org/10.1088/0022-3727/40/5/S13

[114] Jia, T., Zeng, Z., Lin, H. Q., Duan, Y., & Ohodnicki, P. (2017). First-principles study on the electronic, optical and thermodynamic properties of abo3 (a = la,sr, b = fe,co) perovskites. *RSC Adv.*, *7*, 38798–38804.
URL http://dx.doi.org/10.1039/C7RA06542F

[115] Jia, Y., Chopdekar, R. V., Arenholz, E., Young, A. T., Marcus, M. A., Mehta, A., & Takamura, Y. (2015). Exchange coupling in (111)-oriented $La_{0.7}Sr_{0.3}Mno_3/La_{0.7}Sr_{0.3}Feo_3$ superlattices. *Phys. Rev. B*, *92*, 094407.
URL https://link.aps.org/doi/10.1103/PhysRevB.92.094407

[116] Jia, Y., Chopdekar, R. V., Shafer, P., Arenholz, E., Liu, Z., Biegalski, M. D., & Takamura, Y. (2017). Antiferromagnetic structure of exchange-coupled $La_{0.7}Sr_{0.3}Feo_3$ thin films studied using angle-dependent x-ray absorption spectroscopy. *Phys. Rev. B*, *96*, 214411.
URL https://link.aps.org/doi/10.1103/PhysRevB.96.214411

[117] Johnson, M., & Silsbee, R. H. (1987). Thermodynamic analysis of interfacial transport and of the thermomagnetoelectric system. *Phys. Rev. B*, *35*, 4959–4972.
URL https://link.aps.org/doi/10.1103/PhysRevB.35.4959

[118] Jungwirth, T., Wunderlich, J., & Olejník, K. (2012). Spin hall effect devices. *Nature Materials*, *11*(5), 382–390.
URL https://doi.org/10.1038/nmat3279

[119] Kajiwara, Y., Harii, K., Takahashi, S., Ohe, J., Uchida, K., Mizuguchi, M., Umezawa, H., Kawai, H., Ando, K., Takanashi, K., Maekawa, S., & Saitoh,

E. (2010). Transmission of electrical signals by spin-wave interconversion in a magnetic insulator. *Nature*, *464*(7286), 262–266.
URL https://doi.org/10.1038/nature08876

[120] Kalaswad, M., Zhang, B., Wang, H., Wang, X., Huang, J., & Wang, H. (2020). Tailorable fe nanostructures and magnetic anisotropy in (la0.5sr0.5feo3)1-x:fex thin films integrated on srtio3 and silicon substrates. *Materials Today Advances*, *8*, 100112.
URL https://www.sciencedirect.com/science/article/pii/S259004982030059X

[121] Kannan, H., Fan, X., Celik, H., Han, X., & Xiao, J. Q. (2017). Thickness dependence of anomalous nernst coefficient and longitudinal spin seebeck effect in ferromagnetic $ni_x fe_{100-x}$ films. *Scientific Reports*, 7(1), 6175.
URL https://doi.org/10.1038/s41598-017-05946-1

[122] Karplus, R., & Luttinger, J. M. (1954). Hall effect in ferromagnetics. *Phys. Rev.*, *95*, 1154–1160.
URL https://link.aps.org/doi/10.1103/PhysRev.95.1154

[123] Kato, Y. K., Myers, R. C., Gossard, A. C., & Awschalom, D. D. (2004). Observation of the spin hall effect in semiconductors. *Science*, *306*(5703), 1910–1913.
URL https://www.science.org/doi/abs/10.1126/science.1105514

[124] Kikkawa, T., Uchida, K., Daimon, S., Shiomi, Y., Adachi, H., Qiu, Z., Hou, D., Jin, X.-F., Maekawa, S., & Saitoh, E. (2013). Separation of longitudinal spin seebeck effect from anomalous nernst effect: Determination of origin of transverse thermoelectric voltage in metal/insulator junctions. *Phys. Rev. B*, *88*, 214403.
URL https://link.aps.org/doi/10.1103/PhysRevB.88.214403

[125] Kikkawa, T., Uchida, K., Shiomi, Y., Qiu, Z., Hou, D., Tian, D., Nakayama, H., Jin, X.-F., & Saitoh, E. (2013). Longitudinal spin seebeck effect free from the proximity nernst effect. *Phys. Rev. Lett.*, *110*, 067207.
URL https://link.aps.org/doi/10.1103/PhysRevLett.110.067207

[126] Kikkawa, T., Uchida, K.-i., Daimon, S., Qiu, Z., Shiomi, Y., & Saitoh, E. (2015). Critical suppression of spin seebeck effect by magnetic fields. *Phys. Rev. B*, *92*, 064413.
URL https://link.aps.org/doi/10.1103/PhysRevB.92.064413

[127] Kim, J., Sheng, P., Takahashi, S., Mitani, S., & Hayashi, M. (2016). Spin hall magnetoresistance in metallic bilayers. *Phys. Rev. Lett.*, *116*, 097201.
URL https://link.aps.org/doi/10.1103/PhysRevLett.116.097201

[128] Kimura, T., Otani, Y., Sato, T., Takahashi, S., & Maekawa, S. (2007). Room-temperature reversible spin hall effect. *Phys. Rev. Lett.*, *98*, 156601.
URL https://link.aps.org/doi/10.1103/PhysRevLett.98.156601

[129] Kishimoto, S. (2012). Electron moiré method. *Theoretical and Applied Mechanics Letters*, *2*(1), 011001.
URL https://www.sciencedirect.com/science/article/pii/S2095034915301082

[130] Kittel, C. (1991). *Quantum Theory of Solids, 2nd Revised Edition*. 111 River Street Hoboken, NJ: Wiley.

[131] Kittel, C. (2004). *Intoduction to Solid State Physics, 8th Edition*. 111 River Street Hoboken, NJ: Wiley.

[132] Koch, R. (2010). Stress in evaporated and sputtered thin films – a comparison. *Surface and Coatings Technology*, *204*(12), 1973–1982. Proceedings of the European Materials Research Socierty (E-MRS)Spring Meeting 2009.
URL https://www.sciencedirect.com/science/article/pii/S0257897209007464

[133] Koinuma, H., Nagata, H., Tsukahara, T., Gonda, S., & Yoshimoto, M. (1991). Ceramic layer epitaxy by pulsed laser deposition in an ultrahigh vacuum system. *Applied Physics Letters*, *58*(18), 2027–2029.
URL https://doi.org/10.1063/1.105002

[134] Korotin, M. A., Anisimov, V. I., Khomskii, D. I., & Sawatzky, G. A. (1998). cro_2: A self-doped double exchange ferromagnet. *Phys. Rev. Lett.*, *80*, 4305–4308.
URL https://link.aps.org/doi/10.1103/PhysRevLett.80.4305

[135] Kravtsov, E., Brucas, R., Hjörvarsson, B., Hoser, A., McIntyre, G., Nefedov, A., Radu, F., Remhof, A., & Zabel, H. (2005). Proximity effect of vanadium on strain and spin-density waves in thin cr films. *Journal of Magnetism and Magnetic Materials*, *286*, 425–431. Proceedings of the 5th International Symposium on Metallic Multilayers.
URL https://www.sciencedirect.com/science/article/pii/S0304885304009576

[136] Kulikov, N. I., & Tugushev, V. V. (1984). Spin-density waves and itinerant antiferromagnetism in metals. *Soviet Physics Uspekhi*, *27*(12), 954.
URL https://dx.doi.org/10.1070/PU1984v027n12ABEH004088

[137] Kulkarni, A., & Chang, L. (1997). Electrical and structural characteristics of chromium thin films deposited on glass and alumina substrates. *Thin Solid Films*, *301*(1), 17–22.
URL https://www.sciencedirect.com/science/article/pii/S0040609096095533

[138] Lee, P. A., & Ramakrishnan, T. V. (1985). Disordered electronic systems. *Rev. Mod. Phys.*, *57*, 287–337.
URL https://link.aps.org/doi/10.1103/RevModPhys.57.287

[139] Liao, Z., & Zhang, J. (2019). Metal-to-insulator transition in ultrathin manganite heterostructures. *Applied Sciences*, *9*(1).
URL https://www.mdpi.com/2076-3417/9/1/144

[140] Lim, W. L., Ebrahim-Zadeh, N., Owens, J. C., Hentschel, H. G. E., & Urazhdin, S. (2013). Temperature-dependent proximity magnetism in Pt. *Applied Physics Letters*, *102*(16), 162404.
URL https://doi.org/10.1063/1.4802954

[141] Liu, J., Cornelissen, L. J., Shan, J., van Wees, B. J., & Kuschel, T. (2018). Nonlocal magnon spin transport in yttrium iron garnet with tantalum and platinum spin injection/detection electrodes. *Journal of Physics D: Applied Physics*, *51*(22), 224005.
URL https://dx.doi.org/10.1088/1361-6463/aabf80

[142] Liu, L., Buhrman, R. A., & Ralph, D. C. (2012). Review and analysis of measurements of the spin hall effect in platinum.

[143] Liu, L., Pai, C.-F., Li, Y., Tseng, H. W., Ralph, D. C., & Buhrman, R. A. (2012). Spin-torque switching with the giant spin hall effect of tantalum. *Science*, *336*(6081), 555–558.
URL https://www.science.org/doi/abs/10.1126/science.1218197

[144] Liu, X., Hong, R., & Tian, C. (2009). Tolerance factor and the stability discussion of abo3-type ilmenite. *Journal of Materials Science: Materials in Electronics*, *20*(4), 323–327.
URL https://doi.org/10.1007/s10854-008-9728-8

[145] Lou, X., Adelmann, C., Crooker, S. A., Garlid, E. S., Zhang, J., Reddy, K. S. M., Flexner, S. D., Palmstrøm, C. J., & Crowell, P. A. (2007). Electrical detection of spin transport in lateral ferromagnet–semiconductor devices. *Nature Physics*, *3*(3), 197–202.
URL https://doi.org/10.1038%2Fnphys543

[146] Lourens, J. A. J., Arajs, S., Helbig, H. F., Cheriet, L., & Mehanna, E. A. (1988). The electrical resistance of Cr films. *Journal of Applied Physics*, *63*(8), 4282–4284.
URL https://doi.org/10.1063/1.340203

[147] Lunney, J. G. (1995). Pulsed laser deposition of metal and metal multilayer films. *Applied Surface Science*, *86*(1), 79–85.
URL https://www.sciencedirect.com/science/article/pii/0169433294003688

[148] Luo, C., Fu, Y., Zhang, D., Yuan, S., Zhai, Y., Dong, S., & Zhai, H. (2015). Temperature dependent coercivity and magnetization of light rare-earth nd doped permalloy thin films. *Journal of Magnetism and Magnetic Materials*, *374*, 711–715.
URL https://www.sciencedirect.com/science/article/pii/S0304885314008336

[149] Lv, Y., Kally, J., Zhang, D., Lee, J. S., Jamali, M., Samarth, N., & Wang, J.-P. (2018). Unidirectional spin-hall and rashba-edelstein magnetoresistance in topological insulator-ferromagnet layer heterostructures. *Nature Communications*, *9*(1), 111.
URL https://doi.org/10.1038/s41467-017-02491-3

[150] Lyo, S. K., & Holstein, T. (1972). Side-jump mechanism for ferromagnetic hall effect. *Phys. Rev. Lett.*, *29*, 423–425.
URL https://link.aps.org/doi/10.1103/PhysRevLett.29.423

[151] Lytvynenko, Y. M., Polek, T. I., Pashchenko, A. V., Prokopenko, V. K., Sycheva, V. Y., & Tovstolytkin, A. I. (2020). Thickness- and substrate-dependent magnetotransport properties of lanthanum–strontium manganite films with overstoichiometric manganese content. *Journal of Materials Science: Materials in Electronics*, *31*(19), 16360–16368.
URL https://doi.org/10.1007/s10854-020-04186-w

[152] Maekawa, S., Kikkawa, T., Chudo, H., Ieda, J., & Saitoh, E. (2023). Spin and spin current—From fundamentals to recent progress. *Journal of Applied Physics*, *133*(2), 020902.
URL https://doi.org/10.1063/5.0133335

[153] Maeno, Y., Hashimoto, H., Yoshida, K., Nishizaki, S., Fujita, T., Bednorz, J. G., & Lichtenberg, F. (1994). Superconductivity in a layered perovskite without copper. *Nature*, *372*(6506), 532–534.
URL https://doi.org/10.1038/372532a0

[154] Majumdar, S., & van Dijken, S. (2013). Pulsed laser deposition of $la_{1-x}sr_xmno_3$: thin-film properties and spintronic applications. *Journal of Physics D: Applied Physics*, *47*(3), 034010.
URL https://dx.doi.org/10.1088/0022-3727/47/3/034010

[155] Manchon, A., Železný, J., Miron, I. M., Jungwirth, T., Sinova, J., Thiaville, A., Garello, K., & Gambardella, P. (2019). Current-induced spin-orbit torques in ferromagnetic and antiferromagnetic systems. *Rev. Mod. Phys.*, *91*, 035004.
URL https://link.aps.org/doi/10.1103/RevModPhys.91.035004

[156] Marmion, S. R., Ali, M., McLaren, M., Williams, D. A., & Hickey, B. J. (2014). Temperature dependence of spin hall magnetoresistance in thin yig/pt films. *Phys. Rev. B*, *89*, 220404.
URL https://link.aps.org/doi/10.1103/PhysRevB.89.220404

[157] McGuire, T., & Potter, R. (1975). Anisotropic magnetoresistance in ferromagnetic 3d alloys. *IEEE Transactions on Magnetics*, *11*(4), 1018–1038.

[158] McLaughlin, R., Sun, D., Zhang, C., Groesbeck, M., & Vardeny, Z. V. (2017). Optical detection of transverse spin-seebeck effect in permalloy film using sagnac interferometer microscopy. *Phys. Rev. B*, *95*, 180401.
URL https://link.aps.org/doi/10.1103/PhysRevB.95.180401

[159] Medvedeva, J. E., Buchholz, D. B., & Chang, R. P. H. (2017). Recent advances in understanding the structure and properties of amorphous oxide semiconductors. *Advanced Electronic Materials*, *3*(9), 1700082.
URL https://onlinelibrary.wiley.com/doi/abs/10.1002/aelm.201700082

[160] Mehanna, A., Arajs, S., Helbig, H. F., Aidun, R., & Kattan, N. A. E. (1987). Electrical conduction in thin chromium films. *Journal of Applied Physics*, *61*(8), 4273–4274.
URL https://doi.org/10.1063/1.338469

[161] Meier, D., Kuschel, T., Meyer, S., Goennenwein, S. T. B., Shen, L., Gupta, A., Schmalhorst, J.-M., & Reiss, G. (2016). Detection of DC currents and resistance measurements in longitudinal spin Seebeck effect experiments on Pt/YIG and

Pt/NFO. *AIP Advances*, *6*(5), 056302.
URL https://doi.org/10.1063/1.4942796

[162] Meier, D., Reinhardt, D., van Straaten, M., Klewe, C., Althammer, M., Schreier, M., Goennenwein, S. T. B., Gupta, A., Schmid, M., Back, C. H., Schmalhorst, J.-M., Kuschel, T., & Reiss, G. (2015). Longitudinal spin seebeck effect contribution in transverse spin seebeck effect experiments in pt/yig and pt/nfo. *Nature Communications*, *6*(1), 8211.
URL https://doi.org/10.1038/ncomms9211

[163] Meyer, S., Althammer, M., Geprägs, S., Opel, M., Gross, R., & Goennenwein, S. T. B. (2014). Temperature dependent spin transport properties of platinum inferred from spin Hall magnetoresistance measurements. *Applied Physics Letters*, *104*(24), 242411.
URL https://doi.org/10.1063/1.4885086

[164] Meyer, S., Chen, Y.-T., Wimmer, S., Althammer, M., Wimmer, T., Schlitz, R., Geprägs, S., Huebl, H., Ködderitzsch, D., Ebert, H., Bauer, G. E. W., Gross, R., & Goennenwein, S. T. B. (2017). Observation of the spin nernst effect. *Nature Materials*, *16*(10), 977–981.
URL https://doi.org/10.1038/nmat4964

[165] Miao, B. F., Huang, S. Y., Qu, D., & Chien, C. L. (2013). Inverse spin hall effect in a ferromagnetic metal. *Phys. Rev. Lett.*, *111*, 066602.
URL https://link.aps.org/doi/10.1103/PhysRevLett.111.066602

[166] Miao, B. F., Huang, S. Y., Qu, D., & Chien, C. L. (2014). Physical origins of the new magnetoresistance in Pt/YIG. *Phys. Rev. Lett.*, *112*, 236601.
URL https://link.aps.org/doi/10.1103/PhysRevLett.112.236601

[167] Miao, B. F., Huang, S. Y., Qu, D., & Chien, C. L. (2016). Absence of anomalous Nernst effect in spin Seebeck effect of Pt/YIG. *AIP Advances*, *6*(1), 015018.
URL https://doi.org/10.1063/1.4941340

[168] Mir, S. A., Seh, A. Q., & Gupta, D. C. (2020). New ferromagnetic half-metallic perovskites for spintronic applications: Bamo3 (m = mg and ca). *RSC Adv.*, *10*, 36241–36252.
URL http://dx.doi.org/10.1039/D0RA06739C

[169] Mott, N. F. (1929). The scattering of fast electrons by atomic nuclei. *Proc. R. Soc. Lond. A*, *124*, 425–442.

[170] Mott, N. F. (2012). In *Electronic Processes in Non-Cystalline Materials*. Oxford University Press.

[171] Nagaosa, N., Sinova, J., Onoda, S., MacDonald, A. H., & Ong, N. P. (2010). Anomalous hall effect. *Rev. Mod. Phys.*, *82*, 1539–1592.
URL https://link.aps.org/doi/10.1103/RevModPhys.82.1539

[172] Nakayama, H., Althammer, M., Chen, Y.-T., Uchida, K., Kajiwara, Y., Kikuchi, D., Ohtani, T., Geprägs, S., Opel, M., Takahashi, S., Gross, R., Bauer, G. E. W., Goennenwein, S. T. B., & Saitoh, E. (2013). Spin hall magnetoresistance induced by a nonequilibrium proximity effect. *Phys. Rev. Lett.*, *110*, 206601.
URL https://link.aps.org/doi/10.1103/PhysRevLett.110.206601

[173] Nakayama, H., Ando, K., Harii, K., Kajiwara, Y., Yoshino, T., Uchida, K.-i., & Saitoh, E. (2010). Inverse spin-hall effect induced by spin pumping in different thickness pt films. *IEEE Transactions on Magnetics*, *46*(6), 2202–2204.

[174] Nakayama, H., Ando, K., Harii, K., Yoshino, T., Takahashi, R., Kajiwara, Y., Uchida, K., Fujikawa, Y., & Saitoh, E. (2012). Geometry dependence on inverse spin hall effect induced by spin pumping in $ni_{81}fe_{19}$/pt films. *Phys. Rev. B*, *85*, 144408.
URL https://link.aps.org/doi/10.1103/PhysRevB.85.144408

[175] Natale, M. R., Wesenberg, D. J., Edwards, E. R. J., Nembach, H. T., Shaw, J. M., & Zink, B. L. (2021). Field-dependent nonelectronic contributions to thermal conductivity in a metallic ferromagnet with low gilbert damping. *Phys. Rev. Mater.*, *5*, L111401.
URL https://link.aps.org/doi/10.1103/PhysRevMaterials.5.L111401

[176] Neil W. Ashcroft, N. D. M. (1976). *Solid State Physics 1st Edition*. 10650 Toebben Dr, KY: Cengage Learning.

[177] Nguyen, M.-H., & Pai, C.-F. (2021). Spin–orbit torque characterization in a nutshell. *APL Materials*, *9*(3).
URL http://dx.doi.org/10.1063/5.0041123

[178] Nguyen, M.-H., Ralph, D. C., & Buhrman, R. A. (2016). Spin torque study of the spin hall conductivity and spin diffusion length in platinum thin films with varying resistivity. *Phys. Rev. Lett.*, *116*, 126601.
URL https://link.aps.org/doi/10.1103/PhysRevLett.116.126601

[179] Ni, L., Chen, Z., Lu, X., Yan, Y., Jin, L., Zhou, J., Yue, W., Zhang, Z., Zhang, L., Wang, W., Wang, Y.-L., Ruan, X., Liu, W., He, L., Zhang, R., Zhang, H., Liu, B., Liu, R., Meng, H., & Xu, Y. (2020). Strong interface-induced spin-charge conversion in YIG/Cr heterostructures. *Applied Physics Letters*, *117*(11), 112402.
URL https://doi.org/10.1063/5.0017745

[180] Nogués, J., & Schuller, I. K. (1999). Exchange bias. *Journal of Magnetism and Magnetic Materials*, *192*(2), 203–232.
URL https://www.sciencedirect.com/science/article/pii/S0304885398002662

[181] O'Brien, L., Erickson, M. J., Spivak, D., Ambaye, H., Goyette, R. J., Lauter, V., Crowell, P. A., & Leighton, C. (2014). Kondo physics in non-local metallic spin transport devices. *Nature Communications*, *5*(1), 3927.
URL https://doi.org/10.1038/ncomms4927

[182] of Edinburgh., R. S. (1853). *Transactions of the Royal Society of Edinburgh*, vol. v.21 (1853-1857). Edinburgh, Royal Society of Edinburgh,. Https://www.biodiversitylibrary.org/bibliography/2290.
URL https://www.biodiversitylibrary.org/item/126375

[183] Olejník, K., Schuler, V., Marti, X., Novák, V., Kašpar, Z., Wadley, P., Campion, R. P., Edmonds, K. W., Gallagher, B. L., Garces, J., Baumgartner, M., Gambardella, P., & Jungwirth, T. (2017). Antiferromagnetic cumnas multilevel memory cell with microelectronic compatibility. *Nature Communications*, *8*(1), 15434.
URL https://doi.org/10.1038/ncomms15434

[184] P. Noziéres, C. L. (1973). A simple theory of the anomalous hall effect in semiconductors. *Journal de Physique*, *34*, 901–915.

[185] Park, S.-i., Quan, Y.-j., Kim, S.-h., Kim, H., Kim, S., Chun, D.-m., Lee, C. S., Taya, M., Chu, W.-s., & Ahn, S.-h. (2016). A review on fabrication processes for electrochromic devices. *International Journal of Precision Engineering and Manufacturing - Green Technology*, *3*(4), 397–421. Copyright - International Journal of Precision Engineering and Manufacturing-Green Technology is a copyright of Springer, 2016; Last updated - 2018-01-10.
URL https://du.idm.oclc.org/login?url=https://www.proquest.com/scholarly-journals/review-on-fabrication-processes-electrochromic/docview/1945160006/se-2

[186] Parker, J. S., Wang, L., Steiner, K. A., Crowell, P. A., & Leighton, C. (2006). Exchange bias as a probe of the incommensurate spin-density wave in epitaxial Fe/Cr(001). *Phys. Rev. Lett.*, *97*, 227206.
URL https://link.aps.org/doi/10.1103/PhysRevLett.97.227206

[187] Peng, S., Zhu, D., Li, W., Wu, H., Grutter, A. J., Gilbert, D. A., Lu, J., Xiong, D., Cai, W., Shafer, P., Wang, K. L., & Zhao, W. (2020). Exchange bias switching in an antiferromagnet/ferromagnet bilayer driven by spin–orbit torque. *Nature Electronics*, *3*(12), 757–764.
URL https://doi.org/10.1038/s41928-020-00504-6

[188] Pongophas, E., Infahsaeng, Y., Maiaugree, W., Phumying, S., Pattanakul, R., Horprathum, M., Chananonnawathorn, C., Piyasin, P., Pinitsoontorn, S., Ramamoorthy, H., Somphonsane, R., Faibut, N., Pijitrojana, W., Khayaiwong, P., & Wongjom, P. (2023). Low-cost instrument for the versatile measurement of spin caloritronic phenomena: Spin seebeck effect, anisotropic magnetoresistance, anomalous hall effect, and anomalous nernst effect. *IEEE Transactions on Instrumentation and Measurement*, *72*, 1–10.

[189] Qu, D., Huang, S. Y., & Chien, C. L. (2015). Inverse spin hall effect in cr: Independence of antiferromagnetic ordering. *Phys. Rev. B*, *92*, 020418.
URL https://link.aps.org/doi/10.1103/PhysRevB.92.020418

[190] Qu, D., Huang, S. Y., Hu, J., Wu, R., & Chien, C. L. (2013). Intrinsic spin seebeck effect in Au/YIG. *Phys. Rev. Lett.*, *110*, 067206.
URL https://link.aps.org/doi/10.1103/PhysRevLett.110.067206

[191] Qu, D., Huang, S. Y., Miao, B. F., Huang, S. X., & Chien, C. L. (2014). Self-consistent determination of spin hall angles in selected $5d$ metals by thermal spin injection. *Phys. Rev. B*, *89*, 140407.
URL https://link.aps.org/doi/10.1103/PhysRevB.89.140407

[192] Ralph, D., & Stiles, M. (2008). Spin transfer torques. *Journal of Magnetism and Magnetic Materials*, *320*(7), 1190–1216.
URL https://www.sciencedirect.com/science/article/pii/S0304885307010116

[193] Ramirez, A. P. (1997). Colossal magnetoresistance. *Journal of Physics: Condensed Matter*, *9*(39), 8171.
URL https://dx.doi.org/10.1088/0953-8984/9/39/005

[194] Ramos, R., Aguirre, M. H., Anadón, A., Blasco, J., Lucas, I., Uchida, K., Algarabel, P. A., Morellón, L., Saitoh, E., & Ibarra, M. R. (2014). Anomalous

nernst effect of fe_3o_4 single crystal. *Phys. Rev. B*, *90*, 054422.
URL https://link.aps.org/doi/10.1103/PhysRevB.90.054422

[195] Randolph, S. J., Fowlkes, J. D., & Rack, P. D. (2006). Focused, nanoscale electron-beam-induced deposition and etching. *Critical Reviews in Solid State and Materials Sciences*, *31*(3), 55–89.
URL https://doi.org/10.1080/10408430600930438

[196] Raveau, B., Martin, C., & Maignan, A. (1998). What about the role of b elements in the cmr properties of abo3 perovskites? *Journal of Alloys and Compounds*, *275-277*, 461–467.
URL https://www.sciencedirect.com/science/article/pii/S0925838898003727

[197] Ravi, S. (2020). High curie temperature and room temperature magnetoresistance in pr2fecro6 material for spintronics applications. *Materials Letters*, *278*, 128448.
URL https://www.sciencedirect.com/science/article/pii/S0167577X20311538

[198] Ren, L., Liu, L., Song, X., Zhao, T., Xing, X., Feng, Y. P., Chen, J., & Teo, K. L. (2023). Manipulation of the topological ferromagnetic state in a weyl semimetal by spin–orbit torque. *Nano Letters*, *23*(8), 3394–3400.
URL https://doi.org/10.1021/acs.nanolett.3c00410

[199] Reverter, F. (2021). A tutorial on thermal sensors in the 200th anniversary of the seebeck effect. *IEEE Sensors Journal*, *21*(20), 22122–22132.

[200] Rezende, S., Rodríguez-Suárez, R., Cunha, R., López Ortiz, J., & Azevedo, A. (2016). Bulk magnon spin current theory for the longitudinal spin seebeck effect. *Journal of Magnetism and Magnetic Materials*, *400*, 171–177.
URL https://www.sciencedirect.com/science/article/pii/S0304885315304108

[201] Rojas-Sánchez, J.-C., Reyren, N., Laczkowski, P., Savero, W., Attané, J.-P., Deranlot, C., Jamet, M., George, J.-M., Vila, L., & Jaffrès, H. (2014). Spin pumping and inverse spin hall effect in platinum: The essential role of spin-memory loss at metallic interfaces. *Phys. Rev. Lett.*, *112*, 106602.
URL https://link.aps.org/doi/10.1103/PhysRevLett.112.106602

[202] Roos, M. J., Bleser, S. M., Hernandez, L., Diederich, G. M., Siemens, M. E., Wu, M., Kirby, B. J., & Zink, B. L. (2023). Electrical, optical, and magnetic properties of amorphous yttrium iron oxide thin films and consequences for non-local resistance measurements. *Journal of Applied Physics*, *133*(22), 223901.
URL https://doi.org/10.1063/5.0144371

[203] Rots, M., Demuynck, S., Cottenier, S., Dekoster, J., & Meersschaut, J. (1999). Longitudinal spin-density-wave ordering in thin epitaxial chromium layers. *Journal of Applied Physics*, *85*(8), 4836–4838.
URL https://doi.org/10.1063/1.370037

[204] Roy, A., & Kumar, P. S. A. (2010). Giant planar hall effect in pulsed laser deposited permalloy films. *Journal of Physics D: Applied Physics*, *43*(36), 365001.
URL https://dx.doi.org/10.1088/0022-3727/43/36/365001

[205] S. O. Valenzuela, M. T. (2006). Direct electronic measurement of the spin hall effect. *Nature Letters*, *442*.

[206] Sagasta, E., Omori, Y., Isasa, M., Gradhand, M., Hueso, L. E., Niimi, Y., Otani, Y., & Casanova, F. (2016). Tuning the spin hall effect of pt from the moderately dirty to the superclean regime. *Phys. Rev. B*, *94*, 060412.
URL https://link.aps.org/doi/10.1103/PhysRevB.94.060412

[207] Saiga, Y., Mizunuma, K., Kono, Y., Ryu, J. C., Ono, H., Kohda, M., & Okuno, E. (2014). Platinum thickness dependence and annealing effect of the spin-seebeck voltage in platinum/yttrium iron garnet structures. *Applied Physics Express*, *7*(9), 093001.
URL https://dx.doi.org/10.7567/APEX.7.093001

[208] Saito, T., Tezuka, N., Matsuura, M., & Sugimoto, S. (2013). Non-local and local spin signals in a lateral spin transport device with $co_2feal_{0.5}si_{0.5}$/n-gaas schottky tunnel junctions. *IEEE Transactions on Magnetics*, *49*(7), 4327–4330.

[209] Saitoh, E., Ueda, M., Miyajima, H., & Tatara, G. (2006). Conversion of spin current into charge current at room temperature: Inverse spin-Hall effect. *Applied Physics Letters*, *88*(18), 182509.
URL https://doi.org/10.1063/1.2199473

[210] Sánchez, J. C. R., Vila, L., Desfonds, G., Gambarelli, S., Attané, J. P., De Teresa, J. M., Magén, C., & Fert, A. (2013). Spin-to-charge conversion using rashba coupling at the interface between non-magnetic materials. *Nature Communications*, *4*(1), 2944.
URL https://doi.org/10.1038/ncomms3944

[211] Schlitz, R., Kosub, T., Thomas, A., Fabretti, S., Nielsch, K., Makarov, D., & Goennenwein, S. T. B. (2018). Evolution of the spin hall magnetoresistance in Cr2O3/Pt bilayers close to the Néel temperature. *Applied Physics Letters*,

112(13), 132401.
URL https://doi.org/10.1063/1.5019934

[212] Schlitz, R., Vélez, S., Kamra, A., Lambert, C.-H., Lammel, M., Goennenwein, S. T. B., & Gambardella, P. (2021). Control of nonlocal magnon spin transport via magnon drift currents. *Phys. Rev. Lett.*, *126*, 257201.
URL https://link.aps.org/doi/10.1103/PhysRevLett.126.257201

[213] Schmid, M., Srichandan, S., Meier, D., Kuschel, T., Schmalhorst, J.-M., Vogel, M., Reiss, G., Strunk, C., & Back, C. H. (2013). Transverse spin seebeck effect versus anomalous and planar nernst effects in permalloy thin films. *Phys. Rev. Lett.*, *111*, 187201.
URL https://link.aps.org/doi/10.1103/PhysRevLett.111.187201

[214] Schreier, M., Roschewsky, N., Dobler, E., Meyer, S., Huebl, H., Gross, R., & Goennenwein, S. T. B. (2013). Current heating induced spin Seebeck effect. *Applied Physics Letters*, *103*(24), 242404.
URL https://doi.org/10.1063/1.4839395

[215] Schumacher, D., Steffen, A., Voigt, J., Schubert, J., Brückel, T., Ambaye, H., & Lauter, V. (2013). Inducing exchange bias in $la_{0.67}sr_{0.33}mno_{3-\delta}/srtio_3$ thin films by strain and oxygen deficiency. *Phys. Rev. B*, *88*, 144427.
URL https://link.aps.org/doi/10.1103/PhysRevB.88.144427

[216] Seebeck, T. J. (1826). Ueber die magnetische polarisation der metalle und erze durch temperaturdiffenez. *Ann. Phys*, *82*, 253–286.

[217] Segal, A., Shaya, O., Karpovski, M., & Gerber, A. (2009). Asymmetric field dependence of magnetoresistance in magnetic films. *Phys. Rev. B*, *79*, 144434.
URL https://link.aps.org/doi/10.1103/PhysRevB.79.144434

[218] Seki, T., Hasegawa, Y., Mitani, S., Takahashi, S., Imamura, H., Maekawa, S., Nitta, J., & Takanashi, K. (2008). Giant spin hall effect in perpendicularly spin-polarized fept/au devices. *Nature Materials*, *7*(2), 125–129.
URL https://doi.org/10.1038/nmat2098

[219] Selvakumar, N., & Barshilia, H. C. (2012). Review of physical vapor deposited (pvd) spectrally selective coatings for mid- and high-temperature solar thermal applications. *Solar Energy Materials and Solar Cells*, *98*, 1–23.
URL https://www.sciencedirect.com/science/article/pii/S0927024811005939

[220] Shan, J., Bougiatioti, P., Liang, L., Reiss, G., Kuschel, T., & van Wees, B. J. (2017). Nonlocal magnon spin transport in NiFe2O4 thin films. *Applied Physics Letters*, *110*(13), 132406.
URL https://doi.org/10.1063/1.4979408

[221] Shen, J., Gai, Z., & Kirschner, J. (2004). Growth and magnetism of metallic thin films and multilayers by pulsed-laser deposition. *Surface Science Reports*, *52*(5), 163–218.
URL https://www.sciencedirect.com/science/article/pii/S0167572903000839

[222] Sheng, P., Sakuraba, Y., Lau, Y.-C., Takahashi, S., Mitani, S., & Hayashi, M. (2017). The spin nernst effect in tungsten. *Science Advances*, *3*(11), e1701503.
URL https://www.science.org/doi/abs/10.1126/sciadv.1701503

[223] Shull, C. G., Chase, C. T., & Myers, F. E. (1943). Electron polarization. *Phys. Rev.*, *63*, 29–37.
URL https://link.aps.org/doi/10.1103/PhysRev.63.29

[224] Sinova, J., Valenzuela, S. O., Wunderlich, J., Back, C. H., & Jungwirth, T. (2015). Spin hall effects. *Rev. Mod. Phys.*, *87*, 1213–1260.
URL https://link.aps.org/doi/10.1103/RevModPhys.87.1213

[225] Slonczewski, J. (1996). Current-driven excitation of magnetic multilayers. *Journal of Magnetism and Magnetic Materials*, *159*(1), L1–L7.
URL https://www.sciencedirect.com/science/article/pii/0304885396000625

[226] Smejkal, L., MacDonald, A. H., Sinova, J., Nakatsuji, S., & Jungwirth, T. (2022). Anomalous hall antiferromagnets. *Nature Reviews.Materials*, *7*(6), 482–496. Copyright - © Springer Nature Limited 2022; Last updated - 2023-11-30.
URL https://du.idm.oclc.org/login?url=https://www.proquest.com/scholarly-journals/anomalous-hall-antiferromagnets/docview/2674582560/se-2

[227] Smit, J. (1955). The spontaneous hall effect in ferromagnetics i. *Physica*, *21*(6), 877–887.
URL https://www.sciencedirect.com/science/article/pii/S0031891455925969

[228] Sola, A., Basso, V., Kuepferling, M., Pasquale, M., Meier, D., Reiss, G., Kuschel, T., Kikkawa, T., Uchida, K.-i., Saitoh, E., Jin, H., Boona, S., Watzman, S., Heremans, J., Hoffmann, A., & Schumacher, H. W. (2018). Spin caloritronic measurements: A round robin comparison of the longitudinal spin

seebeck effect. In *2018 Conference on Precision Electromagnetic Measurements (CPEM 2018)*, (pp. 1–2).

[229] Sola, A., Basso, V., Kuepferling, M., Pasquale, M., né Meier, D. C., Reiss, G., Kuschel, T., Kikkawa, T., Uchida, K.-i., Saitoh, E., Jin, H., Watzman, S. J., Boona, S., Heremans, J., Jungfleisch, M. B., Zhang, W., Pearson, J. E., Hoffmann, A., & Schumacher, H. W. (2019). Spincaloritronic measurements: A round robin comparison of the longitudinal spin seebeck effect. *IEEE Transactions on Instrumentation and Measurement*, *68*(6), 1765–1773.

[230] Sola, A., Bougiatioti, P., Kuepferling, M., Meier, D., Reiss, G., Pasquale, M., Kuschel, T., & Basso, V. (2017). Longitudinal spin seebeck coefficient: heat flux vs. temperature difference method. *Scientific Reports*, *7*(1), 46752.
URL https://doi.org/10.1038/srep46752

[231] Sola, A., Kuepferling, M., Basso, V., Pasquale, M., Kikkawa, T., Uchida, K., & Saitoh, E. (2015). Evaluation of thermal gradients in longitudinal spin Seebeck effect measurements. *Journal of Applied Physics*, *117*(17), 17C510.
URL https://doi.org/10.1063/1.4916762

[232] Solovyev, I. V., Kashin, I. V., & Mazurenko, V. V. (2015). Mechanisms and origins of half-metallic ferromagnetism in cro_2. *Physical Review B*, *92*(14).
URL http://dx.doi.org/10.1103/PhysRevB.92.144407

[233] Sommerfeld, A. (1928). Zur elektronentheorie der metalle auf grund der fermischen statistik. *Z. Physik*, *47*, 1–32.

[234] Song, C., Zhang, R., Liao, L., Zhou, Y., Zhou, X., Chen, R., You, Y., Chen, X., & Pan, F. (2021). Spin-orbit torques: Materials, mechanisms, performances, and potential applications. *Progress in Materials Science*, *118*, 100761.
URL https://www.sciencedirect.com/science/article/pii/S0079642520301250

[235] Song, M., & Furuya, K. (2008). Fabrication and characterization of nanostructures on insulator substrates by electron-beam-induced deposition. *Science and Technology of Advanced Materials*, *9*(2), 023002.
URL https://doi.org/10.1088/1468-6996/9/2/023002

[236] Spiesser, A., Saito, H., Fujita, Y., Yamada, S., Hamaya, K., Yuasa, S., & Jansen, R. (2017). Giant spin accumulation in silicon nonlocal spin-transport devices. *Phys. Rev. Appl.*, *8*, 064023.
URL https://link.aps.org/doi/10.1103/PhysRevApplied.8.064023

[237] Stavroyiannis, S. (2003). Planar hall effect and magnetoresistance in ni81fe19 and co square shaped thin films. *Solid State Communications*, *125*(6), 333–336. URL https://www.sciencedirect.com/science/article/pii/S0038109802008141

[238] Takahashi, S., & Maekawa, S. (2008). Spin current, spin accumulation and spin hall effect. *Science and Technology of Advanced Materials*, *9*(1), 014105. URL https://dx.doi.org/10.1088/1468-6996/9/1/014105

[239] Takamura, Y., Chopdekar, R. V., Arenholz, E., & Suzuki, Y. (2008). Control of the magnetic and magnetotransport properties of La0.67Sr0.33MnO3 thin films through epitaxial strain. *Applied Physics Letters*, *92*(16), 162504. URL https://doi.org/10.1063/1.2908051

[240] Takamura, Y., Chopdekar, R. V., Scholl, A., Doran, A., Liddle, J. A., Harteneck, B., & Suzuki, Y. (2006). Tuning magnetic domain structure in nanoscale la0.7sr0.3mno3 islands. *Nano Letters*, *6*(6), 1287–1291. URL https://doi.org/10.1021/nl060615f

[241] Tang, Z., Kitamura, Y., Shikoh, E., Ando, Y., Shinjo, T., & Shiraishi, M. (2013). Temperature dependence of spin hall angle of palladium. *Applied Physics Express*, *6*(8), 083001. URL https://dx.doi.org/10.7567/APEX.6.083001

[242] Tang, Z., Kitamura, Y., Shikoh, E., Ando, Y., Shinjo, T., & Shiraishi, M. (2013). Temperature dependence of spin hall angle of palladium. *Applied Physics Express*, *6*(8), 083001. URL https://dx.doi.org/10.7567/APEX.6.083001

[243] Thomson, W. (1857). 4. on a mechanical theory of thermo-electric currents. *Proceedings of the Royal Society of Edinburgh*, *3*, 91–98.

[244] Thomson, W. (1857). Xix. on the electro-dynamic qualities of metals:—effects of magnetization on the electric conductivity of nickel and of iron. *Proceedings of the Royal Society of London*, *8*, 546–550. URL https://royalsocietypublishing.org/doi/abs/10.1098/rspl.1856.0144

[245] Thornton, J. A., & Hoffman, D. (1989). Stress-related effects in thin films. *Thin Solid Films*, *171*(1), 5–31. URL https://www.sciencedirect.com/science/article/pii/0040609089900308

[246] Tian, D., Li, Y., Qu, D., Jin, X., & Chien, C. L. (2015). Separation of spin Seebeck effect and anomalous Nernst effect in Co/Cu/YIG. *Applied Physics*

Letters, *106*(21), 212407.
URL https://doi.org/10.1063/1.4921927

[247] Tombros, N., Jozsa, C., Popinciuc, M., Jonkman, H. T., & van Wees, B. J. (2007). Electronic spin transport and spin precession in single graphene layers at room temperature. *Nature*, *448*(7153), 571–574.
URL https://doi.org/10.1038/nature06037

[248] Uchida, K., Ishida, M., Kikkawa, T., Kirihara, A., Murakami, T., & Saitoh, E. (2014). Longitudinal spin seebeck effect: from fundamentals to applications. *Journal of Physics: Condensed Matter*, *26*(34), 343202.
URL https://dx.doi.org/10.1088/0953-8984/26/34/343202

[249] Uchida, K., Ota, T., Adachi, H., Xiao, J., Nonaka, T., Kajiwara, Y., Bauer, G. E. W., Maekawa, S., & Saitoh, E. (2012). Thermal spin pumping and magnon-phonon-mediated spin-Seebeck effect. *Journal of Applied Physics*, *111*(10), 103903.
URL https://doi.org/10.1063/1.4716012

[250] Uchida, K., Ota, T., Harii, K., Takahashi, S., Maekawa, S., Fujikawa, Y., & Saitoh, E. (2010). Spin-seebeck effects in ni81fe19/pt films. *Solid State Communications*, *150*(11), 524–528. Spin Caloritronics.
URL https://www.sciencedirect.com/science/article/pii/S003810980900698X

[251] Uchida, K., Takahashi, S., Harii, K., Ieda, J., Koshibae, W., Ando, K., Maekawa, S., & Saitoh, E. (2008). Observation of the spin seebeck effect. *Nature*, *455*(7214), 778–781.
URL https://doi.org/10.1038/nature07321

[252] Uchida, K.-i., Adachi, H., Kikkawa, T., Kirihara, A., Ishida, M., Yorozu, S., Maekawa, S., & Saitoh, E. (2016). Thermoelectric generation based on spin seebeck effects. *Proceedings of the IEEE*, *104*(10), 1946–1973.

[253] Uchida, K.-i., Adachi, H., Ota, T., Nakayama, H., Maekawa, S., & Saitoh, E. (2010). Observation of longitudinal spin-Seebeck effect in magnetic insulators. *Applied Physics Letters*, *97*(17), 172505.
URL https://doi.org/10.1063/1.3507386

[254] Uchida, K.-i., Qiu, Z., Kikkawa, T., Iguchi, R., & Saitoh, E. (2015). Spin Hall magnetoresistance at high temperatures. *Applied Physics Letters*, *106*(5), 052405.
URL https://doi.org/10.1063/1.4907546

[255] Vignale, G. (2010). Ten years of spin hall effect. *23*, 3–10.

[256] Vlietstra, N., Shan, J., Castel, V., van Wees, B. J., & Ben Youssef, J. (2013). Spin-hall magnetoresistance in platinum on yttrium iron garnet: Dependence on platinum thickness and in-plane/out-of-plane magnetization. *Phys. Rev. B*, *87*, 184421.
URL https://link.aps.org/doi/10.1103/PhysRevB.87.184421

[257] Vlietstra, N., Shan, J., van Wees, B. J., Isasa, M., Casanova, F., & Ben Youssef, J. (2014). Simultaneous detection of the spin-hall magnetoresistance and the spin-seebeck effect in platinum and tantalum on yttrium iron garnet. *Phys. Rev. B*, *90*, 174436.
URL https://link.aps.org/doi/10.1103/PhysRevB.90.174436

[258] Wadley, P., & Edmonds, K. W. (2018). Spin switching in antiferromagnets using néel-order spin-orbit torques*. *Chinese Physics B*, *27*(10), 107201.
URL https://dx.doi.org/10.1088/1674-1056/27/10/107201

[259] Wadley, P., Howells, B., Železný, J., Andrews, C., Hills, V., Campion, R. P., Novák, V., Olejník, K., Maccherozzi, F., Dhesi, S. S., Martin, S. Y., Wagner, T., Wunderlich, J., Freimuth, F., Mokrousov, Y., Kuneš, J., Chauhan, J. S., Grzybowski, M. J., Rushforth, A. W., Edmonds, K. W., Gallagher, B. L., & Jungwirth, T. (2016). Electrical switching of an antiferromagnet. *Science*, *351*(6273), 587–590.
URL https://www.science.org/doi/abs/10.1126/science.aab1031

[260] Wadley, P., Howells, B., Železný, J., Andrews, C., Hills, V., Campion, R. P., Novák, V., Olejník, K., Maccherozzi, F., Dhesi, S. S., Martin, S. Y., Wagner, T., Wunderlich, J., Freimuth, F., Mokrousov, Y., Kuneš, J., Chauhan, J. S., Grzybowski, M. J., Rushforth, A. W., Edmonds, K. W., Gallagher, B. L., & Jungwirth, T. (2016). Electrical switching of an antiferromagnet. *Science*, *351*(6273), 587–590.
URL http://dx.doi.org/10.1126/science.aab1031

[261] Wang, H. L., Du, C. H., Pu, Y., Adur, R., Hammel, P. C., & Yang, F. Y. (2014). Scaling of spin hall angle in 3d, 4d, and 5d metals from $y_3fe_5o_{12}$/metal spin pumping. *Phys. Rev. Lett.*, *112*, 197201.
URL https://link.aps.org/doi/10.1103/PhysRevLett.112.197201

[262] Wang, W. X., Wang, S. H., Zou, L. K., Cai, J. W., Sun, Z. G., & Sun, J. R. (2014). Joule heating-induced coexisted spin Seebeck effect and spin Hall magnetoresistance in the platinum/Y3Fe5O12 structure. *Applied Physics Letters*,

105(18), 182403.
URL https://doi.org/10.1063/1.4901101

[263] Wang, X., Bauer, G. E. W., van Wees, B. J., Brataas, A., & Tserkovnyak, Y. (2006). Voltage generation by ferromagnetic resonance at a nonmagnet to ferromagnet contact. *Phys. Rev. Lett.*, *97*, 216602.
URL https://link.aps.org/doi/10.1103/PhysRevLett.97.216602

[264] Waschk, M., Sarkar, A., Barthel, J., Voigt, J., Schröder, S., Zakalek, P., Schmitz, M., Kirby, B. J., Pütter, S., Schubert, J., & Brückel, T. (2020). Impact of growth kinetics on the interface morphology and magnetization in la1/3sr2/3feo3/la2/3sr1/3mno3 heterostructures. *Journal of Physics: Condensed Matter*, *32*(16), 165801.
URL https://dx.doi.org/10.1088/1361-648X/ab678c

[265] Weiler, M., Althammer, M., Czeschka, F. D., Huebl, H., Wagner, M. S., Opel, M., Imort, I.-M., Reiss, G., Thomas, A., Gross, R., & Goennenwein, S. T. B. (2012). Local charge and spin currents in magnetothermal landscapes. *Phys. Rev. Lett.*, *108*, 106602.
URL https://link.aps.org/doi/10.1103/PhysRevLett.108.106602

[266] Werner, S. A., Arrott, A., & Atoji, M. (2003). Spin Directions in Pure Chromium. *Journal of Applied Physics*, *40*(3), 1447–1449.
URL https://doi.org/10.1063/1.1657712

[267] Wesenberg, D., Hojem, A., Bennet, R. K., & Zink, B. L. (2018). Relation of planar hall and planar nernst effects in thin film permalloy. *Journal of Physics D: Applied Physics*, *51*(24), 244005.
URL https://dx.doi.org/10.1088/1361-6463/aac2b3

[268] Wright, A. J., Erickson, M. J., Bromley, D., Crowell, P. A., Leighton, C., & O'Brien, L. (2021). Origin of the magnetic field enhancement of the spin signal in metallic nonlocal spin transport devices. *Phys. Rev. B*, *104*, 014423.
URL https://link.aps.org/doi/10.1103/PhysRevB.104.014423

[269] Wu, H., Wan, C. H., Yuan, Z. H., Zhang, X., Jiang, J., Zhang, Q. T., Wen, Z. C., & Han, X. F. (2015). Observation of pure inverse spin hall effect in ferromagnetic metals via ferromagnetic/antiferromagnetic exchange-bias structures. *Phys. Rev. B*, *92*, 054404.
URL https://link.aps.org/doi/10.1103/PhysRevB.92.054404

[270] Wu, H., Zhang, H., Wang, B., Groß, F., Yang, C.-Y., Li, G., Guo, C., He, H., Wong, K., Wu, D., Han, X., Lai, C.-H., Gräfe, J., Cheng, R., & Wang, K. L. (2022). Current-induced néel order switching facilitated by magnetic phase transition. *Nature Communications*, *13*(1), 1629.
URL https://doi.org/10.1038/s41467-022-29170-2

[271] Wu, S. M., Fradin, F. Y., Hoffman, J., Hoffmann, A., & Bhattacharya, A. (2015). Spin Seebeck devices using local on-chip heating. *Journal of Applied Physics*, *117*(17), 17C509.
URL https://doi.org/10.1063/1.4916188

[272] Wu, S. M., Hoffman, J., Pearson, J. E., & Bhattacharya, A. (2014). Unambiguous separation of the inverse spin Hall and anomalous Nernst effects within a ferromagnetic metal using the spin Seebeck effect. *Applied Physics Letters*, *105*(9), 092409.
URL https://doi.org/10.1063/1.4895034

[273] Wu, X., Liu, Z., & Luo, T. (2018). Magnon and phonon dispersion, lifetime, and thermal conductivity of iron from spin-lattice dynamics simulations. *Journal of Applied Physics*, *123*(8), 085109.
URL https://doi.org/10.1063/1.5020611

[274] Wunderlich, J., Kaestner, B., Sinova, J., & Jungwirth, T. (2005). Experimental observation of the spin-hall effect in a two-dimensional spin-orbit coupled semiconductor system. *Phys. Rev. Lett.*, *94*, 047204.
URL https://link.aps.org/doi/10.1103/PhysRevLett.94.047204

[275] Xiao, J., Bauer, G. E. W., Uchida, K.-c., Saitoh, E., & Maekawa, S. (2010). Theory of magnon-driven spin seebeck effect. *Phys. Rev. B*, *81*, 214418.
URL https://link.aps.org/doi/10.1103/PhysRevB.81.214418

[276] Xie, Y. J., Scafetta, M. D., Moon, E. J., Krick, A. L., Sichel-Tissot, R. J., & May, S. J. (2014). Electronic phase diagram of epitaxial $La_{1-x}Sr_xFeO_3$ films. *Applied Physics Letters*, *105*(6), 062110.
URL https://doi.org/10.1063/1.4893139

[277] Yang, F. Y., & Chien, C. L. (2003). Exchange coupling between Cr and ferromagnetic thin films. *Journal of Applied Physics*, *93*(10), 6829–6831.
URL https://doi.org/10.1063/1.1544473

[278] Yang, F. Y., & Chien, C. L. (2003). Oscillatory exchange bias due to an antiferromagnet with incommensurate spin-density waves. *Phys. Rev. Lett.*, *90*,

147201.
URL https://link.aps.org/doi/10.1103/PhysRevLett.90.147201

[279] Yang, S., & Zhang, J. (2021). Current progress of magnetoresistance sensors. *Chemosensors*, *9*(8).
URL https://www.mdpi.com/2227-9040/9/8/211

[280] Yang, Y., Wu, B., Yao, K., Shannigrahi, S., Zong, B., & Wu, Y. (2014). Investigation of magnetic proximity effect in Ta/YIG bilayer Hall bar structure. *Journal of Applied Physics*, *115*(17), 17C509.
URL https://doi.org/10.1063/1.4863486

[281] Yin, S. L., Mao, Q., Meng, Q. Y., Li, D., & Zhao, H. W. (2013). Hybrid anomalous and planar nernst effect in permalloy thin films. *Phys. Rev. B*, *88*, 064410.
URL https://link.aps.org/doi/10.1103/PhysRevB.88.064410

[282] Yuan, W., Zhu, Q., Su, T., Yao, Y., Xing, W., Chen, Y., Ma, Y., Lin, X., Shi, J., Shindou, R., Xie, X. C., & Han, W. (2018). Experimental signatures of spin superfluid ground state in canted antiferromagnet cr₂o₃ via nonlocal spin transport. *Science Advances*, *4*(4), eaat1098.
URL https://www.science.org/doi/abs/10.1126/sciadv.aat1098

[283] Zabel, H. (1999). Magnetism of chromium at surfaces, at interfaces and in thin films. *Journal of Physics: Condensed Matter*, *11*(48), 9303.
URL https://dx.doi.org/10.1088/0953-8984/11/48/301

[284] Zakharova, A., Caputo, M., Guedes, E. B., Radovic, M., Nolting, F., & Piamonteze, C. (2021). Interplay between magnetism and interface-induced effects in ultrathin manganites. *Phys. Rev. Mater.*, *5*, 124404.
URL https://link.aps.org/doi/10.1103/PhysRevMaterials.5.124404

[285] Zannoni, A. (1999). On the quantization of the monoatomic ideal gas.

[286] Zhang, R. Q., Liao, L. Y., Chen, X. Z., Xu, T., Cai, L., Guo, M. H., Bai, H., Sun, L., Xue, F. H., Su, J., Wang, X., Wan, C. H., Bai, H., Song, Y. X., Chen, R. Y., Chen, N., Jiang, W. J., Kou, X. F., Cai, J. W., Wu, H. Q., Pan, F., & Song, C. (2020). Current-induced magnetization switching in a cotb amorphous single layer. *Phys. Rev. B*, *101*, 214418.
URL https://link.aps.org/doi/10.1103/PhysRevB.101.214418

[287] Zhang, W., Vlaminck, V., Pearson, J. E., Divan, R., Bader, S. D., & Hoffmann, A. (2013). Determination of the Pt spin diffusion length by spin-pumping and spin Hall effect. *Applied Physics Letters*, *103*(24), 242414.
URL https://doi.org/10.1063/1.4848102

[288] Zhang, Y., & Xu, X. (2020). Curie temperature modeling of magnetocaloric lanthanum manganites using gaussian process regression. *Journal of Magnetism and Magnetic Materials*, *512*, 166998.
URL https://www.sciencedirect.com/science/article/pii/S0304885319339642

[289] Zhou, W., Seki, T., Kubota, T., Bauer, G. E. W., & Takanashi, K. (2018). Spin-hall and anisotropic magnetoresistance in ferrimagnetic co-gd/pt layers. *Phys. Rev. Mater.*, *2*, 094404.
URL https://link.aps.org/doi/10.1103/PhysRevMaterials.2.094404

[290] Zi, Z., Fu, Y., Liu, Q., Dai, J., & Sun, Y. (2012). Enhanced low-field magnetoresistance in lsmo/sfo composite system. *Journal of Magnetism and Magnetic Materials*, *324*(6), 1117–1121.
URL https://www.sciencedirect.com/science/article/pii/S0304885311007566

APPENDIX A

ATOMIC FORCE MICROSCOPE AND SCANNING ELECTRON MICROSCOPE IMAGING

Here, we overview the operations of an atomic force microscope (AFM) for topological imaging of a sample surface. With the analysis of an AFM image, one is able to extract out important quantities such as surface roughness and heights of objects, which are important for material growth and device fabrication.

A.1. Introduction to Atomic Force Microscopes

The atomic force microscopy (AFM) is a very-high-resolution type of scanning probe microscopy with demonstrated resolution on the order of fractions of a nanometer. Figure A.1 depicts a basic schematic of the working principles of the AFM instrument. A laser, technically a superluminous diode, shines on the reflective coating on the backside of the cantilever. The force between the probe tip and the sample surface causes the lever to be deflected when the probe is moved into close proximity with a sample. Optical techniques are used to measure the bending of this flexible cantilever as it responds to mechanical or magnetic interactions with the surface of the sample. Moving the probe across the surface causes the deflection of the probe tip to change as it responds in real-time to the evolution of forces at the surface. As the cantilever taps or is dragged across the surface of the sample, the cantilever is deflected which is recorded as a variation of Z-height coupled to the X and Y lateral positions of the stage. This allows for a 2D image to be transformed into a 3D image.

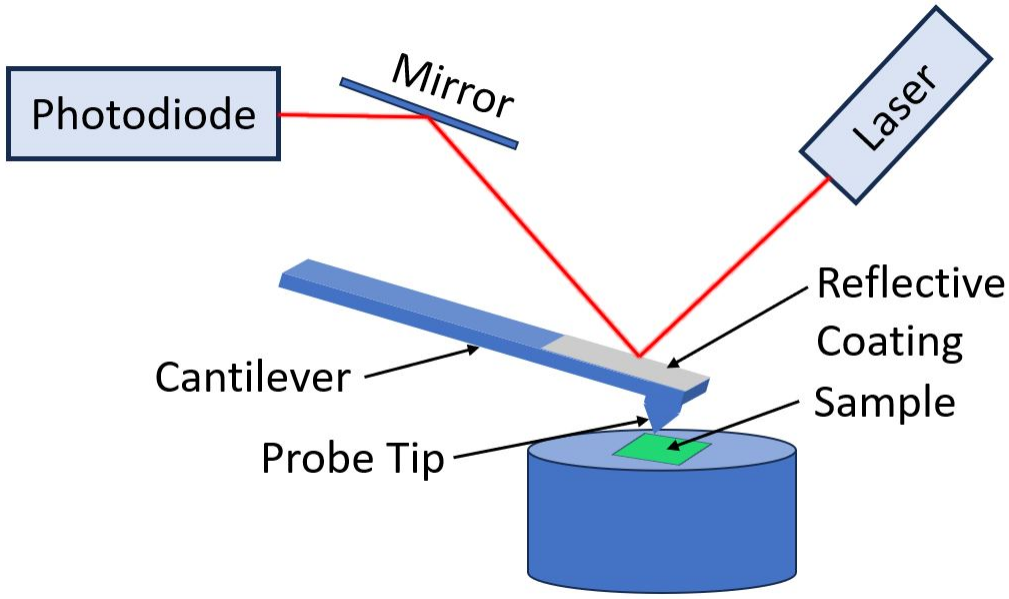

Figure A.1: A schematic of some of the internal components of an atomic force microscope (AFM). Illustration inspired from[10]

Two common scanning modes are depicted in Figure A.2, the left picture is contact mode and the right is tapping mode. In contact mode, the AFM probe tip is dragged across the surface of the sample and the contours of the surface are measured, in the most common way, using the feedback signal required to keep the cantilever at a constant position. In tapping mode, the cantilever is driven to oscillate up and down at or near its resonance frequency by a z-piezoelectric device. The frequency and amplitude of the driving signal are kept constant. The interaction of forces acting on the cantilever when the tip comes into close proximity of the surface, van der Waals forces, dipole-dipole interactions, or electrostatic forces cause the amplitude of the cantilever's oscillation to alter. The height of the cantilever is adjusted in order to maintain the cantilever oscillation amplitude as it is scanned over the surface of the sample. Thus, the tapping AFM image is produced by imaging the force of the intermittent contacts of the tip with the sample surface.

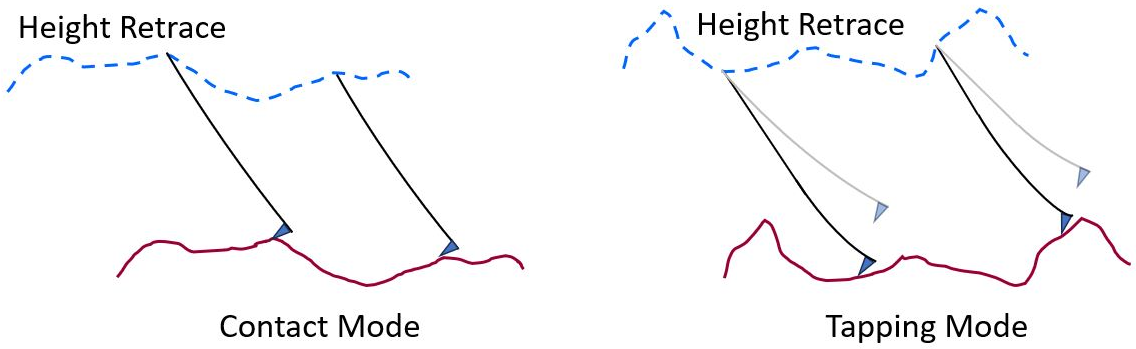

Figure A.2: Cartoon diagrams that represent contact mode (left) and AC tapping mode (right) of an AFM system. Solid lines is a representation of a sample surface and the dashed lines are the height retrace determined by the AFM instrument. Illustrations inspired from[10].

The position of the reflected beam on the photodiode is determined by the angle of the deflected cantilever. That means, as the cantilever drags along the surface of the sample and is bent due to variations in height of the surface, the laser spot on the photodiode will move accordingly to any minute changes in surface. This concept of a laser spot on a photodiode responding to the bending of a cantilever, effectively amplifying the signal, gives the AFM the ability to detect sub-nanometer changes. The photodiode is segmented into four quadrants, as seen in Figure A.3, that record the Z position of the probe tip as it is deflected as vertical displacements on the photodiode and lateral forces as horizontal displacements.

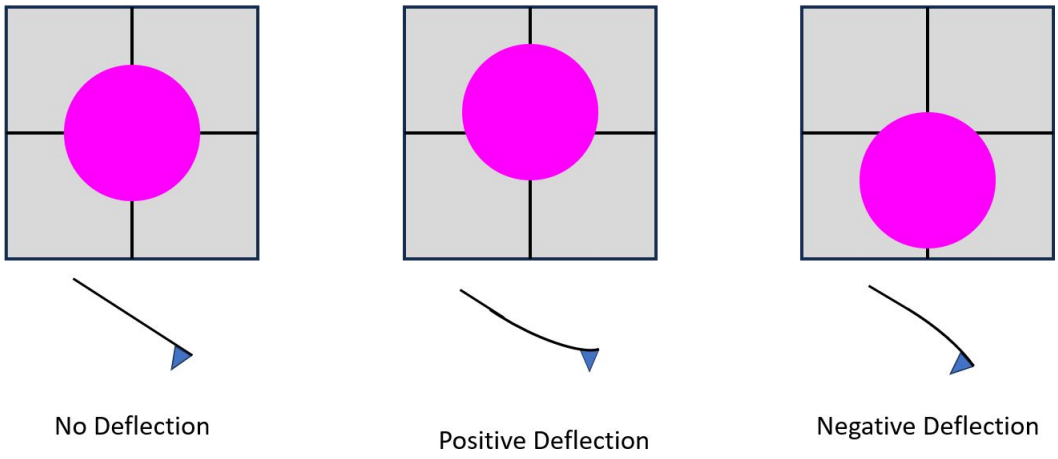

Figure A.3: A cartoon of the deflection of the cantilever being recorded on a segmented photodiode. Illustration taken from [10]

I perform a thickness calibration and measured surface roughness. For all images, I followed the procedure outlined by the Asylum's informative manualette. This manualette is found on their website and describes the procedure for loading a cantilever, aligning the laser to the cantilever, engagement of the probe tip, imaging, image analysis, and how to run a scan.

Once images are obtained, I performed image analysis to remove artifacts from the raw images. Removing artifacts from an image consists of performing a flatten or plane fit functions. Flatten eliminates unwanted features from scan lines such as low frequency noise, bow, or a tilt in an image. It uses all unmasked portions of scan lines to calculate individual least-square fit polynomials for each line. These fits are then subsequently removed from the raw image. This polynomial fit can be of different orders: 0th order fits each line individually to center data, 1st order removes tilt, and 2nd (or 3rd) to remove bow. Likewise, plane fit is another polynomial fit to remove unwanted artifacts from an AFM image. It is a single polynomial of a selectable order for an image and subtracts it from the image. The difference being that the plane fit function can be fitted to either the X scan lines, Y scan lines, or both.

Calibration of the AFM with a standard calibration chip consisting of numerous square features is used to optimize the scanning parameters before imaging a sample.

A.2. Height and Surface Roughness

In Figure A.4 we have the 2D scan, 3D reconstruction, and height vs scan length of a standard AFM calibration chip.

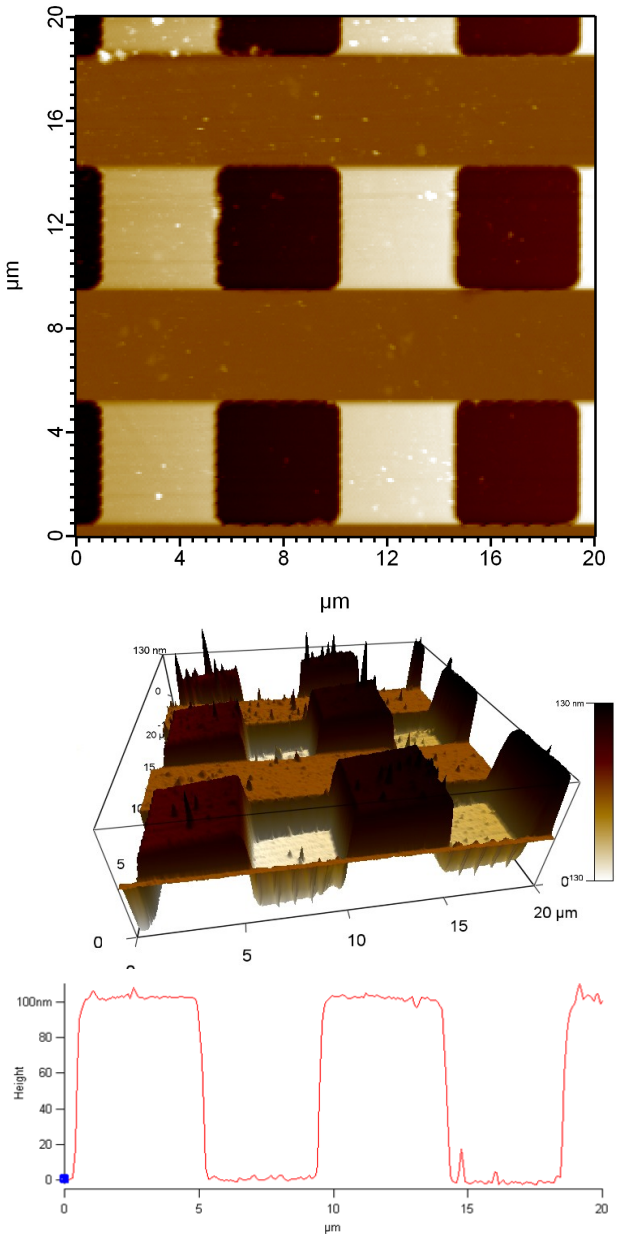

Figure A.4: (Top) A $20 \times 20\,\mu$m 2D image scan of the calibration chip. (Middle) A 3D reconstruction of the 2D scan. (Bottom) A height vs scan length plot.

The image quality of the top figure in Figure A.4 show that the AFM is well optimized. The roughness of the square patterns of the calibration chip is calculated to be 4.503 nm RMS with a 1.459 nm standard deviation. The height of the square

patterns is estimated to be roughly 100 nm, in good agreement with label on the standard chip. In Figure A.5 we present AFM data on the 10 nm thermally evaporated Cr Hall bar structure on a polycrystalline YIG substrate.

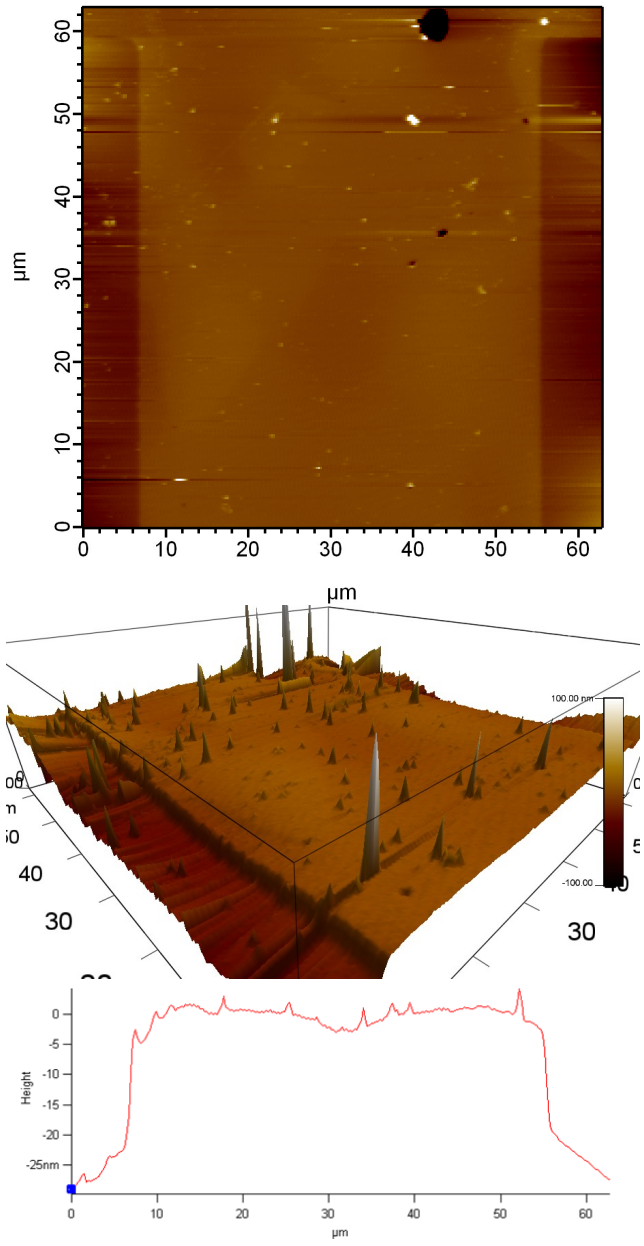

Figure A.5: (Top) A 70×70 μm 2D image scan of the 10 nm thermally evaporated Cr Hall bar on polycrystalline YIG. (Middle) A 3D reconstruction of the 2D scan. (Bottom) A height vs scan length plot.

The Cr had a 1.570 nm RMS roughness with a standard deviation of 1.239 nm. The height retrace graph indicates a roughly 20 nm thickness for the Cr Hall bar structure.

A.3. Imaging With a Scanning Electron Microscope

Images were also taken with a scanning electron microscope (SEM) system. The SEM system acquires these images by rastering an electron beam from top to bottom (left to right) of the scanning area and detecting the scattered electrons from the surface. These SEM images were taken a low beam currents (<50 pA) and used the nanometer pattern generation system (NPGS) software to computer control the acquisition of the SEM image. An SEM image of the 8-terminal circuit used to measure spin orbit torques can be seen in Figure A.6 and an SEM image of the Hall bars used in the longitudinal spin Seebeck experiments can be seen in Figure A.7.

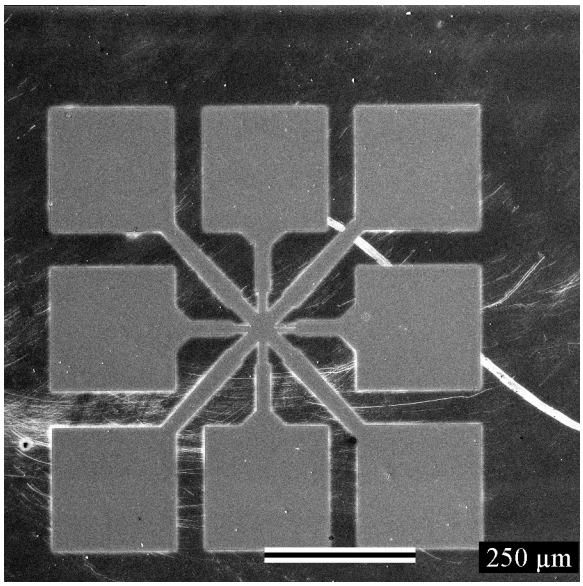

Figure A.6: An SEM image of a 8-terminal circuit used in the spin orbit torque experiments. The device is made of 10 nm Pt on a SiOx/Si substrate.

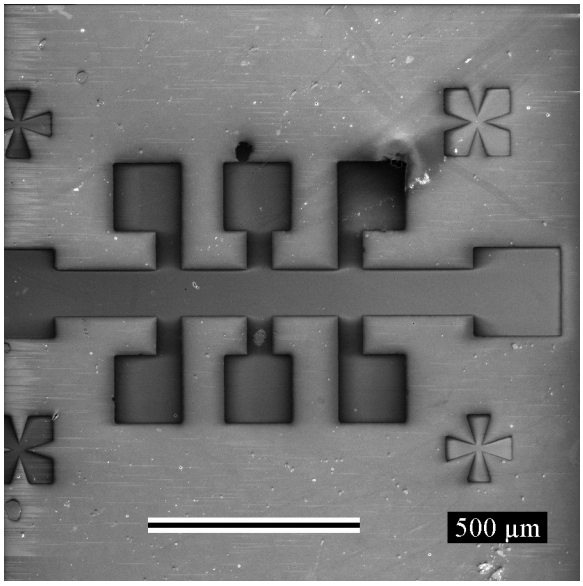

Figure A.7: An SEM image of a 8-terminal Hall bar used in measurements of the longitudinal spin Seebeck effect. This particular image is of a 25 nm Pt Hall bar on top of a ferrimagnetic YIG substrate.

SEM imaging is a useful technique to capture high resolution images of sub-micron structure that are often difficult to see under traditional optical microscopes. The high resolution of these images make it apparent of device structure and any defects that could potentially obscure measurements. Within the NPGS software, distances can be calculated from these images giving accurate device dimension measurements.

APPENDIX B

LABVIEW DESIGN

Here we will overview the essential LabVIEW virtual instrument (VIs) programs that were utilized in the acquisition of data and post analysis.

B.1. Code Used For the Non-local Experiments

Here, we briefly describe the critical LabVIEW programs used to measure the non-local resistances on our samples.

B.1.1. DifferentialConductance_IVCurve.vi

This program uses the differential conductance mode of the paired Keithley 6221/Keithley 2182a. These Keithley instruments are linked together with a RS232 cable and trigger link cable. The differential conductance process uses a stepped sweep of known current values with a specified current delta. This current delta is added to and subtracted from each subsequent step in the sweep.

B.1.2. Film4WDiffCondwithTempReg.vi

This program combines a temperature regulation program that monitors the rate of change of resistance with time with the DifferentialConductance_IVCurve.vi to perform a series of differential conductance measurements across a range of temperatures.

B.1.3. AmplifierFreqSetMagneticFiledsAndMeasurewithTempControlv4.vi

This LabVIEW program controls the AFG function generator output and measures the in-phase voltage, X, and total voltage, R, with a SR 810 lock-in amplifier. The out-of-phase component of the measured voltage, Y, is calculated. These measurements are made at a variety of temperatures and magnetic fields.

B.1.4. DeltaModeVsTwithRegulationAndFieldv2.vi

This program regulates temperatures by measuring change in resistance over time until it meets certain criterion and measures the voltage response from a sweeping magnetic field. The voltage response is measured with the delta mode function of the paired Keithley6221/Keithley 2182a instruments.

B.1.5. SaveOscilloscopeMeasurementsv1.vi

This program interfaces with an oscilloscope and records/saves the data displayed on the front screen of the oscilloscope.

B.2. Code Used For The LSSE Experiments

Here we outline the functionality of the critical LabVIEW programs used in the longitudinal spin Seebeck and spin Hall magnetoresistance measurements. These LabView codes can be found within the LSSEProject.lvproj project folder.

B.2.1. Master_LSSEV1.vi

This program is used to measure the thermal and non-thermal voltage responses from our local devices for spin Seebeck effect measurements. It begins by establishing a VISA connection to required instruments for voltage measurement, current biasing, temperature control, and magnetic field control. Then the parameters are set such as the range of temperatures to be measured, the magnetic field values to sweep to and from with associated field step size, and file name. Once all of that is established the measurements begins. First, the temperature is regulated by measuring the film resistance with either the paired Keithley 2182a nanovoltmeter/Keithley 6221 sourcemeter (TempRegulationForNanoVoltmeterV2.vi) or by measuring the film resistance with the 4-wire ac bridge by Standford Research Systems (Temp_regulation Slope2DUWithRangeScalingv6withNVMforLSSE.vi). The former divides the measured voltage by the supplied current and waits until the slope of the calculated resistance values meets our criterion for stability. The latter performs a 4-wire volt-

age bias resistance measurement and waits for the slope of the resistance to meet our criterion for stability. Once temperature stability is established, the magnetic field is ramped to the positive user defined value. The field is swept towards the negative magnetic field value, then swept from the negative magnetic field value back to the positive magnetic field value, all while voltage values from the Keithley 2182a nanovoltmeter are read (MeasurementLSSEV1.vi). Then the polarity of the supplied dc current from the Keithley 6221 sourcementer is switched and the measurement repeats. This constitutes a single loop of measurements. Each loop is individually saved with SaveEachLoopV1.vi and the thermal and non-thermal components of the signal are calculated with GetSSESMRV1.vi. Once every loop is complete (number of loops is defined by the user), then the averages are calculated (AverageFieldSSESMR-datafromloopsV1.vi) and saved (SaveAVGV1.vi). A new temperature (if applicable) is then set and the whole process repeats until the last user defined temperature point.

B.2.2. LSSECalibrationwithNVMwithSRSOption2.vi

This program is used to calibrate our local geometry devices with either the paired Keithley 2182a nanovoltmeter/6221 current source or, with also, a 4-wire Standford Research System ac bridge. Temperature is regulated by measuring the film resistance of our sample with the Keithley 2182a nanovoltmeter by taking the voltage and dividing it by the supplied current (TempRegulationForNanoVoltmeterV2.vi) or by measuring a voltage biased resistance with the Standford Research System (Temp_regulation Slope2DUWithRangeScalingv6withNVMforLSSE.vi). An output check is taken where a 0 current resistance value is taken when the nanovoltmeter is on/off. Next, the program cycles through a series of user defined currents to supply the Keithley 6221 current source meter, voltage is monitored until it is stable with the 6221VoltageAveWithRealGraphv2.vi, and the voltage is finally measured once it is stable using the same VI. Once all currents from the user generated array are complete, the program goes to the next temperature, and repeats.

B.2.3. CalibrationAnalysisV1.vi

This program takes the data files (written as .txt files) generated from the LSSECalibrationwithNVMwithSRSOption2.vi and processes them to generate R vs T curves, calculate temperature difference, and calculate the sensitivity ($dR/dT * (T/R)$). The data from the files are read and converted to a double precision floating-point numeric (dbl) since the file data is initially stored as string values. The voltage values are then converted into resistances by dividing by their respective current values. The resistance values are recorded for each temperature measured. Temperature (T) vs resistance (R) curves are constructed and fitted to a user defined polynomial (typically a polynomial order of 4 is used). From these fits, temperature difference values can be obtained from subtracting these T vs R curves. A forward derivative calculation is performed:

$$y_i = \frac{1}{dt}\left(x_i - x_{i-1}\right), \tag{B.1}$$

where y_i is the resulting value from the derivative calculation (the sensitivity in this case), x_i is the i-th x-value (resistance), x_{i-1} is the previous i-th x-value (resistance), and dt is sampling interval. The calculated data is then saved.

B.2.4. PostAnalysisSSESMRV1.vi

This program serves to do quick analysis on data files with the appended loop number (that is to say .txt files with loop# appended at the end of the file name). All files with the same base name and indexed only by loop number are found and loaded into the program through the FindAllLoopFilesV1.vi. The imported data, originally as the string data type, is converted into a double precision floating-point numeric type (dbl) with the ConvertStringFilestodblV1.vi. In situations where loop .txt files are not the same size (this can happen when the magnetic field step is not uniform throughout the run), the TruncateTheRawdataV1.vi helps remove zeroes due to un-

even column sizes and truncates the data to even sizes. Spin Seebeck voltages and spin Hall magnetoresistance values are calculate with the CalculateSSEandSMRfromCurrentsV1.vi. If the user wishes to remove averages from the data, they can opt into that option with the RemoveAVGOffsetFromSSEandSMRV1.vi. In scenarios where there is apparent thermal drift, assuming that it is linear, it can be removed with this program. The user enters a known or estimated coercivity and selects the "Remove Linear?" option. The subVIs SubtractLinearComponentFromSaturationV1.vi will remove the thermal drift from the tail ends of the data. Thermal drift that results in individual loops shifted from each other can also be removed if needed. The processed data is then saved.

B.3. Code Used For Spin Orbit Torque Measurements

B.3.1. DCPulse_Main_NoField.vi

This is the main program used to measure spin-orbit torque relation phenomena in the 8-terminal star device. The standford research system 830 lock-in amplifier and Tektronix AFG 3300 function generator are first configured to the desires of the experiment. Temperature regulation is optionally monitored by the TempRegulationForLockInV1.vi where a small, low frequency sine wave current is outputted from the lock-in amplifier and measured with the lock-in amplifier until the slope of the resistance meets the experimentalist's criterion for temperature stability. Afterwards, the SingleDCPulseMeasLockIn.vi is called. This VI send a current pulse from the function generator, waits a sufficient amount of time to avoid thermal artifacts caused by Joule heating, and then measures the voltage from the lock-in amplifier. The process is repeated N number of times. Then, the pulse channel is switched using the standford research system SIM900 and the measurement repeats. The process of pulsing a current in one direction and measuring, pulsing in a different direction and measuring, is looped over k number of times. Data from each pulse direction is displayed on the main VI front panel as graphs. All raw data and

averaged data are saved for each loop.

B.3.2. DCPulse_Main_WithField.vi

This program works similar to DCPulse_Main_NoField.vi except it uses two fields determined by the user. A high field value where a background value is measured and a low field value where another background value is determined. The low field value is also where the pulses occur.

B.3.3. LockINQuickHysteresisV2.vi

This program was used to measure the planar Hall response of the 8-terminal structure using only the lock-in amplifier. The lock-in amplifier is configured to the needed parameters, outputs a small AC current, and measures the first harmonic voltage. An externally applied field is swept downward, starting from the user's high field value, and ending at the user's low field value. Then the applied field is swept in the opposite direction, starting from the user's low field value and ending at the user's high field value. Displayed on the screen are the two individual sweeps and a graph that combines both sweeps into a single curve.

B.3.4. LockINVsFieldQuick_TempDepV3.vi

This program allows for the planar Hall measurement to be conducted over a wide range of input temperatures. Effectively, this creases a planar Hall voltage versus temperature plot. A temperature range is given and controlled through a LakeShore 331 Temperature Controller and regulated by TempRegulationForLock-InV1.vi until conditions are met by the user's inputs fro thermal stability. Then the planar Hall voltage will be measured using LockINQuickHysteresisV2.vi. Finally, a new temperature is determined and the process repeats until the final temperature,

determined by the user, is reached.

B.3.5. FieldNoFieldPulsesAnalysisV1.vi

This program is an analysis program for the DCPulse_Main_NoField.vi or DCPulse_Main_withField.vi, where the raw data is taken, displayed on a graph, and averages and standard deviations are calculated for each part of the measurement.

B.3.6. PulseAnalysisV1.vi

This program takes the pulse data text file and displays each individual pulse from the data set. The user, if some pulse data runs are too noisy, remove them from the calculations by selecting the curves they wish to omit from statistical analysis.

B.3.7. PHEAnalysisV2.vi

This program is for the planar Hall effect measurements. It is a state machine where the user selects a series of buttons from the control panel on the front screen. "Load Data" will open up a file explorer screen where the user can select the planar Hall data they wish to analyze, "Graph Data" will display the planar Hall curve on the graph, "Analyze Data" will do a series of analysis: identify the field location of the peak voltages from the curve, identify the voltage values of the peaks, determine the error in the peak voltages, calculate the average peak voltage, calculate the average peak voltage error, calculate the average field where the peaks occur, and find the difference in field between the peaks.